THESIS FOR THE DEGREE OF DOCTOR OF PHILOSOPHY

Electrolyte evaluation and engineering for the performance enhancement of electrochemical capacitors

Mazharul Haque

Department of Microtechnology and Nanoscience

CHALMERS UNIVERSITY OF TECHNOLOGY

Gothenburg, Sweden 2021

Electrolyte evaluation and engineering for the performance enhancement of electrochemical capacitors

Mazharul Haque

Department of Microtechnology and Nanoscience
Chalmers University of Technology
SE-412 96 Gothenburg
Sweden
Telephone + 46 (0)31-772 1000

To my Abbu and Amma

ABSTRACT

As a consequence of a fast-paced technological evolution along with the acknowledgment of utilizing clean and renewable energy resources over fossil fuels, the importance of energy storage devices is widely recognized. The electrochemical capacitor (EC), commonly known as a supercapacitor or ultracapacitor, is an energy storage device that is already being used in portable consumer electronics, electrification of transportation, and grid-level applications. High power density and long cycle life are the two most prominent properties of ECs, thanks to the electrostatic nature of their charge storage mechanism. These properties are well utilized in a system where ECs are used as a backup power-boosting device to rechargeable batteries. By providing the peak power required, they eventually prolong the battery lifetime. However, the relatively low energy density of ECs compared to rechargeable batteries limits their application as a standalone device. In addition, low operating voltage, adverse self-discharge rate, severe leakage current, elevated temperature incompatibility are some of the crucial issues that are preventing the widespread application of ECs.

Besides a general discussion about ECs, the main objective of this thesis is to identify and address the above-mentioned critical challenges, and to propose and demonstrate corresponding solutions. Firstly, it is revealed that utilizing a redox-active KBr electrolyte can enhance both operating voltage and capacitance, and hence increases energy density without sacrificing power density or cycle life. Secondly, an evaluation of elevated temperature influence on the capacitive performance of ECs containing ionic liquid (IL) electrolyte demonstrates a high working temperature beyond 120 °C. Thirdly, a systematic investigation of ECs containing IL at elevated temperatures shows a significant increase of the self-discharge rate with temperature and pinpoints the underlying mechanisms; at lower initial voltages the self-discharge rate is dominated by diffusion of electrolyte ions rather than charge redistribution. Fourthly, the addition of a small amount of liquid crystals (LC) in neutral electrolyte shows a reduction of self-discharge and leakage current due to slower diffusion of ions in the device, which is proposed to originate from the anisotropic properties of LC. Finally, by utilizing the thermocapacitive effect, a thermal charging of ECs containing IL is demonstrated, where a high voltage of more than 900 mV could be recovered when two devices in series are exposed to a 60 °C temperature environment.

Keywords: Energy storage, supercapacitors, activated carbon, ionic liquid, liquid crystal, redox-electrolyte, self-discharge, leakage current, thermoionic system, thermal charging.

ACKNOWLEDGEMENTS

Mazharul

Göteborg, Sweden

May, 2021

The thesis is based on the following papers:

Paper I

Redox enhanced energy storage in aqueous high-voltage electrochemical capacitor with a potassium bromide electrolyte
Qi Li, Mazharul Haque, V. Kuzmenko, N. Ramani, P. Lundgren, A. D. Smith, P. Enoksson.
Journal of Power Sources, 348 (2017) 219-228.

Paper II
Thermal influence on the electrochemical behavior of a supercapacitor containing an ionic liquid electrolyte
Mazharul Haque, Qi Li, A. D. Smith, V. Kuzmenko, E. Köhler, P. Lundgren, P. Enoksson.
Electrochimica Acta, 263 (2018) 249-260.

Paper III
Identification of self-discharge mechanism of ionic liquid electrolyte based supercapacitor under high temperature operation
Mazharul Haque, Qi Li, C. Rigato, A. Rajaras, A. D. Smith, P. Lundgren, P. Enoksson.
Journal of Power Sources, 485 (2021) 229328.

Paper IV
Self-discharge and leakage current mitigation of neutral aqueous-based supercapacitor by means of liquid crystal additive
Mazharul Haque, Qi Li, A. D. Smith, V. Kuzmenko, P. Rudquist, P. Lundgren, P. Enoksson,
Journal of Power Sources, 453 (2020) 227897.

Paper V
Exploiting low-grade waste heat to produce electricity through supercapacitor containing carbon electrodes and ionic liquid electrolytes
Mazharul Haque, Iqbaal Abdurrokhman, Alexander Idström, Qi Li, A. Rajaras, Anna Martinelli, Lars Evenäs, P. Lundgren, P. Enoksson (Submitted).

Contributions statements (according to CRediT-Contributor Roles Taxonomy)

Paper I: Conceptualization, Investigation, Methodology, Data curation, Writing-review & editing, Resources, Formal analysis.

Paper II: Conceptualization, Methodology, Investigation, Visualization, Data curation, Project administration, Writing-original draft, Writing-review & editing, Formal analysis.

Paper III: Conceptualization, Methodology, Investigation, Visualization, Data curation, Writing-original draft, Writing-review & editing, Formal analysis.

Paper IV: Conceptualization, Methodology, Investigation, Visualization, Data curation, Project administration, Writing-original draft, Writing-review & editing, Formal analysis.

Paper V: Conceptualization, Methodology, Investigation, Visualization, Data curation, Project administration, Writing-original draft, Writing-review & editing, Formal analysis.

Other publications (Not appended due to overlap or out of scope):

- Explanation of anomalous rate capability enhancement by manganese oxide incorporation in carbon nanofiber electrodes for electrochemical capacitors, Electrochimica Acta 340 (11) 135921.
- Comparison of Thermally grown Carbon Nanofiber-Based and Reduced Graphene Oxide-Based CMOS-compatible Microsupercapacitors, physica status solidi (b) 258 (2021) 2000358.
- Finger Number and Device Performance: A Case Study of Reduced Graphene Oxide (rGO) Microsupercapacitors, physica status solidi 258 (2021) 2000354.
- Enhanced Electrode Deposition for On-Chip Integrated Micro-Supercapacitors by Controlled Surface Roughening, ACS omega, 5 (2020) 5219-5228.
- Carbon-Based Electrode Materials for Microsupercapacitors in Self-Powering Sensor Networks: Present and Future Development, Sensors 19 (2019) 4231.
- Surface Roughening with Iron Nanoparticles for Promoted Adhesion of Spin Coated Microsupercapacitor Electrodes, MRS advance 23 (2019) 1335-1340.
- Cellulose-derived carbon nanofibers/graphene composite electrodes for powerful compact supercapacitors, RSC advance 7 (2017) 45968-45977.
- Hierarchical cellulose-derived CNF/CNT composites for electrostatic energy storage, Journal of Micromechanics and Microengineering 26 (2016) 124001.
- Capacitive effects of nitrogen doping on cellulose-derived carbon nanofibers, Materials Chemistry and Physics 160 (2015) 59-65.
- Sustainable carbon nanofibers/nanotubes composites from cellulose as electrodes for supercapacitors, Energy 90 (2015) 1490-1496.
- Investigation of palladium current collectors for vertical graphene-based microsupercapacitors, Journal of Physics: Conference Series 1319 (2018) 012007.
- Giving micro-supercapacitors fingers? 29th Micromechanics and Microsystems Europe (MME) workshop 2018, August 26-29, Bratislava, Slovakia.
- Toward CMOS compatible wafer-scale fabrication of carbon-based microsupercapacitors for IoT, Journal of Physics: Conference Series, 1052 (2018) 012143.
- A carbon based high frequency electrochemical capacitor for miniaturized smart systems, MRS spring meeting 2018, April 2-6, Arizona, United states.
- High voltage aqueous asymmetric supercapacitor with thin film MnO_2 and carbon nanotube electrodes, Advanced energy materials 2017, September 11-13, Surrey, United kingdom.
- Ionic liquid electrolyte for supercapacitor with high temperature compatibility, Journal of Physics: Conference Series, 922 (2017) 012011.

- Redox enhanced supercapacitor with an aqueous potassium bromide electrolyte, smart-Memphis Summer school 2017, June 26-28, Valletta, Malta.
- Nanocomposite materials for miniaturized systems, International conference and exhibition on integration issues of miniaturized systems 2017, March 8-9, Cork, Ireland.
- Graphite paper/carbon nanotube composite: a potential supercapacitor electrode for powering microsystem technology, Journal of Physics: Conference Series, 922 (2017) 012014.

Table of Contents

Introduction

1.1 Electrical Energy Storage devices (EES)

Electrical energy is the primary form of energy in modern civilization, and the demand has been growing enormously. The majority of the industries, such as transportation, agriculture, grid-level application, portable consumer electronics, public services, and residential applications, are heavily dependent on oil, natural gas, and coal [1]. Currently, worldwide acknowledgment of the limited availability of these fossil fuels and their adverse environmental impacts spurred an interest to shift the energy production towards more from sustainable and renewable resources such as wind, solar, and hydropower. This shift opens the possibility to save, simplify distribution, or even convert energy on-site rather than transporting fossil-based fuels [2]. Nevertheless, these renewable resources are dependent on the time and weather of the day, making them highly intermittent. Therefore, electrical energy storage (EES) devices that can store energy and deliver on-demand are the prerequisite for using renewable energy sources [3, 4].

Over the last decades, two main types of devices, namely rechargeable batteries and electrochemical capacitors (ECs), are recognized as essential EES devices. Batteries are the most popular and widely used EES devices throughout the world, dominating the market for all kinds of electronic devices and progressively entering the electrification of transportation and large-scale grid storage system [5]. They offer a stable voltage window with high storage capacity utilizing a redox reaction (either by conversion type or intercalation type). Currently, intercalation type Li-ion batteries can provide specific energy of 20-150 Wh kg^{-1} (based on device mass) with a stable voltage of 3.6 V [5].

With the fast-paced technological evolution, the widely anticipated *Internet of Things* containing an enormous amount of wireless sensors and devices uplifted not only the demand for high storage of energy but also quick delivery of stored energy at a low cost. Generally, rechargeable batteries suffer from long charging times due to their intrinsic low power density (< 1 kW kg^{-1}, based on device mass) and short cycle life. Numerous research activities are ongoing to increase the power density of the battery, but at the current stage, they still do not fulfill the required power demands by many applications, let alone their high cost and limited cycle life [6]. In this regard, ECs are particularly suitable for their high power density (> 10 kW Kg^{-1}, based on device mass), and they can be charged in minutes if not in seconds due to their inherent electrostatic charge storage mechanism [7]. They have attracted immense interest in a wide range of

applications where high power density is of the utmost importance, such as electric and hybrid electric vehicles, uninterruptible power supply, portable electronics, power tools, and seaport cranes [8]. However, the energy density is 1-2 orders of magnitude lower than the rechargeable battery, typically less than 10 Wh Kg^{-1} (based on device mass) [7, 9].

At the current state of the technology, the major improvement of ECs requires increasing energy density without sacrificing the power density and cycle life. The energy density is related to the capacitance and voltage in the following manner: $E = \frac{1}{2} CV^2$, where *C* is the capacitance, and *V* is the operating voltage. Therefore, increasing either capacitance or voltage or both of them will provide improved energy density. As a means to achieve that goal, it is highly required to develop electrode materials with large capacitance or electrolytes with a wide operating voltage range or a smart configuration with an optimized structure. As the energy density is directly proportional to the square of the voltage, it is more efficient to prioritize developing electrolyte materials with an extended operating voltage [10].

Besides the energy density and power density, another critical parameter that needs to be under consideration is the operating temperature range of the device. In applications such as automotive, military, and aerospace ECs are required to operate at elevated temperatures. Even ECs developed for ambient conditions can be exposed to elevated ambient temperature due to weather change or geographical constraints. Moreover, heat is generated during charging-discharging and can lead to a temperature rise in the device. Generally, thermal management or cooling systems are integrated into the power system to address this issue but with a significant compromise on weight and volume of the overall system resulting in reduced efficiency. Often in miniaturized devices, space and volume restrictions are so demanding that adding a thermal management system is not feasible at all [1]. In this regard, as the electrolyte material in the ECs is the most vulnerable constituent at elevated temperature, developing an electrolyte material with a wide range of temperature compatibility can extend the applications of ECs to a large extent.

Although ECs offer several beneficial characteristics such as high power and, compared to rechargeable batteries, unlimited cycle life, they suffer from high self-discharge rates especially in applications where they are standalone devices required to deliver power in a long interval [11]. Self-discharge is a spontaneous voltage decay of charged devices not connected to any power supply. At a charged state, the device is at a higher free energy level compared to the discharged state. Therefore, an internal driving force tries to push the energy level to a lower energy level that initiates self-discharge. In batteries, the electrode potentials are thermodynamically determined at some equilibrium where a single-valued potential is responsible for the charged or discharged state. However, in ECs the potentials are electrostatically determined where a continuous variation of potential is responsible for the

charged or discharged state. Therefore, there is no particular mechanism (thermodynamic or kinetic) that stabilizes the electrode potential resulting in a significantly higher self-discharge in ECs than in batteries [12]. Generally, the high self-discharge in carbon-based ECs originates from uneven electronic charge distribution [13] and an unbalanced ionic distribution in the electric double layer (EDL) [14]. Several factors such as initial voltage, charging current, charging duration, operational history, and temperature influences the self-discharge behavior. Different strategies to suppress the self-discharge rate involve the modification of all the constituents of ECs: electrodes, electrolytes, separators, current collectors, or smart device design such as bipolar configuration.

1.2 Scope of the thesis

In order to achieve the optimum performance of ECs each of the constituents should have good compatibility with each other. A particular focus in this thesis work has been to develop well-performing electrolytes to maximize the ECs performance in terms of increased energy density, improved high-temperature performance, and suppressed self-discharge. Chapter 2 describes the fundamentals of EC technology. Chapter 3 presents the experimental evaluation of ECs. Chapter 4 covers a brief overview and discussion regarding the undertaken strategies to enhance the capacitive performance of ECs. Chapter 5 contains the conclusion and future work. In the end, Chapter 6 presents a summary of the appended papers. **Paper I** describes a way to increase energy density by taking advantage of the redox activity of KBr electrolyte. **Paper II** presents an EC with an ionic liquid electrolyte operating in a wide elevated temperature range. **Paper III** investigates temperature influence on self-discharge characteristics of an ionic liquid electrolyte containing EC and identifies the underlying self-discharge mechanisms. **Paper IV** demonstrates a simple way to reduce the self-discharge of an EC containing Li_2SO_4 electrolyte with a nematic liquid crystal additive by taking advantage of the anisotropic property of the liquid crystal. **Paper V** demonstrates the potential to use low-grade waste heat to recover charge in an ionic liquid containing ECs.

Development of EC technology

2.1 Constructions and working mechanism of EES

The construction of EES devices is similar, comprising of two electrode materials, an electrolyte, an ion-impermeable separator, current collectors, and encapsulating casing, as shown in Fig.1. However, the electrochemical signature and fundamental charge storage mechanisms are very different.
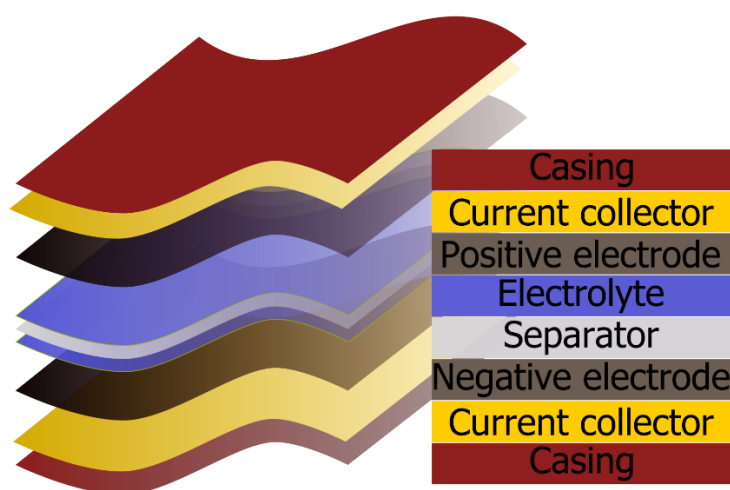

Figure 1: Schematic of EES device construction.

In rechargeable batteries, the charge storage takes place in the bulk of the electrode material in combination with electrolytes through a reversible faradaic reaction. Therefore, the designed materials are susceptible to the insertion/de-insertion of the reacting species throughout the material. Upon applying a specific potential, the reaction at negative electrodes gives rise to electrons that are accepted by the reaction that happens in the positive electrode. During the process, 1-3 electrons per atom or molecule participate in the reaction [15]. Due to this high electron density, batteries can store vast amounts of charge. At the same time, as these reactions are diffusion-controlled, the kinetics are slow, resulting in low power density.

In ECs, charges are stored only on the surface or close to the surface of the electrodes. Therefore, the electrode materials are designed to have a high surface area. Upon applying a potential, the charge is stored in the interface between the electrode and electrolyte by forming an electrical double layer (EDL). As there is no Faradaic reaction involved in the process, kinetics is very fast

compared to batteries, which give rise to a high power density. As only 0.18 electrons per carbon atom participate in the charge storage process at a relatively low voltage, the energy density of an electrical double-layer capacitor (EDLC) is low compared to a battery [15]. Another class of ECs involves fast and reversible surface redox reactions without any ion diffusion in the bulk of the material. This kind of ECs is known as pseudocapacitor, and it mimics the capacitive behavior like the EDLC. Due to the involvement of multielectron in the redox reactions, the energy density of pseudocapacitors is higher than EDLC [9]. As phase changes do not occur within the materials of ECs during their operation; theoretically, they hold a limitless cycle life, whereas rechargeable batteries can survive only for a few thousands of cycles due to volume changes in the material upon cycling [16]. Table 1 summarizes the fundamental operational parameter differences between ECs and rechargeable batteries [3].

Table 1. Features of typical ECs and rechargeable batteries

Characteristics	ECs	Rechargeable batteries
Charge time	1 - 10 s	10 - 60 min
Specific power (W kg^{-1})	10000	1000 - 3000
Specific energy (Wh Kg^{-1})	< 10	120 - 240
Charge temperature	-40 to 65 °C	0 to 45 °C
Discharge temperature	-40 to 65 °C	-20 to 60 °C
Discharge efficiency	Fast and efficient for discharge from V_{max} to ½ V_{max}	Slow and efficiency depends on the internal resistance
Storage mechanism	Physical	Chemical
Energy limitation	Limited to electrode surface area	High (bulk)
Power limitation	Electrolyte conductivity, separator	Reaction kinetics and mass transport
Charge rate	High, same as discharge rate	Kinetically limited with mass transport
Cycle life limitations	Side reactions	Mechanical stability, chemical reversibility

Recently, a significant effort has been carried out to explore the hybrid devices by combining a high power characteristic of supercapacitor and high energy characteristic of rechargeable batteries both on the material level and the device level [6, 17]. All these devices have their respective applications, and they are not competitive rather complementary to each other.

2.2 Parallel plate capacitor

From an electronic point of view, there is a substantial similarity between conventional capacitors and ECs; however, there lies a significant difference from a technological point of view. Therefore, it is useful to have a brief overview of the basic principles of the capacitor to understand the capacitive mechanism that occurs in ECs entirely.

The simplest example of a capacitor is a parallel plate capacitor consisting of two conducting metal plates (electrodes) separated by a vacuum or a dielectric material (Fig. 2). The capacitor is charged upon applying a voltage difference across the electrodes from an external power supply (battery). Upon connecting to the battery, the electrons from one electrode of the capacitor start flowing towards the positive terminal of the battery, leaving an electron deficiency on the electrode and hence becomes positively charged. Simultaneously, an equal magnitude of electron surplus develops on the other electrode and becomes negatively charged. The flow of electrons continues until the voltage difference between the electrodes matches the externally supplied voltage and considered as a fully charged capacitor. If we connect this charged capacitor in a circuit with a load, it will work as a voltage source, and the current will flow until a complete charge balance is reached.
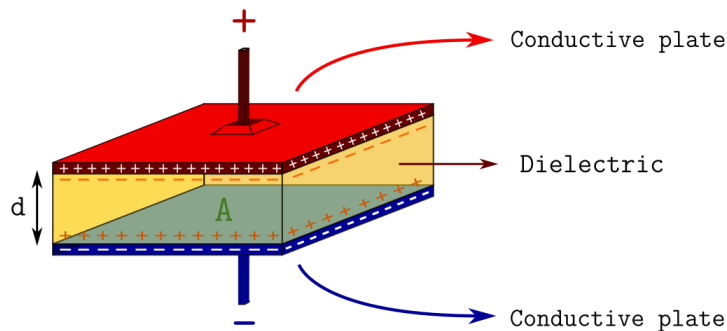
Figure 2: Schematic of a parallel plate capacitor.

For a given capacitor the quantity of stored electric charge on the electrodes is directly proportional to the voltage between them and expressed as $Q = C \cdot V$, where Q is the charge in each electrode, V is the voltage difference between the plates, and C is a positive proportionality constant called capacitance. The SI unit of capacitance is the *farad* (F). Upon rearranging the equation in the following manner $V = Q/C$, if the C is very high, it will require a low voltage (V) to store a given amount of charge (Q). If the C is very low, then it needs a high voltage (V) to store the same amount of charge (Q). Therefore, capacitance is just a measure of the efficiency of storing electric charges for a given voltage.

Opposite charges on the electrodes in a charged state create an electric field from the positive to negative electrodes. This electric field is uniform between the electrodes, and according to Gauss's law, it can be expressed as:

$$E = \frac{\sigma}{\varepsilon_0}$$
Equation 1

where E is the electric field, σ is the charge density of the electrode $\left(\sigma = \frac{Q}{A}\right)$, ε_0 is the permittivity of free space or vacuum permittivity. Therefore, the electric field inside the capacitor is expressed as:

$$E = \frac{Q}{\varepsilon_0 \cdot A}$$
Equation 2

where Q is the charge, A is the area of the electrodes. If the electric field is uniform, then the potential difference between the plates is

$$V = E \cdot d$$
Equation 3

where d is the distance between the electrodes. A further extrapolation of this equation leads to

$$V = \frac{Q}{\varepsilon_o \cdot A} \cdot d$$
Equation 4

Therefore, the capacitance can be expressed as:

$$C = \frac{Q}{V} = \frac{\varepsilon_o \cdot A}{d}$$
Equation 5

Hence, the capacitance solely depends on the area of the electrode, the distance between the two electrodes, and the permittivity/relative permittivity of the dielectric material.

The dielectric material present between the plates orients itself according to the electric field lines inside the capacitor. The orientation creates a net negative charge on the dielectric next to the positive electrode and a net positive charge on the dielectric next to the negative electrode and consequently creates an internal electric field within the dielectric material. This internal electric field partially counteracts the electric field between the electrodes resulting in a decreased electric field that leads to a fall in voltage (Equation 3). As the voltage decreases without any change in the stored charge, the insertion of the dielectric material increases the capacitance.

The measure of the ability of a dielectric material to be polarized under an applied electric field is known as permittivity. The higher the permittivity, the greater the material is prone to reduce the electric field set up in it. Relative permittivity or dielectric constant is a ratio of the permittivity of a dielectric material relative to the permittivity of free space and can be expressed as $\kappa = \varepsilon / \varepsilon_o$. Consequently, the expression of the capacitance is $C' = \kappa\, C$, where C' is the

capacitance of a capacitor with a dielectric material, and C is the capacitance of a capacitor with a vacuum. Therefore considering a fixed configuration (area and the distance between the plates) of the capacitor, the higher the dielectric constant, the greater the capacitance. The operating voltage of a capacitor is defined by the dielectric strength (V m^{-1}) of the material, which is the maximum electric field that can exist in a dielectric material without an electrical breakdown. Several factors affect the dielectric strength, such as the thickness of the material, temperature, and frequency [18]. Due to the small surface area of the electrodes, the conventional capacitors can yield a capacitance in the range of pF to µF with a broad voltage range of 50 to 400 V [19].

2.3 Electrolytic capacitor

The second generation of capacitive devices is known as electrolytic capacitors. These provide a higher capacitance compared to conventional capacitors. Even though the basic working principle is the same as the parallel plate capacitor, the configuration of the device is quite different. A schematic of an aluminum electrolytic capacitor is given in Fig. 3.

As the name suggests, the electrolytic capacitor contains an electrolyte, which is an ionic conductor, but an electronic insulator and, in practice, functions as the negative terminal (real cathode) of the device. In principle, a metal foil, using e.g. aluminum, tantalum, niobium, titanium, or silicon, is used as a positive terminal (anode) and as a negative terminal (apparent cathode) of the device. A polymeric paper functions as a separator in order to avoid short-circuiting the plates. For the anode material, the metal foil is electrochemically etched or sintered to increase the surface area (almost 100 times compared to the plane metal) onto which an oxide layer is grown by a process called anodization [20].
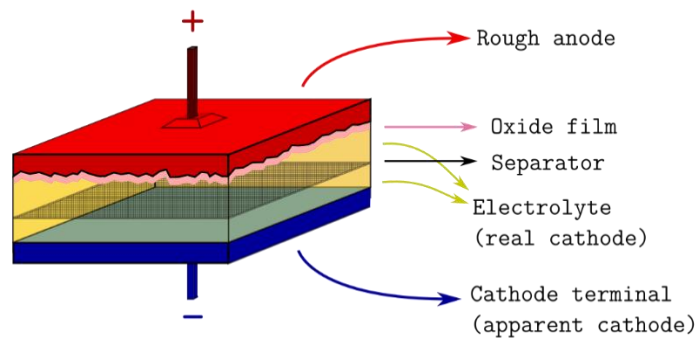
Figure 3: Schematic of an electrolytic capacitor.

Unlike a conventional capacitor that contains a separate dielectric material, an electrolytic capacitor uses its built-in oxide layer as a dielectric. The thickness of the oxide layer is nearly proportional to the applied dc voltage (also called formation voltage) during the anodization process. Generally, the ratio of the oxide thickness to the formation voltage is about 1 nm/V [20].

The dielectric strength is determined by the thickness, structure, and composition of the oxide layer. Inherently this oxide layer possesses a forward direction insulation property when in contact with an electrolyte (cathode), giving rise to the different polarity of the device [20].

The dielectric coating or the thickness of the oxide layer on the cathode side is significantly thinner than the anode side. Therefore, the capacitance in the negative terminal is also considerably higher than the capacitance in the positive terminal. Considering the total capacitance of a practical electrolytic capacitor is a combination of two capacitors in series [21],

$$\frac{1}{C_t} = \frac{1}{C_p} + \frac{1}{C_n}$$
Equation (6)

where C_t is the total capacitance, C_p is capacitance in the positive terminal, and C_n is the capacitance in the negative terminal. By making the capacitance in the negative terminal large, the total capacitance is realized only from the capacitance from the positive terminal, $C_t \sim C_P$. Due to the high surface area of the electrodes and the high dielectric constant of the oxide layer, the capacitance of an aluminum electrolytic capacitor is in the mF range with a rated voltage of 300 V [21].

2.4 Electrochemical capacitor

ECs are the latest addition to capacitor technology. They offer a significantly higher capacitance than the other counterparts do. The construction of ECs is somewhat different from the electrolytic or conventional plate capacitor; instead, it is more similar to the rechargeable battery concerning design and manufacturing. However, in principle, the underlying working mechanism still follows the capacitive principle of charge storage. The EC also contains an electrolyte but it does not participate in any chemical reaction to produce the dielectric oxide layer as in an electrolytic capacitor. In fact, there is no apparent dielectric in the EC; instead, there is a formation of an EDL at the electrode and electrolyte interface, and the electrolyte ions contribute to the charge storage by getting adsorbed on the electrode surface. Depending on the implemented materials, configurations, and working mechanisms, ECs are generally classified into three main categories:

   1) Electrical double-layer capacitor (EDLC)

   2) Pseudocapacitor

   3) Hybrid supercapacitor

2.4.1 EDLC

In an EDLC, the capacitance arises from the charge stored in the electric double layer (EDL) residing at the interface between the electrodes and electrolytes. What corresponds to dielectric

thickness or distance between plates in a conventional capacitor forms naturally in an EC at the interface with an atomic distance of separation. This minimal distance at the interface and the high surface area of the electrodes are the roots of the improved capacitance.

1) The progressive development of the EDL model

The models of EDL formation at the electrode/electrolyte interface developed gradually as shown in Fig. 4. The foremost model was developed by von Helmholtz (Fig. 4a), where he observed a separation of cationic and anionic charge across the interface of colloidal particles in an electrolyte. Eventually, the theory was extended to metal surfaces.
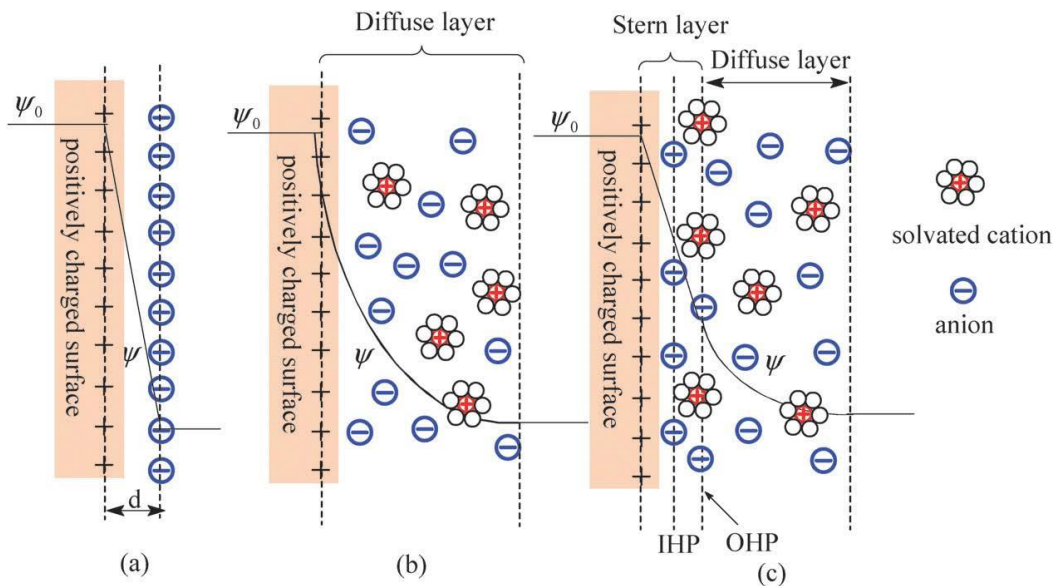

Figure 4: Progressive development of EDL theory (a) Helmholtz model (b) Gouy-Chapman model (c) Stern/Grahame model [22]. (Reprinted with permission from RSC)

When a voltage is applied to a metal electrode immersed in an electrolyte solution, an excess or deficit of electronic charges on the metal surfaces develops relative to the counter-ions in the electrolyte solution. Therefore, two parallel layers of charge are formed: one charged layer from the metal surface and one oppositely charged layer of ions from the electrolyte side with a separation on the order of an atomic distance, forming a structure termed "EDL" [23]. The model assumes that the metal surface charge is neutralized by the static counter ions from the electrolyte through Coulomb's force. The potential across the double layer falls to zero in a similar fashion (linearly) of a conventional parallel plate capacitor, and the capacitance is expressed as:

$$C_H = \frac{\varepsilon_r \varepsilon_o A}{d}$$
Equation (7)

where ε_r is the dielectric constant of electrolyte, ε_o is the vacuum permittivity, A is the surface area, and d is the effective thickness of the EDL, also known as the Debye length which is generally in the range of < 1 nm [24].

The Helmholtz model was modified by Gouy and Chapman (Fig. 4b), considering that charged ions in the electrolyte solution are not static but subjected to a random and continuous thermal motion under the combined influence of ion diffusion driven by the concentration gradients and electromigration driven by the electric field. Therefore, the surface charge is balanced by a distribution of ions named a "diffuse layer", unlike the rigid counter layer proposed by Helmholtz. In this model, ions are treated as point charges, and the ion concentration follows a Boltzmann distribution near the surface, and the charge density with the potential follows the Poisson equation, and accordingly, the potential falls exponentially to the bulk solution [25, 26].

However, the Gouy-Chapman model overestimates the capacitance from a highly charged double layer due to treating the ions as point charges and not considering the finite size of the ions. Afterward, Stern modified the EDL model by combining the Gouy-Chapman model and the Helmholtz model, which distinguishes two different regions of ion distribution, namely the compact region (Stern layer or Helmholtz layer - ions with finite-size get adsorbed very close to the electrode surface) and the diffuse layer (ions are mobile) [27].

Afterward, the compact layer was further divided by Grahame (Fig. 4c) into two regions: the inner Helmholtz plane (IHP), where the ions are specifically (covalently bonded) adsorbed, and the outer Helmholtz plane (OHP) where ions are non-specifically (electrostatically) adsorbed or solvated [28]. Continuum models of EDLCs only consider electrostatic adsorption concerning the Stern model [29]. Generally, the most common cations are smaller than the anions and prone to have larger solvation shells. Therefore, they will have a larger distance of closest approach to the electrodes and reside in the OHP whereas, the anions reside in the IHP (in most of the cases irrespective of the charged nature of the electrode) [15, 22]. As the distance of the closest approach for anions is smaller than the distance of the closest approach for solvated cations, the intrinsic capacitance of the positively charged electrode is roughly twice the negatively charged electrode; of course, this can differ based on the electrodes, electrolyte ions and solvents [15].

Concerning the distinct regions in the EDL, the total double-layer capacitance (C_{DL}) can be expressed as equivalent to two capacitors in series,

$$\frac{1}{C_{DL}} = \frac{1}{C_H} + \frac{1}{C_D} \qquad\qquad \text{Equation 8}$$

where C_H originating from the Helmholtz layer or Stern layer and C_D originating from the Diffuse layer.

It is worth mentioning that the EDL models mentioned above are developed in terms of an infinite planar metal surface with an electrolyte. In a typical EDLC, the electrodes are made from highly porous carbon materials with a large surface area and with a diverse geometry of pores. According to the International Union of Pure and Applied Chemistry (IUPAC), pores can be classified based on their diameter or inter-layer distance in the case of slit-shaped pores. Initially, pores were categorized into three main sections: macropores (> 50 nm), mesopore (2-50 nm), and micropore (< 2 nm) [30]. In 2015 as a consequence of the vast technological development of nanomaterials, IUPAC modified the category [31]; supermicropores (smaller than 2 nm but larger than 0.7 nm), and ultramicropores (< 0.7 nm), (Fig. 5).
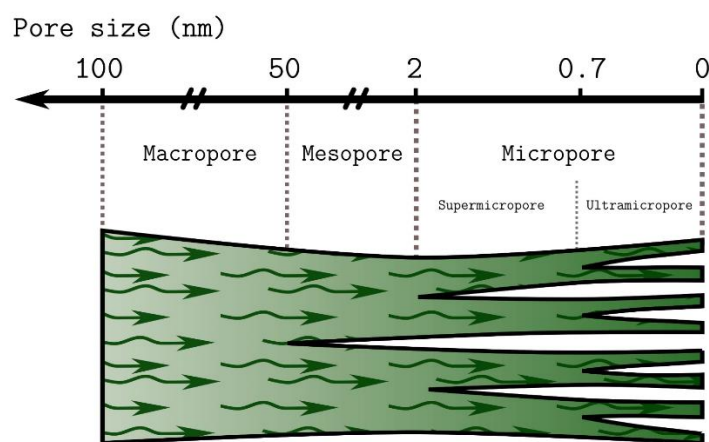

Figure 5: Classification of pores according to IUPAC and ion diffusion pattern in a typical hierarchical porous structure.

A material that contains pores with different sizes and shapes without any interconnection is not considered a porous material. For ECs, where fast diffusion of electrolyte ions is of the utmost importance, carbon materials with a good interplay among different pores are highly suitable. Typically, in a hierarchical porous material, electrolyte ions initially enter the largest pores and then proceed to the smaller ones (Fig. 5).

Consequently, the EDL properties in the porous carbon-based system are more complex than in the infinite planar electrodes. It is influenced by the wetting properties (hydrophobic or hydrophilic) of the electrode surface by the electrolyte, the ohmic resistance related to the electrolytes, the limited space constraints inside the pores, and the tortuous mass transfer path [22]. Most importantly, the capacitive behavior will largely depend on the geometric features of the different pores. The classical EDL model excludes the contribution of supermicropores to the charge storage mechanisms due to their small size compared to the size of the solvated ions. However, recent studies show that partial desolvation of solvated ions occurs, and even a pore size less than 1 nm contributes to the charge storage, leading to an enhanced capacitance [32,

33]. This phenomenon cannot be modeled solely by Equation (7), and the capacitance calculation will not be valid for a system containing porous material. The explanation of the anomalous enhancement of capacitance has recently been modeled [34, 35] by taking into account the pore curvature. Considering that mesoporous carbon materials are cylindrical, the solvated counterions enter the pores and proceed to the pore walls forming an electric double-cylinder capacitor (EDCCs) (Fig. 6b), and in the micropores, solvated, partially solvated, or desolvated counterions line up along the pore axis forming an electric wire-in-cylinder capacitor (EWCC) (Fig. 6c).

Macropore
(Ø ≥ 50 nm)

Mesopore
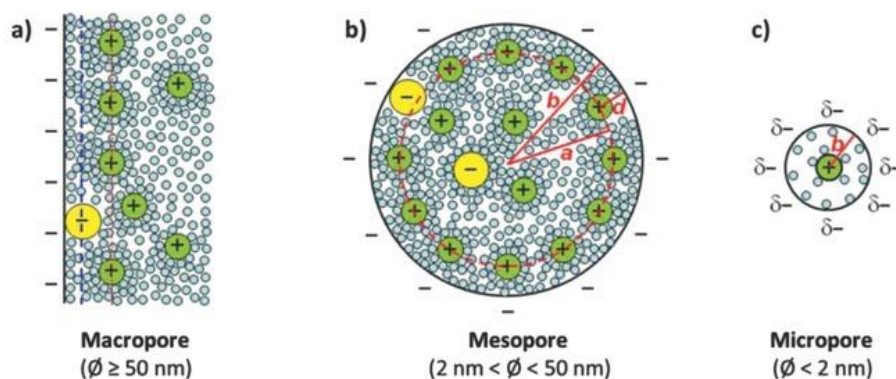**(2 nm < Ø < 50 nm)**

Micropore
(Ø < 2 nm)

Figure 6: Double layer formation in (a) macropore (b) mesopore and (c) micropore [24, 34]. (Reprinted with permission from John Wiley and Sons)

The assessment of the capacitance from these proposed models can be expressed as:

$$C_{EDCC} = \frac{2\pi\varepsilon_r\varepsilon_o L}{ln(b/a)} \ or, \frac{\varepsilon_r\varepsilon_o}{bln\ [b/(b-d)]} A \qquad \text{Equation 9}$$

$$C_{EWCC} = \frac{\varepsilon_r\varepsilon_o}{bln(b/a_0)} A \qquad \text{Equation 10}$$

where L is the pore length, b and a are the radii of the outer and inner cylinders, d is the distance of approaching ions to the electrode surface, a_0 is the effective size of the counterions.

The EDCC model could be naturally reduced to the classical EDL model (Fig. 6a) for macropores considering insignificance of the pore curvature, where Equation (7) is applicable. The proposed models were validated by fitting experimental data with carbon materials with diverse pore sizes and with different electrolytes and provides a fundamental insight regarding the modern EDL model regarding ECs and related electrolytes [34, 35].

2) EDLC construction and working mechanism:

For an EDLC construction, two high surface area carbon electrodes (1000-3000 $m^2\ g^{-1}$) are ionically connected through an electrolyte and separated by an ion-permeable but electron non-

permeable separator that makes sure that there is no short circuit between the electrodes. Fig. 7 demonstrates a schematic of an EDLC with its equivalent circuit.
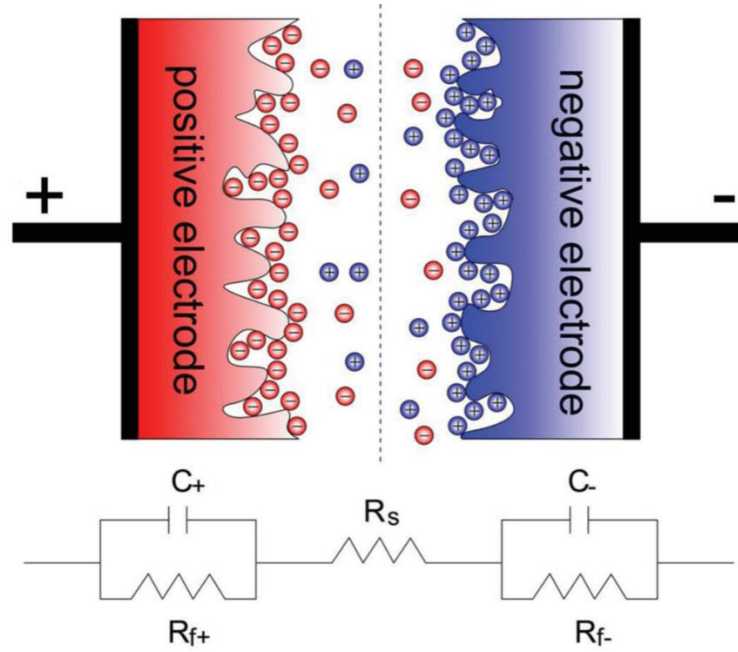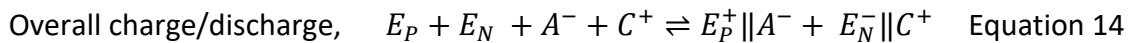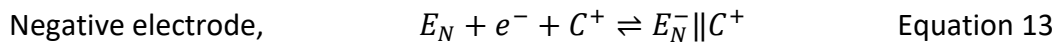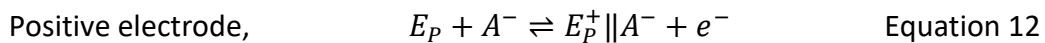

Figure 7: Schematic and equivalent circuit of EDLC [24]. (Reprinted with permission from John Wiley and Sons)

Upon applying a voltage between the electrodes, an excess or deficit of charges on the electrode surface occurs. Subsequently, the counter ions from the electrolyte solution get adsorbed at the interface of electrode/electrolyte and simultaneously proceed on both the positive and negative electrodes forming two EDLs. Therefore, EDLC containing two electrodes can be thought of as two capacitors in series, and the device capacitance can be expressed as:

$$\frac{1}{C_T} = \frac{1}{C_P} + \frac{1}{C_N}$$
<div align="right">Equation 11</div>

where C_T is the total capacitance of the device, C_P is the capacitance in the positive electrode, and C_N is the capacitance of the negative electrode. As the capacitors are in series connection, the equivalent capacitance or the total capacitance of the device is determined by the electrode side that has the smaller capacitance.

The occurring charging and discharging process in the EDLC can be expressed as follows [36]:

Positive electrode, $\qquad E_P + A^- \rightleftharpoons E_P^+\|A^- + e^- \qquad$ Equation 12

Negative electrode, $\qquad E_N + e^- + C^+ \rightleftharpoons E_N^-\|C^+ \qquad$ Equation 13

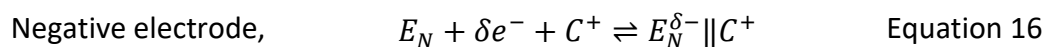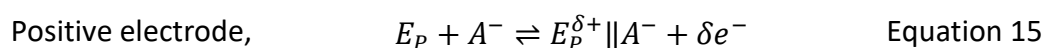Overall charge/discharge, $\quad E_P + E_N + A^- + C^+ \rightleftharpoons E_P^+\|A^- + E_N^-\|C^+ \quad$ Equation 14

where E_P and E_N are the positive and negative electrodes, $\|$ is the interface for EDL formation, A^- is the anion, C^+ is the cation.

During charging, electrons flow from the positive electrode to the negative electrode through an external power source. Simultaneously, ions from the bulk electrolyte solution start getting adsorbed, cations towards the negative electrode, anions towards the positive electrode, forming EDLs. During discharging, the reverse process occurs where electrons flow from the negative electrode to the positive electrode through an external load releasing the stored charge. Meanwhile, the adsorbed ions from the interfaces go back to the bulk electrolyte. The fast electrostatic sorption/desorption of the ions allows high power performance of EDLCs because it does not involve any solid-state diffusion or chemical reaction. The electrolyte concentration remains constant during the process. The observed currents are displacement currents as a result of the rearrangement of charges, and the process is electrostatic and non-faradaic in nature. However, the electrolyte ions that are solvated in the bulk solution get desolvated or partially solvated at the interface, allowing some changes in the chemical bonding. Therefore, technically the entire charge storage mechanism in EDLC is not purely physical [17].

2.4.2 Pseudocapacitor

An alternative charge storage mechanism in ECs involves pseudocapacitance. The difference in the charge storage mechanism of pseudocapacitive materials and EDLC materials lies in the fact that the capacitive charge storage mechanism in pseudocapacitive materials is faradaic in origin. It relies on fast and reversible faradaic redox reactions between the surface/close to the surface of the electrode and electrolyte, where charge transfer occurs across the electrode/electrolyte interface [37]. It is worth noting that not all the faradaic reactions contribute to the pseudocapacitive characteristic in terms of current and potential [38]. For instance, the potential related to the redox reaction that occurs in a rechargeable battery remains ideally constant following the Nernst process. In pseudocapacitive materials, a linear change in the potential (dV) of the electrode changes the charge (dQ) during the redox reactions and results in a measurable capacitance ($C = dQ/dV$), and qualify as pseudocapacitance [15]. The redox reactions are only limited by the surface and not by solid-state diffusion as in the case of batteries. The term "pseudo" adapted to describe pseudocapacitive materials refers to similarity to EDLC behavior even though the origin of the charge storage is different [39].

The occurring charge-discharge process can be expressed as follows:

Positive electrode, $\qquad E_P + A^- \rightleftharpoons E_P^{\delta+}\|A^- + \delta e^-$ $\qquad$ Equation 15

Negative electrode, $\qquad E_N + \delta e^- + C^+ \rightleftharpoons E_N^{\delta-}\|C^+$ $\qquad$ Equation 16

Overall charge/discharge, $\quad E_P + E_N + A^- + C^+ \rightleftharpoons E_P^{\delta+}\|A^- + E_N^{\delta-}\|C^+ \quad$ Equation 17

where E_P and E_N are the positive and negative electrodes, $\|$ is the electrode/electrolyte interface, A^- is the anion, C^+ is the cation and δe^- is the electrosorption valence related to the redox reaction.

The interaction of electrolytes and materials has a strong influence on the different electrochemical processes that contribute to the pseudocapacitance. As shown in Fig. 8 several mechanisms are identified and categorized as follows [40] :
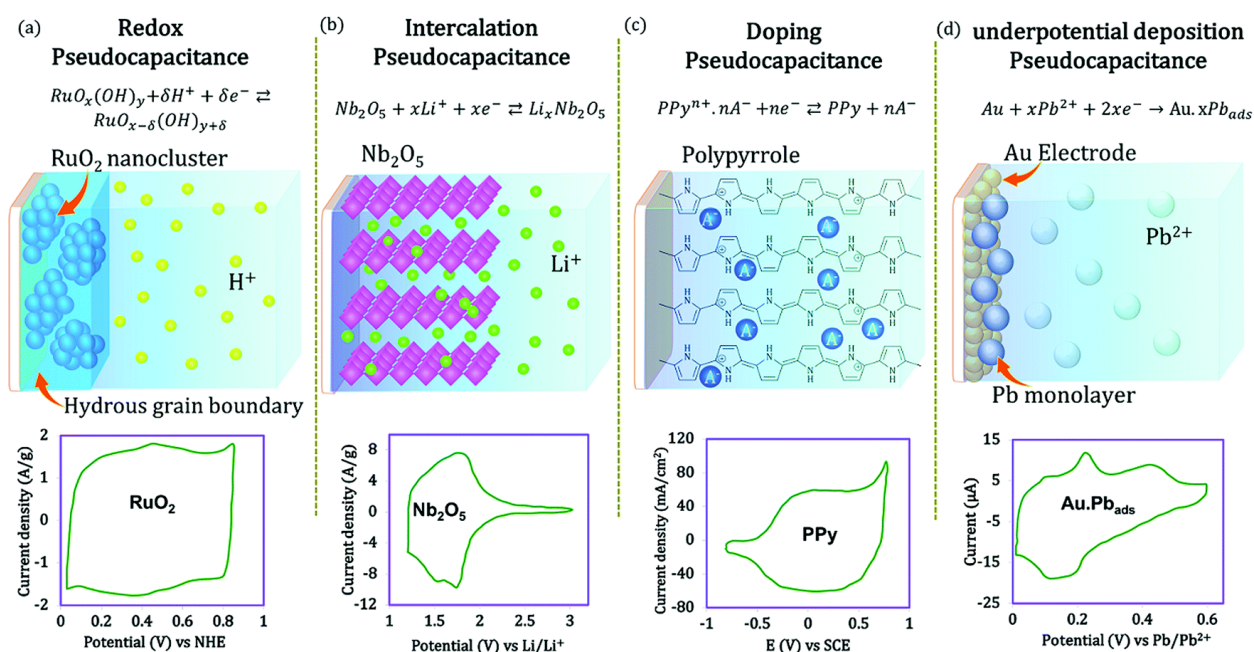
Figure 8: Different redox mechanisms and representative CV for pseudocapacitance [2]: (a) Redox pseudocapacitance, (b) Intercalation pseudocapacitance, (c) Doping pseudocapacitance, and (d) Underpotential deposition. (Reprinted with permission from RSC)

1) Redox pseudocapacitance:

The charge is stored when ions are electrochemically adsorbed onto or near the surface of electrodes with fast faradaic charge transfer reactions (Fig. 8a).

2) Intercalation pseudocapacitance

The charge is stored when ions (*e.g.,* Li⁺, K⁺, Na⁺, or H⁺) reversibly intercalate into the tunnel or layers of a redox-active electrode supplemented by a faradaic charge transfer with no crystallographic phase transformation (*e.g.,* intercalation of Li⁺ on Nb_2O_5) (Fig. 8b).

3) Doping pseudocapacitance

The charge storage involves reversible electrochemical doping and de-doping in conductive polymer-based electrodes (Fig. 8c).

4) Underpotential deposition based pseudocapacitance

Underpotential deposition takes place when metal ions or hydrogen form an adsorbed monolayer at a surface of a noble metal above their redox potential (*e.g.,* deposition of lead on the surface of a gold electrode) (Fig. 8d).

These mechanisms occur as a result of different physical processes associated with different materials. However, the resultant electrochemical signatures are similar because the adsorption /desorption processes occurring at the interface or the inner surface of the materials hold similar dependences between potential and extent of charge and follow a Nernst like equation [37, 40]:

$$E = E^0 + \frac{RT}{nF} ln\left(\frac{1-X}{X}\right) \qquad \text{Equation 18}$$

where E^0 is the standard electrode potential, R is the ideal gas constant (8.314 J mol^{-1} K^{-1}), T is the temperature, n is the number of electrons, F is the Faraday constant (96485 C mol^{-1}), X is the extent of fractional coverage of the surface or inner structure.

The thermodynamic correlation of different mechanisms is listed in Table 2.

Table 2. The Nernst-like equation for different charge storage mechanisms giving rise to pseudocapacitance.

Mechanism	Nernst-like equation	Symbol meaning
Redox	$E = E^0 + \frac{RT}{nF} ln\left(\frac{\Re}{1-\Re}\right)$	$\Re = \frac{[Ox]}{([Ox]+[Red])}$
Intercalation	$E = E^0 + \frac{RT}{nF} ln\left(\frac{1-X}{X}\right)$	X, fractional coverage of lattice sites
Doping	$E = E^0 + \frac{RT}{nF} ln\left(\frac{1-X}{X}\right)$	X, fractional extent of the redox-active site of polymer chain
Underpotential deposition	$E = E^0 + \frac{RT}{nF} ln\left(\frac{1-\theta}{\theta}\right)$	θ, fractional coverage of the surface

As a result of the redox activity on the surface and close to the surface, the pseudocapacitance is 10 to 100 times larger than the EDLC capacitance but usually suffers from lower power density because the faradaic processes are slower than an electrostatic process [15]. In addition, repeated ingression and depletion of ions in the electrode materials can potentially cause alteration of the structure of the electrode materials leading to a reduced cycle life. Typical EDLC can have a lifetime > 10^5 cycles, whereas the pseudocapacitor is limited to ~ 10^3 cycles [41].

Generally, the capacitance of a carbon-based EDLC contains 1-5 % contribution of pseudocapacitance due to the faradaic reactivity of surface functional groups on the carbon electrodes. Similarly, pseudocapacitor also contains 5-10 % of EDL capacitance that is proportional to their electrochemically effective interfacial areas [15].

2.4.3 Hybrid capacitor

As a means to increase the energy content of ECs while maintaining high power and stable cycle life, hybrid capacitors take advantage of both electrostatic and faradaic charge storage mechanisms. Hybridization can be achieved at both the material level and the device level. As long as more than one charge storage mechanism is active, the device can be termed a hybrid. It is worth pointing out that the device containing one pseudocapacitive electrode and one opposite EDL electrode is not considered to be a hybrid as there are only capacitive charge storage mechanisms in play at each interface. Due to the different nature of the electrodes, this configuration can be technically termed an *asymmetric* device. The asymmetric device covers every combination of positive and negative electrodes, including differences in weight, thickness, and type of material. In that sense, hybrid devices can be thought of as a particular case of the asymmetric device where synergistic effects from more than one charge storage mechanism exist [5].
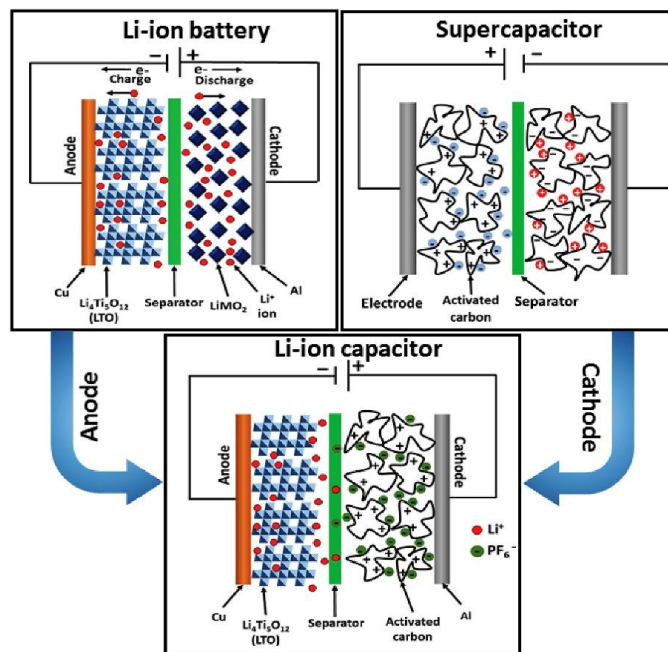

Figure 9: Schematic of charge storage of a Li-ion capacitor [42]. (Reprinted with permission from Elsevier)

The most common hybrid devices contain a battery-type electrode that provides high energy content and a supercapacitor electrode that ensures high power delivery. A typical example of a hybrid capacitor is a Li-ion capacitor (Fig. 9) that contains a porous carbon cathode/positive electrode (follows EDLC charge storage mechanism) and a battery-type anode/negative electrode (follows redox reaction, *e.g.*, insertion, intercalation, or conversion based charge storage mechanism).

During the charging process, electrons move from the positive to the negative electrode through the external circuit while forming an EDL on the positive electrode side where anions get absorbed on the porous carbon, and simultaneously, the negative electrode undergoes Li-ion intercalation. The reverse process takes place during discharging. Due to the contribution of redox activity, the device delivers an energy density of around 20 Wh kg^{-1}, which is significantly higher than that of EDLC but lower than the Li-ion battery. The power density of the device is similar to an EDLC [42]. The overall charge storage mechanism of a Li-ion capacitor is capacitor-like because the cell voltage is mainly controlled by the capacitive potential change at the positive electrode, and the battery-type electrode operates only in a narrow potential window. Therefore, the electrochemical signature is similar to a regular EDLC, and the performance metrics are expressed as for a capacitor.

Another approach for developing a hybrid capacitor involves the usage of redox electrolytes. By replacing the inert electrolyte used in a typical carbon-based EDLC with a redox electrolyte, the charge storage capacity can be increased beyond the electrode/electrolyte interface by utilizing the redox activity of the electrolyte. Redox activity can be implemented both in a battery or an EC as long as the electrodes are conductive enough for the electron transfer to occur between the electrode and electrolyte [6]. In general, redox electrolytes can be categorized in two main ways: redox-active electrolytes, which intrinsically undergo fast electron transfer reactions, and redox-additive electrolytes in which electroactive redox species are added to the conventional electrolytes to introduce a fast reversible redox reaction. Redox electrolytes can also be added to the separator membrane (electrically non-conductive) for preparing redox additive polymer electrolytes [43].
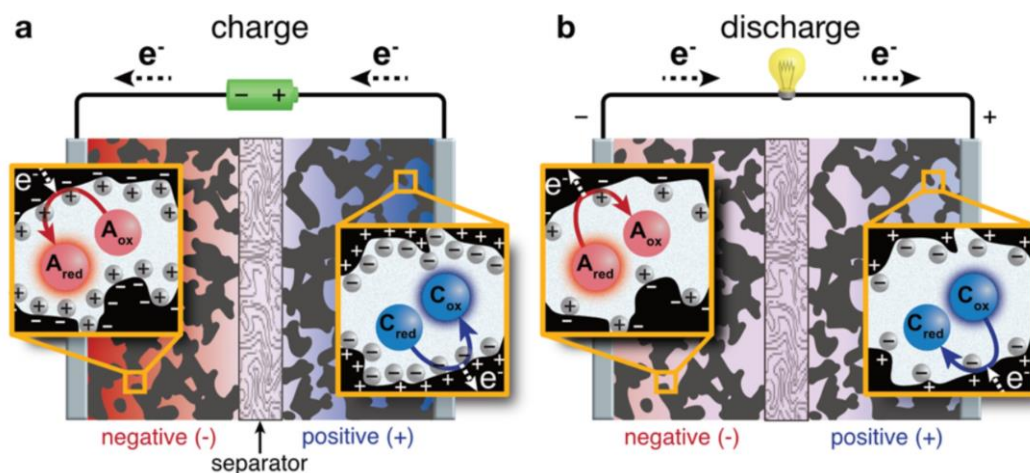
Figure 10: Energy storage mechanism with a Redox process [44]. (Reprinted with permission from Springer Nature)

Fig. 10 demonstrates the charge storage mechanism with redox electrolytes. During charging, oxidizable redox species (known as catholytes) from the redox electrolyte donate electrons at the positive electrode side and get oxidized. Similarly, reducible species (anolytes) accept the electrons at the negative electrode side and become reduced. On discharge, the reversible process occurs. The highest utilization of the redox reactions is restricted to the electrolyte solvent decomposition potential. Microporous carbon electrodes with high surface area provide a large number of active sites in the confined micropores for the electron transfer reactions without diffusion limitations. These diffusionless kinetics provide fast reactions during charging-discharging [45]. Therefore, the devices with redox electrolytes can deliver a high power density, > 1 kW Kg^{-1} (normalized by electrode mass), along with an enhanced energy density, up to 200 Wh kg^{-1} (normalized by electrode mass) [45-49].

The charge storage mechanism of a redox electrolyte containing-device with microporous carbon electrodes is illustrated in Fig. 11, where O and R represent the oxidized and reduced states of the redox species in the electrolyte.
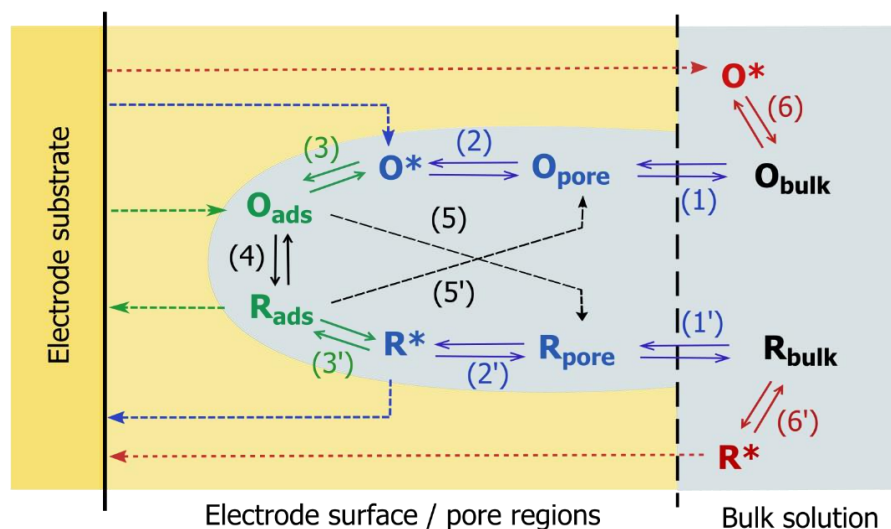
Figure 11: Schematic of charge storage mechanism of a device containing porous carbon electrodes with redox electrolyte.

As a very first step for the charge storage, the redox species in the bulk electrolyte enters the confined pores of the electrode surface with step 1 (for anolyte) and step 1' (for catholyte). Prior to the electron transfer reaction, the redox species go through a transition state with step 2 or 2'. Afterward, a conversion from the transition state to the adsorbed state occurs through step 3 or 3'. In the end, step 4 causes the electron transfer between the adsorbed redox species and the internal or external surface of the electrodes and facilitates high charge storage beyond the electrode/electrolyte interface [50]. There are a few different scenarios that could occur during a charging process. For instance, after step 2 or 2' the redox species from the transition state might directly undergo redox reactions through step 5 or 5' without going through the adsorbed state. It could also happen that upon electron transfer, the adsorbed redox species (O_{ads} or R_{ads}) converts to soluble species (O_{pore} or R_{pore}) through step 5 or 5' and diffuse into the bulk electrolyte through the pore and can not be fully electrochemically recoverable. Both these cases will hardly contribute to the charge storage because the adsorbed redox species (O_{ads} or R_{ads}) would not be present or would be very short-lived. Redox reaction can also take place on the outer surface area through step 6 or 6'. The contribution of this redox activity to the overall charge storage is quite insignificant due to the limited active sites for the electron transfer reaction compared to the internal surface area of the pores.

It is worth pointing out that the redox electrolyte could contain either catholyte or anolyte or both. The KBr electrolyte studied in **Paper I** is a redox-active electrolyte with only one redox-active species, Br_3^- (catholyte). Consequently, the redox reaction occurs only on the positive electrode side. On the negative side, K^+ contributes to a typical EDLC charge storage.

Experimental evaluation

The electrochemical characterization of ECs can be carried through various techniques. Among them, Cyclic Voltammetry (CV), Galvanostatic Charge-Discharge (GCD), and Electrochemical Impedance Spectroscopy (EIS) are the most commonly used techniques. In principle, these techniques measure three fundamental parameters: time, voltage, and current. Consequently, the essential performance metrics of ECs, such as operating voltage window, capacitance, equivalent series resistance (ESR) followed by energy, power, and time constant, can be derived from the variation of these fundamental parameters in one way or another. Each of these techniques holds its advantages for determining some parameters over others. For instance, GCD is particularly useful for deriving capacitance, internal voltage (IR) drop, energy, and power of the device. EIS is suitable for measuring the ESR and differentiating the pure EDLC and pseudocapacitive behavior of the device. The CV is useful for differentiating between capacitive and battery type behavior. The techniques, as mentioned above, could be implemented in both two (full cell) and three-electrode (half-cell) setup. A Three-electrode setup is utilized for fast screening and characterization of the material (electrode, electrolyte) properties, whereas the two-electrode setup is utilized for the validation of the performance under real operating conditions.

3.1 Electrochemical cell design

3.1.1 Two and three-electrode setup

As the name suggests, the three-electrode setup consists of three electrodes containing a working electrode (WE), which is the electrode material under investigation, a reference electrode (RE), a counter electrode (CE), and the electrolyte (Fig. 12b). It is impossible to keep track of the absolute potential of just the working electrode. However, the WE potential can be monitored relative to an included highly nonpolarizable RE. A strict requirement of the RE is that its potential needs to be constant over a broad range of current densities during the experiment. The RE is placed as close as possible to the WE in order to minimize the ohmic potential drop. Commercially available and most commonly used reference electrodes are Ag/AgCl, Ag/Ag$^+$ (Ag in a solution of 10 mM Ag$^+$), saturated calomel electrodes (SCE, Hg/Hg$_2$Cl$_2$/sat KCl), mercury/mercury (mercurous) oxide, mercury/mercury sulfate, copper/copper sulfate. The presentation of data relative to the standard hydrogen electrode (SHE, H$^+$/H$_2$) is quite straightforward, either by subtraction or addition, as the potentials of all these REs are constant

and known. The highly stable constant potential of a RE is achieved by using a redox system with constant concentrations of each participant in the redox reaction. For instance, in the case of Ag/AgCl, the redox reaction happens between Ag metal and its oxidized salt AgCl and can be expressed as:

$$AgCl(s) + e^- \leftrightarrows Ag(s) + Cl^-$$ Equation 19
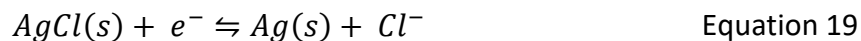
The third electrode in the system is the CE or auxiliary electrode, and the purpose of the CE is to complete the current path between WE and CE. Generally, inert materials like graphite or platinum are used as a CE. Upon power supply from the potentiostat/galvanostat, the current flows through the CE and WE, and the potential is measured between the RE and WE. The three-electrode setup used in **Paper I** consists of a CE (10 mm x 10 mm Pt plate), a RE (Ag/AgCl, 3 M KCl), and a WE (activated carbon).
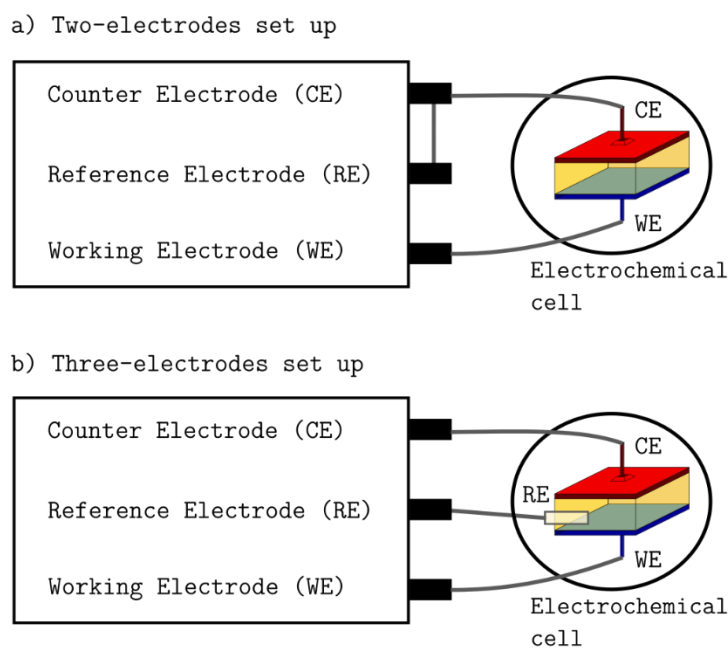
Figure 12: Schematic of (a) two- and (b) there- electrode setup

On the contrary, in a two-electrode setup, the measured voltage is the whole-cell voltage as the RE is shorted with the CE as shown in Fig. 12a. In a symmetrical two-electrode setup, the applied potential differences to the system distribute equally over each electrode. Therefore, for a given applied potential, the electrodes in the two-electrode setup have half the potential of the WE in the three-electrode setup. Generally, commercially available Swagelok cells, coin cells, or pouch cells are used to investigate the electrochemical performance of the whole device. In **Paper I**, a Swagelok cell was used to evaluate the device performance while in **Paper III, IV**, and **V** coin cells were used to the same effect.

3.1.2 T-type Swagelok cell

A T-type Swagelok cell, which is a combination of both three-electrode and a two-electrode setup, was constructed by inserting an Ag/AgCl RE in the middle of the Swagelok cell as shown in Fig. 13. Two potentiostats are required to carry out experiments in this setup, where the 1st potentiostat delivers the perturbation signals to the device and records the voltage between positive or negative electrodes while the 2nd potentiostat records the potential of either positive or negative electrode against the RE. This unique setup facilitates an evaluation of the electrochemical performance of the whole device while simultaneously allowing monitoring the individual electrode within the same experiment and it was used in **Paper I**.
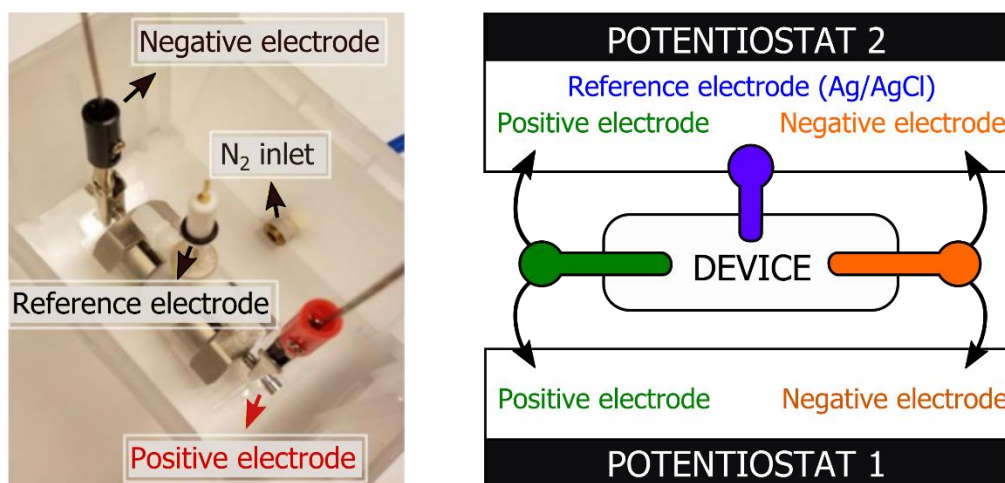

Figure 13: T-type cell and potentiostat connection.

3.2 Evaluation methods

3.2.1 Cyclic voltammetry

Cyclic voltammetry is one of the most used techniques in electrochemistry due to its relative simplicity and ability to reveal a reasonably broad range of qualitative information of the system under study. It applies a linearly changed electric voltage/potential between the working electrode (positive) and counter electrode (negative) in a two-electrode system or between reference and working electrode in a three-electrode system in a predefined operating potential window or voltage window. The change of the voltage relative to time is defined as the sweep rate or scan rate and can be expressed as mV s^{-1}. The scan rate waveform appears to be a triangular shape because of linear shuttling between the two predefined voltage boundaries. By repetitively sweeping the voltage between these two limiting voltage boundaries, the current response of the system can be observed with time. A pair of anodic (increasing voltage) and cathodic (decreasing voltage) sweeps make a cycle, and several cycles can be carried out to

identify the reversibility of the electrode reactions and the mechanistic studies of the processes that are involved in the charge storage.

As the applied voltage in the CV experiment varies linearly with time, the voltage can be expressed as follows:

$$V = V_0 + vt \qquad \qquad \text{Equation 20}$$

where V_0 is the starting voltage, V is the final voltage, and v is the scan rate, and t is time. As at the beginning of the experiment, the starting voltage is zero, therefore

$$V = vt \qquad \qquad \text{Equation 21}$$

Recalling the definition of the capacitance $Q = C \cdot V$ and differentiating relative to time while considering C is constant:

$$\frac{dQ}{dt} = C\frac{dV}{dt} + V\frac{dC}{dt} = C\frac{dV}{dt} = C\frac{d}{dt}(vt) = C \cdot v \qquad \qquad \text{Equation 22}$$

Equation (22) can be simplified as follows:

$$\frac{dQ}{dt} = i\,(current) = C \cdot v \qquad \qquad \text{Equation 23}$$

Equation (23) demonstrates that the current flowing through a capacitor is linearly proportional to the scan rate but independent of the voltage. As the scan rate is positive at an anodic scan and negative at a cathodic scan, the resultant current also changes direction accordingly. Especially when the voltage scan changes its direction in the upper voltage boundary, the current also instantaneously jumps from a positive value to a negative value. It is this feature that creates a rectangular shape when the current is plotted against voltage (*i-V*) [41]. This rectangular shape of the *i-V* plot, also known as cyclic voltammogram (CV) (Fig. 14), is a qualitative measure of the capacitive behavior of the device or material under study. The perfect rectangular shape is a representation of an ideal EDLC.
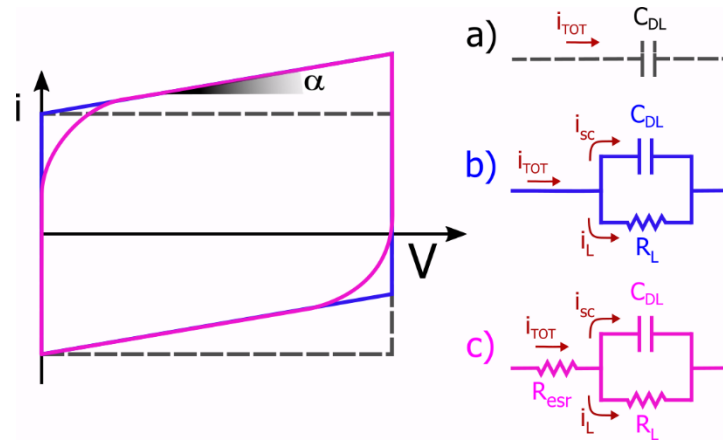
Figure 14: Illustration of equivalent circuits and respective CV plots (a) an ideal EDLC (dashed line), (b) EDLC with resistance (violet line), and (c) EDLC with ESR and resistance (purple line).

Often a slight deviation from the ideal rectangular shape occurs due to the presence of a noninfinite shunt resistance that forces an increasing current with increasing voltage, and the CV plot tilts from the horizontal axis [51]. Also, the presence of ESR, which creates a slow rise in the current with increasing voltage, and a time constant, would round off the two corners of the CV [51]. If the curve rises sharply, it means that the system under study has low ESR.

Materials with pseudocapacitive properties also exhibit a rectangular CV shape. A hybrid system, containing both battery and capacitive type materials, exhibits a quasi rectangular CV with a broad hump associated with the redox reactions considering that the capacitive material dominates the charge storage. If the battery-type material dominates the charge storage mechanism, then there will be a distinct narrow redox peak. A kinetic differentiation can be carried out by observing the dependence of the instantaneous current on the scan rate. The voltammetric response at various scan rates is expressed as:

$$i = av^b$$
<div align="right">Equation 24</div>

where the measured current (i) at a fixed potential follows a power-law relationship with scan rate (v). Both a and b are adjustable parameters, and the value of b is determined from the slope of the plot log (i) vs log (v).

The b-value provides insight into the charge storage mechanism. For pure capacitive process (both EDLC and pseudocapacitance), b=1 as the current is proportional to the scan rate according to Equation (25) [52]:

$$i = av$$
<div align="right">Equation 25</div>

For battery type material, b=0.5 as the response current from the CV is purely diffusion-controlled and proportional to the square root of the scan rate according to Equation (26) [52]:

$$i = av^{\frac{1}{2}}$$ Equation 26

In a hybrid system, the *b* value would be somewhere between 0.5 and 1 as both the surface mechanism related to the electrostatic charging and the diffusion-controlled mechanism related to the intercalation process are happening in the same system. Therefore, the current response at a fixed potential for the mixed process can be expressed according to Equation (27) [53] :

$$i(V) = k_1 v + k_2 v^{\frac{1}{2}}$$ Equation 27

where $k_1 v$ and $k_2 v^{\frac{1}{2}}$ represent the currents related to the surface capacitive process (electrostatic) and the diffusion-controlled intercalation process respectively.

Equation (27) can be rearranged in the following manner,

$$i(V)/v^{\frac{1}{2}} = k_1 v^{\frac{1}{2}} + k_2$$ Equation 28

Both the capacitive and diffusion-limited charge storage mechanisms can be extracted at fixed potential by plotting the scan rate *vs.* current from Equation (28) which gives a straight line with slope k_1 and *y*-axis intercept k_2 [54, 55].

All the important performance metrics such as capacitance, operating voltage window, rate capability, coulombic, and energy efficiency, and cycle life can be directly or indirectly obtained from the CV measurements.

3.2.2 Galvanostatic charge-discharge

The galvanostatic charge/discharge (GCD) technique is used to evaluate the electrochemical performance that mimics practical operating conditions. Unlike cyclic voltammetry, a constant current is applied to the EC device or to the working electrode within a selected voltage range, and the resulting voltage or potential change is recorded with the time that allows collecting information associated with the occurring electrochemical phenomenon at the interface. The overall process includes two steps: charging the device with a constant current followed by discharging at the same magnitude of current, which is similar to the anodic scan and cathodic scan in the CV experiment. Often an additional step (dwelling or potentiostatic holding) is incorporated in the GCD measurements after charging the device to the peak voltage to ensure complete charge distribution in the electrodes. The appearance and shape of the GCD plot can be used to differentiate different charge storage mechanisms. A typical GCD plot of EC, including both EDLC and pseudocapacitor, exhibits a triangular shape due to a linear dependence between the potential and current (Fig. 15). A GCD plot of a hybrid device where battery type behavior dominates displays a nonlinear charging and discharging curve with one or more plateaus (Fig. 15). In the case of batteries, a long steady voltage plateau arises due to the thermodynamic reasons described earlier.
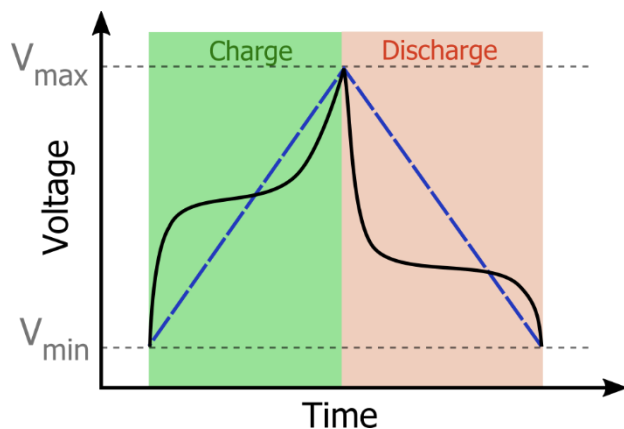
Figure 15: GCD profile of an ideal capacitor (dashed line) and a capacitor with quasi-reversible faradaic reactions (solid line).

The choice of an appropriate current density is crucial to achieving an accurate capacitance measure of the system. For instance, at high current densities, only the outer part of the electrode surface contributes to the overall charge storage mechanism. On the other hand, at low current densities, electrolyte ions have enough time to penetrate deep inside the pores of the electrodes that facilitates the contribution of both the outer and inner surface of the electrodes to the charge storage mechanism and leads to an enhanced capacitance. However, operating the device at extremely low current densities could accelerate unwanted irreversible faradaic reactions that could initiate increased self-discharge. In addition, *IR* drop is directly related to the current density. Therefore, measurements at a wide range of current densities are required to understand the actual performance of the device.

Similar to the CV measurements, all the essential performance parameters of EC devices such as operating voltage limit, capacitance, and IR drop can be depicted from the GCD measurements. Consequently, other properties, such as the rate capability, time constant, power and energy densities, coulombic and energy efficiency, and leakage current, could be derived as well. By continuing GCD measurements for several cycles, the stability of the device can be studied conveniently.

3.2.3 Electrochemical impedance spectroscopy

All the concurring phenomena in an electrochemical cell, such as electrode kinetics, preceding chemical reactions, and diffusion, can impede electron flow and, therefore, could be considered analogous to the essential circuit components like resistors, capacitors, and inductors that describe electron dynamics in an ac circuit. Electrochemical impedance spectroscopy (EIS) measures the impedance of the system at a fixed voltage in a wide frequency range in order to distinguish different frequency responses (resistive, capacitive, inductive) of the device. A low

amplitude AC voltage (typically 5 to 10 mV) superimposed with a steady-state constant DC voltage is applied to perturb the electrochemical cell, and the phase-sensitive current signal is measured in a frequency range of typically 10 mHZ to 100 kHz. Generally, the accumulated data from EIS measurement is expressed as a Nyquist plot, which is also known as a Cole-Cole plot or complex impedance plane plot where a negative imaginary impedance component (-Z") is plotted against a real impedance component at each excitation frequency (Fig. 16a).
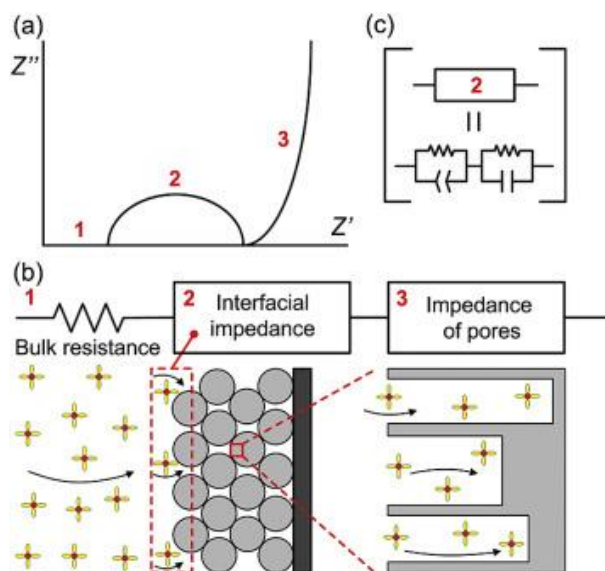

Figure 16: Schematic of the impedance behavior of an EC containing a porous carbon electrode (a) Nyquist plot, (b) Electrode/electrolyte interface and, (c) equivalent circuit [56]. (Reprinted with permission from Elsevier)

Fig. 16 shows the Nyquist plot which consists of three distinct regions: (1) x-intercept at the highest frequency region that originates from a combination of the external circuit resistance, resistance from the separator, and the bulk electrolyte resistance with a dominant contribution from the bulk electrolyte resistance. (2) semi-circle at the middle frequency region that is associated with the interfacial impedance between electrode and electrolyte. (3) a spike at the low-frequency region connected to the intraparticle pores. The first two regions are primarily dependent on the electrolyte solution, whereas both electrodes and electrolytes determine the last region at low frequency. One of the drawbacks of the Nyquist plot is that the frequency does not appear explicitly in the plot. Therefore, often EIS data are presented in a Bode plot where both phase and amplitude can be shown as a function of frequency.

The potential sweep or the current step applied to the electrochemical cell in the CV or GCD measurements shifts the equilibrium condition of the cell, and the transient response is recorded. On the other hand, in EIS, a very small amplitude of AC signal perturbs the cell without destroying

the equilibrium condition. Due to this noninvasive nature, EIS is particularly useful to track the electrochemical behavior over a wide sequence of measurements [57].

Table 3 summarizes the merits and demerits of the different measurement techniques.

Table 3. Comparison of different techniques

Technique	Merits	Demerits
CV	• Fast screening of materials under investigation and revealing degradation processes. • Normalized capacitance evaluation. • Differentiation between different charge storage mechanisms.	• Only kinetic aspects can be revealed, while thermodynamic aspects are neglected.
GCD	• Resembles practical operating condition. • Normalized capacitance evaluation. • Differentiation between different charge storage mechanisms.	• Selecting a proper level of constant current is critical for reproducibility and consistency.
EIS	• Completely nondestructive technique due to usage of small perturbation. • Particularly useful to distinguish the capacitive, resistive, and inductive behavior of the device. • Reveals relaxation time constant. • Differentiation between different charge storage mechanisms.	• Experiment at a very low frequency (less than 5 mHz) is hugely time-consuming. • The experiment above 10^6 Hz often shows a discrete behavior.

3.3 Important figures of merit

3.3.1 Capacitance

Capacitance is the most crucial figure of merit as it defines the efficiency of storing charge in a capacitor and is a reflection of electrical charge storage under a given voltage:

$$C = \frac{Q}{V} \qquad \text{(F)} \qquad \text{Equation 29}$$

Generally, normalized capacitance, C_N is used to compare different capacitors:

$$C_N = \frac{1}{\Pi} \cdot \frac{Q}{V} \qquad \text{(F·}\Pi^{-1}\text{)} \qquad \text{Equation 30}$$

where Π can be the surface area or geometrical area, mass, volume of the individual electrode, or even the whole device. Consequently, the resulting normalized capacitance based on the

above-mentioned parameters is expressed as areal capacitance (F cm^{-2}) or linear capacitance (F cm^{-1}), gravimetric/specific capacitance (F g^{-1}), and volumetric capacitance (F cm^{-3}) [58].

Capacitance can be extracted from all the measurements that are mentioned earlier. The whole CV plot and the discharge curve of the GCD plot are suggested to be taken into account for the capacitance calculation. Accordingly, the specific capacitance can be expressed as:

$$C_{s,CV}(\text{F g}^{-1}) = 4 \times 1000 \times \frac{\int_0^{2\cdot \Delta V/v_s}|i|dt}{2 \cdot m \cdot \Delta V}$$

Equation 31

$$C_{s,GCD}(\text{F g}^{-1}) = 4 \times \frac{I_d \cdot t_d}{m \cdot V_d}$$

Equation 32

where $C_{s,CV}$ is the specific capacitance from a CV plot, i (A) is the current response as a function of time t (s), ΔV is the working voltage range, v_s (mV s^{-1}) is the scan rate, $C_{s,GCD}$ is the specific capacitance from a GCD plot, I_d is the discharge current, t_d is the discharge time, V_d is the voltage range excluding the IR drop, and m is the total mass of both electrodes (in case of a symmetric EC). The factor of 4 modifies the device capacitance (normalized to the mass of two electrodes) to the capacitance of a single electrode.

Capacitance can also be extracted from the EIS measurement according to the following equation [59]:

$$C_{EIS} = \frac{-1}{2\pi f(Z'')}$$

Equation 33

where C_{EIS} is the total device capacitance, f is the frequency in Hz, and Z'' is the imaginary component of impedance. Generally, the lowest frequency applied in the measurement is used to calculate the capacitance [58].

Capacitance can be expressed in terms of complex permittivity and complex impedance in the following manner [60-62]:

$$C(\omega) = C'(\omega) - iC''(\omega)$$

Equation 34

$$= \frac{A}{d} \times [\varepsilon'(\omega) - i\varepsilon''(\omega)]$$

$$C' = \frac{-Z''(\omega)}{\omega \mid Z(\omega) \mid^2}$$

Equation 35

$$C'' = \frac{Z'(\omega)}{\omega \mid Z(\omega) \mid^2} \qquad\qquad \text{Equation 36}$$

where $C(\omega)$ is the frequency-dependent complex capacitance, C' being its real part and C'' its imaginary, A is the geometrical area of the electrode, d is the double layer thickness, $\varepsilon'(\omega)$ and $\varepsilon''(\omega)$ are the real and imaginary part of the complex permittivity, $\mid Z(\omega) \mid$ is the frequency-dependent impedance, $Z'(\omega)$ is the real part of the impedance, $Z''(\omega)$ is the imaginary part of the impedance, and $\omega = 2\pi f$ is the angular frequency.

3.3.2 Energy density and power density

Power density and energy density can be calculated according to the following equations:

$$C_d = \frac{C_{s,GCD}}{4} \qquad (\text{F g}^{-1}) \qquad \text{Equation 37}$$

$$E = \frac{1}{2} \times \frac{C_d \cdot V_d{}^2}{3.6} \qquad (\text{Wh kg}^{-1}) \qquad \text{Equation 38}$$

$$P_{avg} = 3600 \times \frac{E}{t_d} \qquad (\text{W kg}^{-1}) \qquad \text{Equation 39}$$

$$P_{max} = \frac{1}{4} \times \frac{\Delta V^2}{R_s \cdot m} \qquad (\text{kW kg}^{-1}) \qquad \text{Equation 40}$$

where C_d is the specific device capacitance from GCD measurements, E is the energy density, P_{avg} is the average power density, and P_{max} is the maximum power density of the device, R_s is the equivalent series resistance from GCD measurements. The numbers 3.6 and 3600 are unit conversion factors.

3.3.3 Equivalent series resistance

The equivalent series resistance (ESR) is an important parameter as it affects the speed of charging or discharging of an EC. Therefore, a high ESR will restrict the power performance quite significantly, as is shown in Equation (40). The ESR of an EC device is composed of bulk electrolyte resistance, intrinsic resistance from electrodes, contact resistance originating from the electrodes, and current collectors and resistance from external connecting wires. Generally, the electrode materials possess quite high electrical conductivity; thus, the resistive contribution to the ESR is insignificant compared to the resistive contribution coming from the electrolyte. Nonaqueous devices such as organic- ionic liquid- and solid-state electrolyte containing EC suffer quite significantly from the ESR due to their high resistance both in bulk and in the pores of the electrodes. However, with increasing temperature, the ionic conductivity of the electrolyte increases quite drastically. In **Paper II**, we have found that the ESR value of an EC containing an

ionic liquid (EMIm OAc) electrolyte reduces from 2.52 Ω cm^2 at room temperature to 0.37 Ω cm^2 at 150 °C.

Generally, the ESR value is obtained from the Nyquist plot of an EIS measurement. The 1st intercept of the real impedance on the x-axis at the highest frequency is recognized as ESR (Fig. 16). The extent of ESR can also be noticed in a CV plot (Fig. 14c) where high ESR slows down the current rise and rounds of the two corners of the beginning of anodic scan and cathodic scan.

$$ESR = \frac{\Delta V}{\Delta I} = \frac{V_{IR}}{2I}$$ Equation 41

ESR can be obtained from the V_{IR} drop or voltage variation at the initial part of a GCD plot upon applying the Ohm's law (Equation 41).

3.3.4 Rate capability

Rate capability is the ability of an EC to respond to high current densities. Electrodes with fast kinetics, short diffusion pathway, and fast electron transport are the prerequisite of high rate capability and superior power performance. Macropores present in the porous carbon facilitate a short ion diffusion pathway to the internal surface; mesopores offer low resistance for the ions to diffuse through the material, and micropores provide the inherent EDL capacitance. In this regard, hierarchically porous carbon electrodes are particularly well suited to achieve an excellent rate capability of an EC.

Rate capability can be calculated from both CV and GCD measurements. In CV, rate capability is a function of capacitance at different scan rates, and in GCD, it is a function of the capacitance at different normalized current densities. Generally, the maximum capacitance is achieved at a low scan rate or at a low current density. With increasing scan rate or current densities, the capacitance diminishes as the inner portions of the active material hardly contribute to the charge storage mechanism. Therefore, electrode materials with a high surface area and suitable pores with good interconnection are essential.

3.3.5 Coulombic/energy/voltage efficiency

Coulombic efficiency is the ratio of stored charge that is drawn out of the EC device during a discharge step to the accumulated charge during a charge step. A high coulombic efficiency over a period of cycling is an indicator of the EC device stability. Similar to Coulombic efficiency, energy efficiency is also a crucial parameter and it is defined as the ratio of energy drawn out from a device to the energy needed to put back the device in its original state of charge. It is recommended to use energy efficiency over coulombic efficiency for a hybrid device to demonstrate the effectiveness of the device [50]. Voltage efficiency is simply the ratio of

discharge voltage to the charge voltage of the device [2]. Generally, all these efficiencies can be extracted from a GCD plot, as shown in Fig. 17.
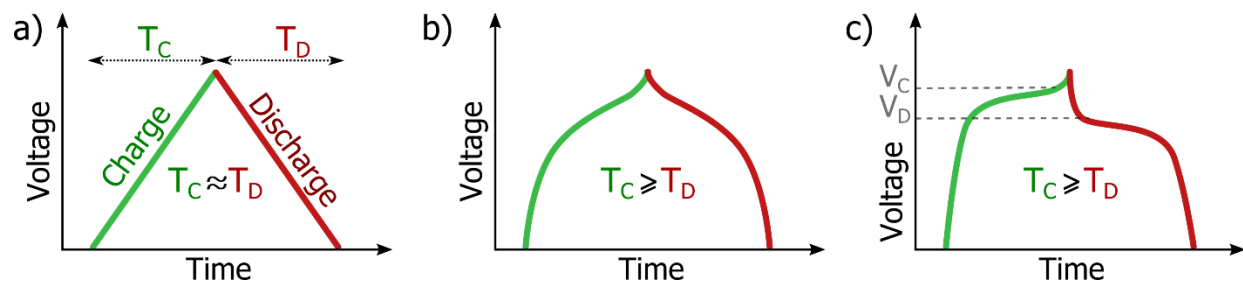

Figure 17: Schematic demonstration of (a) coulombic (b) energy and (c) voltage efficiency of EES devices.

It can be seen that when the charge-discharge profile is perfectly symmetric and triangular, as it should be for a perfect EDLC, the coulombic efficiency can be extracted from the x-axis (Fig. 17a). If the current used in the GCD measurement is constant and the same for both charge and discharge, then the coulombic efficiency can be simply calculated from the discharge time and charge time. In a hybrid device involving a plateau in the charge-discharge profile, one has to consider the information from both the x and y-axis (Fig. 17b). Voltage efficiency is obtained from the information related to the y-axis (Fig. 17c).

3.3.6 Cyclic stability

High stability is one of the most attractive features of the EC. Generally, device stability is compromised in terms of capacitance reduction or an increase of ESR over time [63]. The capacitance degradation occurs due to the reduction of the active surface area as a result of pore blockage that originates from the decomposition products from the electrolyte or the formation of surface functional groups [64, 65]. ESR increases due to the adherence of the decomposition products in the separator or on the electrode surface or by increased contact resistance between the electrodes and current collectors [65, 66].

Generally, a cycling test is carried out by repetitive charging-discharging with the GCD measurement over several thousand cycles, and the capacitance retention (ratio of the capacitance at the end cycle to the initial cycle) is used as a quantitative measure of the stability. Commercial devices show a cycle life of one million or more at nominal conditions (cycling between 0 V to a nominal voltage at room temperature) [67]. Capacitance retention to below 80 to 70% over a period of cycles and a 100% increase in the internal resistance of the device is considered to be the end of life [2, 66, 68, 69]. Generally, the ESR reaches the end of the life limit earlier than capacitance [70]. An alternative stability test involves voltage holding at the nominal voltage over a period (also known as floating) followed by occasional charge-discharge or EIS measurements throughout that period to keep track of the aging process [71, 72]. The cyclic test

mimics the duty cycle of an EC application, whereas the floating test reflects the conditions for the applications where EC is used as an emergency or backup device ready to operate on spontaneous demand [67].
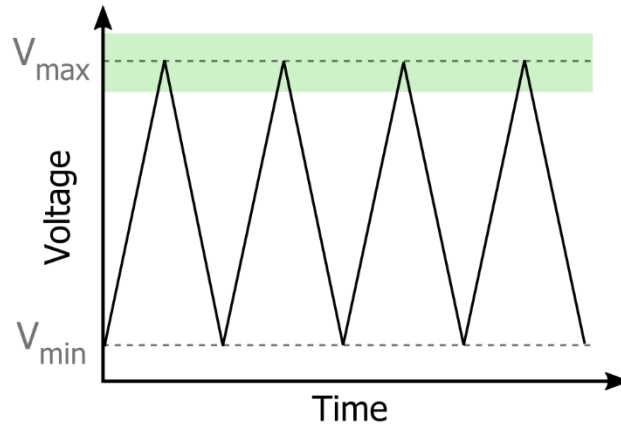

Figure 18: Schematic of voltage during cycling (solid line) and floating (dotted line in green area) test.

As can be seen in Fig. 18 during the cyclic test, the device is exposed to the nominal voltage (green area) for a very short period of time. Therefore, it will require a considerable amount of cycling before the end of life, which could be very time-consuming. On the other hand, during the floating test, the device is continuously exposed to the nominal voltage and will require a shorter time to reveal the end of life of the device and is highly recommended for the device stability measurement [67].

3.3.7 Self-discharge

The spontaneous voltage drop of a fully charged EC when it is not connected to any external power supply is known as self-discharge and is crucial for the preservation of stored energy. The current required to keep the state of charge of the ECs is known as leakage current. High leakage current is detrimental to the ECs when it is a standalone device or is aimed to be integrated into a miniaturized self-powered system where the power harvested from the energy harvesters is often very low (10-1000 µW) [73]. Therefore the amount of available current to charge an EC is also very limited, which could be in µA or even nA range. High leakage currents will require a long time to charge the EC; if the leakage current is higher than the charging current, the device cannot be charged at all.

In an open circuit configuration, the state of charge of an ideally polarizable capacitor remains stable indefinitely because there is no pathway for the current to leak. In reality, due to construction flaws of the EC or components containing impurities, there exist some pathways through which current leaks and the voltage drops over time [12]. The equivalent circuits of an

ideal capacitor (Fig.19a) and leaky capacitor (Fig.19b) can be expressed in the following manner, where a potential and time-dependent leakage resistance (R_L) arises parallel to the double-layer capacitance in the leaky capacitor [74, 75].
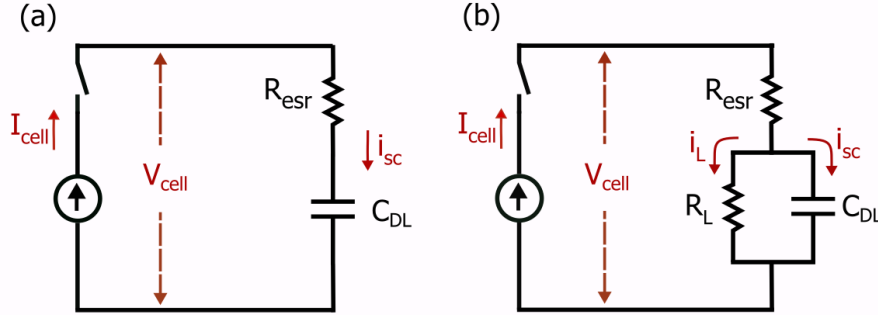

Figure 19: Equivalent circuits of ECs (a) ideal capacitor without leakage and (b) leaky capacitor with self-discharge or leakage current.

Under constant charging in an ideal capacitor, the potential distributes across the whole circuit (Fig.19a) as

$$V_{cell} = I_{cell}R_{ESR} + V_{C_{dl}}$$

Equation 42

where V_{cell} is the cell voltage, I_{cell} is the applied current, R_{ESR} is the equivalent series resistance and $V_{C_{dl}}$ is the voltage across the double-layer capacitor.

For a constant applied voltage V, the time-dependent charging current can be calculated as

$$I_t = I_i \exp\left(-\frac{t}{R_{ESR} \cdot C}\right)$$

Equation 43

where I_i is the initial current at $t \rightarrow 0$, and the charging current decreases exponentially in time.

In the case of the capacitor with a leakage pathway (Fig.19b), the charging current gets distributed into two components: one component I_{SC} is solely responsible for charging the C_{dl} and the other component I_L, the self-discharge current equivalent to the leakage current, is related to the voltage across the double-layer capacitor $V_{C_{dl}}$ and the leakage resistance R_L at a given state of charge of C_{dl}. When R_L is significantly higher than the R_{ESR} then there will be a very slow self-discharge, and the charging will follow the ideal capacitor according to Equation (43). When R_L is significantly lower than the R_{ESR} most of the currents pass through the R_{ESR} and the self-discharge rate would be very high, requiring a high float current or leakage current to keep the state of charge. Generally in practical devices, an intermediate state arises where some part of the current is responsible for charging the C_{dl} and a parasitic fraction passes

through the R_L.With increasing voltage $(V_{C_{dl}})$ the leakage current (I_L) through the leakage resistance (R_L) tends to increase [74].

Performance enhancement

4.1 Boosting energy density of an aqueous system with redox electrolyte

4.1.1 Conventional organic and aqueous electrolytes

As the energy density is directly proportional to the capacitance and square of the voltage, it is highly beneficial to extend the operating voltage along with the capacitance. Generally, the operating voltage largely depends on the electrochemical stability window of the electrolyte or solvents. Currently, electrolytes with organic solvents such as propylene carbonate (PC), acetonitrile (ACN), and dimethyl carbonate (DMC) are used in commercial SCs, which offers a large voltage window of 2.5 -2.7 V owing to their high electrolysis resistance [68]. However, the organic solvents are highly volatile, flammable, and toxic making them very unsafe. Besides their inferior ionic conductivity and low diffusion rate result in increased ESR, which adversely affect their capacitance and power performances [76].

On the other hand, aqueous electrolytes-based devices offer a tremendous potential regarding long-term industrial application because of their convenient fabrication at ambient conditions, prominent safety, earth-abundance, and low cost. Moreover, small-sized ions in an aqueous electrolyte offer an extraordinary ionic conductivity that provides high capacitance and power density. The most commonly studied aqueous electrolytes such as H_2SO_4 and KOH have ionic conductivities of 850 and 620 mS cm^{-1} respectively, which is significantly superior to the ionic conductivity of around 100 mS cm^{-1} for organic electrolytes [77, 78]. However, the practical applications of aqueous-based devices are still limited due to their low operating voltage, at 1.23 V as set by the thermodynamic stability of water. Applying a potential difference outside this range will produce H_2 gas in the negative electrode resulting in the hydrogen evolution reaction (HER) and O_2 gas in the positive electrode resulting in the oxygen evolution reaction (OER) [79].

One strategy to increase the operating voltage range of the aqueous system is to take advantage of the overpotential of HER and OER within the steady-state of the electrodes followed by full utilization of the capacitive potential range (CPR) of individual electrodes. By adopting this strategy, a high operating voltage of 1.6 V was achieved in an acidic media of 1 M L^{-1} H_2SO_4 through an asymmetric system containing activated carbon electrodes with either mass balanced or different oxygenated surface functional groups [80]. Although an effective utilization of high

overpotential for di-hydrogen evolution increased the working voltage range, the highly corrosive nature of H_2SO_4 to current collectors prevents large-scale industrial applications. Cost-efficient and non-novel metal current collectors that are resistant to strong acid corrosion are a big challenge [81].

In contrast, aqueous electrolyte with a less corrosive nature, for instance neutral media, is a more promising solution. Moreover, the overpotential for both HER and OER is higher in neutral electrolytes than in acidic or basic electrolytes [82]. The large overpotential in the neutral media arises due to several reasons. Firstly, the HER and OER are less favored because the concentrations of proton H^+ and hydroxide ions OH^- are extremely low [83]. Secondly, both the cations and anions are strongly bounded by H_2O molecules forming hydrated ions, and it takes extra energy for the H_2O molecules to leave from the hydrated ions, which contributes to the overpotential [83]. Thirdly, electrosorbed hydrogen in the micropores of the carbon electrodes stays strongly attached to the surface, and an excess potential (overpotential) is needed to overcome the additional free energy for HER to occur [84, 85]. By utilizing all these phenomena, a symmetric carbon/carbon SC utilizing Na_2SO_4 could reach up to 1.6 V working voltage [86]. Even a higher operating voltage of 2.2 V has been reported for a carbon-based SC containing Li_2SO_4 electrolyte [81].

4.1.2 Opportunities with redox electrolyte:

Although neutral electrolytes can facilitate a high operating voltage their capacitance is still inferior compared to acidic or basic electrolytes containing devices [76]. Therefore, improving the capacitance along with the high operation voltage would go a long way to achieve an extraordinary energy density. One strategy to improve the capacitance is to use redox electrolyte in combination with electrochemically inert neutral electrolyte, where soluble redox couples add faradaic charge storage on top of the electric-double layer capacitance. In order to have optimal performance, ideally, the standard potential for redox species should be near the potential of OER (for catholytes) and HER (for anolytes) [44].
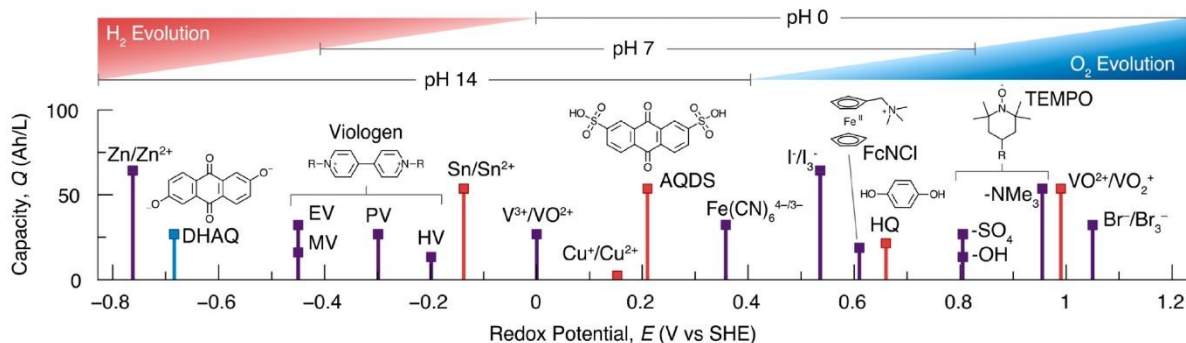
Figure 20: Redox potentials and volumetric capacity of selected redox couples in aqueous electrolytes used in redox ECs, flow batteries, and redox batteries. Electrolytes illustrated in red, blue, and purple operate in acidic, basic, and neutral conditions [87]. (Reprinted with permission from American Chemical Society)

Among the different redox species reported in the literature, as can be seen from Fig. 20, Br^-/Br_3^- redox couple has the highest electrode potential of 1.05 against standard hydrogen electrode (SHE), which is 0.23 V higher than the standard potential for OER (0.82 V) at pH 7. Taking into account the large overpotential in a neutral electrolyte (pH 7), Br^-/Br_3^- catholyte is a perfect fit to adopt a large voltage window with enhanced capacitance.

In **Paper I**, we demonstrate that neutral KBr electrolyte can provide a large voltage window of 1.9 V in a symmetric configuration with activated carbon electrodes.

In order to find out the optimal potential range in the KBr electrolyte, the three-electrode setup is utilized with Ag/AgCl as a reference electrode (3 M KCl, 0.21 V *vs.* NHE). The cathodic and anodic scan of CV with incremental potential can be seen in Fig. 21. Cathodic scan in the negative potential region (Fig. 21 a) increases continuously with the voltage increment. However, no significant current rise is observed until -1.30 V *vs* Ag/AgCl. Similarly, quasi-rectangular CV on the positive potential region (Fig. 21 b) without significant increase of anodic current is maintained from 0 to 0.65 V. Beyond that positive potential limit, a noticeable redox activity of Br^-/Br_3^- is present. Therefore, the capacitive potential range of KBr electrolyte is roughly assigned from -1.30 V to 0.65 V *vs* Ag/AgCl. For a full cell (two electrodes) operation, the operating voltage window would be 1.95 V, which is much higher than the thermodynamic voltage limit for the water decomposition.
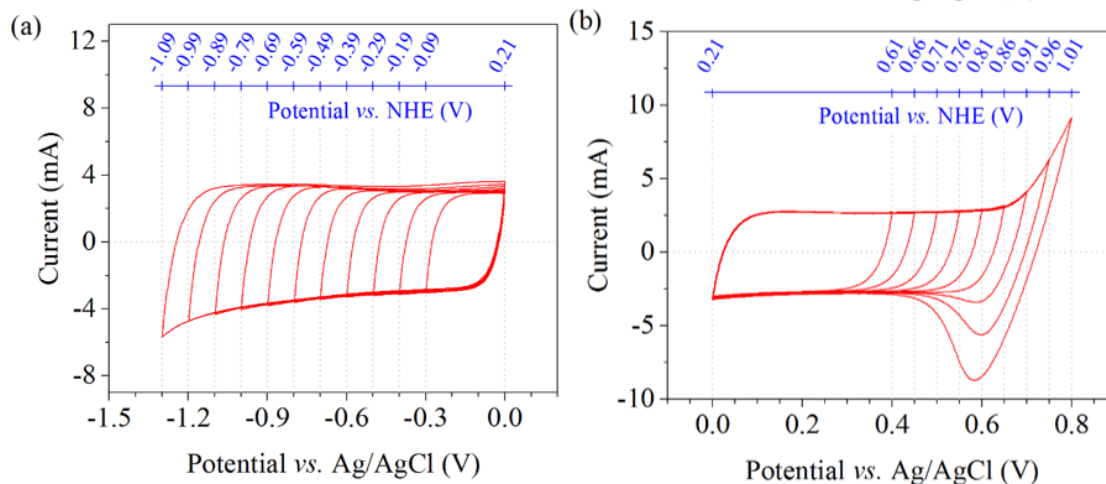
Figure 21: CV scans in a three-electrode cell containing 1 M KBr electrolyte at a scan rate of 20 mV s^{-1} (a) Negative and (b) positive potential region (**Paper I**).

However, when the device performance are characterized with CV (Fig. 22 a) and GCD (Fig. 22 b) in a full cell setup (Swagelok cell), it can be noticed that the rectangular shape of the CV curve and the near-perfect triangular shape of the GCD curve are maintained until 1.6 V, indicating that the device is principally EDLC until 1.6 V. From 1.7 V onwards the current response and the voltage response both deviates from the ideal shape due to redox reaction turning the device into redox-EDLC or hybrid device. It is worth pointing out that even though the concept "capacitance" does not apply to a hybrid device, practically it could be used in this case where EDL behavior still dominates over pure battery type behavior (sharp redox peak in CV and long plateau in GCD plot).
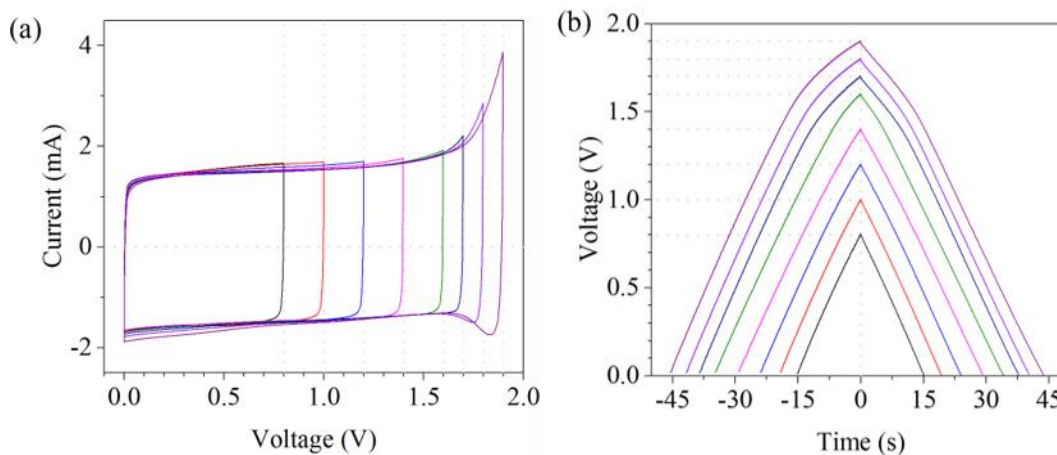

Figure 22: (a) CV scans at 20 mV s^{-1} and (b) GCD profile at 1 A g^{-1} of KBr containing device with incremental voltage increase from 0.8 to 1.9 V (**Paper I**).

Even though a large capacitive potential range (CPR) of more than 1.9 V is depicted from the three-electrode setup, redox activity already starts at 1.7 V during the device operation, suggesting that the point of zero voltage (*PZV*) is not positioned in the middle of the CPR. And there is a shift in the electrode potential limit for the positive electrode (*PL*) and the negative electrode (*NL*). The observation can be more explicitly seen when the devices are cycled at different operating voltages and is further verified by a T-type Swagelok cell by monitoring the potential shift of individual electrodes (**Paper I**). The shift of (*PZV*), (*PL*), and (*NL*) is explained speculatively in terms of electro-oxidation of the positive electrode and slow kinetics of redox reaction.
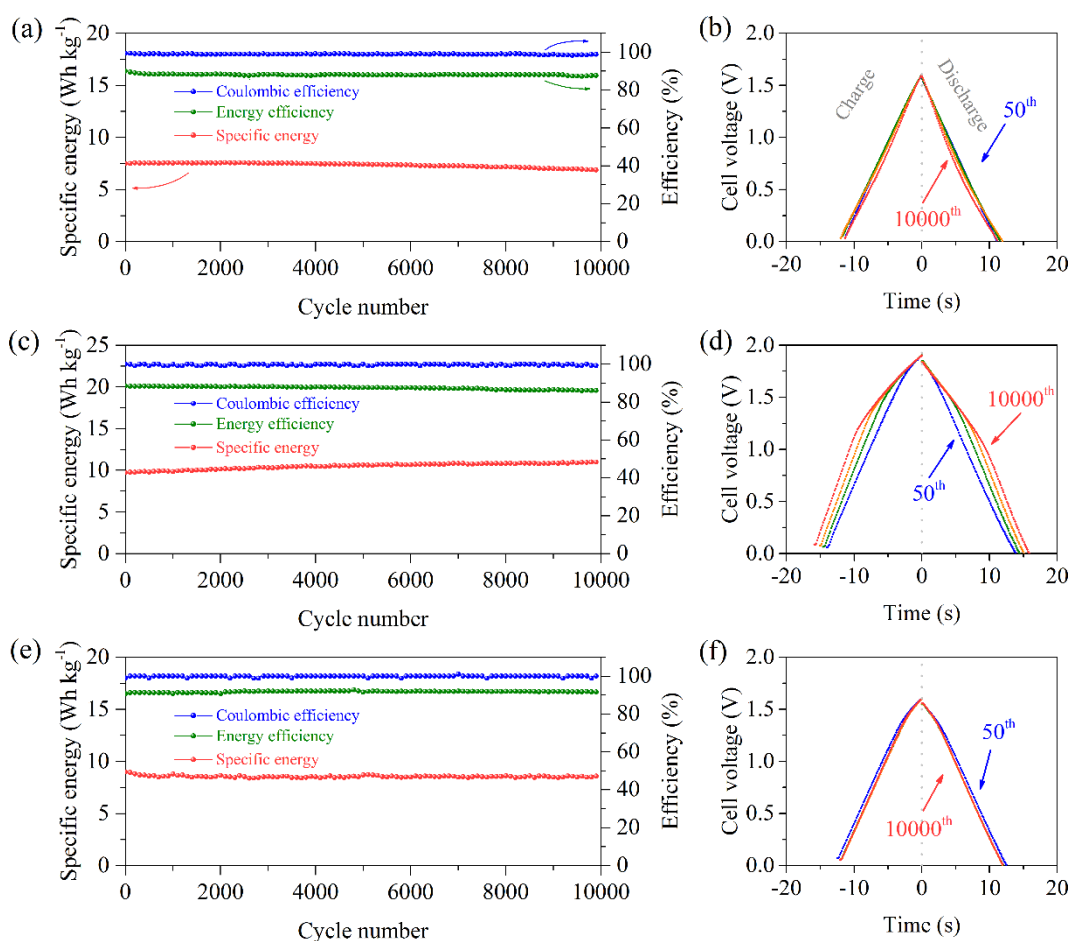
Figure 23: Cycling stability and GCD curves at selected cycle numbers of two-electrode Swagelok® cells operating at 1.6 V (a, b), 1.9 V (c, d), and 1.6 V after triggering operation (e, f) (**Paper I**).

Fig. 23 demonstrates the capacitive performance and charged/discharged behavior for 10,000 cycles at different operating voltages, namely direct polarization to 1.6 V (Fig. 23 a, b), direct polarization to 1.9 V (Fig. 23 c, d), and polarization to 1.6 V after pre-cycling at 1.9 V for 500 cycles (Fig. 23 e, f). As can be seen from Fig. 23 (d) that the deviation from linearity in the GCD profile is

occurring at lower and lower voltages with cycling. Consequently, at the end of the 10,000th cycle, the linear deviation is occurring already at 1.2 V, which means that at this point the redox activity can be utilized at a cell voltage lower than 1.7 V. We term this feature as "triggering operation/effect". The triggering effect gives an interesting aspect of manipulating redox activity by pre-cycling the device at 1.9 V, which afterward can be utilized at lower voltages. It is worth pointing out that although the redox activities at high voltage enhance the energy density by contributing additional energy to the EDLC but simultaneously decrease the rate capability. For instance, a high rate capability (capacitance retention at 15 A g^{-1} relative to 1 A g^{-1}) of 92 % is observed for the device polarized at 1.6 V while the rate capability dropped to 81 % during 1.9 V operation. Therefore, proper utilization of redox activity is necessary in order to have both high energy density along a high power performance.

In this regard, Fig. 23 (e, f) demonstrates increased energy with a minimum sacrifice of power. The initial specific capacitance and energy density at 1.6 V after pre-cycling are 97 F g^{-1} and 9.0 Wh kg^{-1}, corresponding to a 22 % increase based on the results in Fig. 23 (a, b) before pre-cycling, which is around 85 F g^{-1} and 7.4 Wh kg^{-1} for pure EDLC. Although the rate capability (88 %) is slightly lower than the pure EDLC it is still significantly higher than the value when redox activity is heavily involved at 1.9 V. Another advantage of manipulation of the redox activity is to reduce the risk of current collector corrosion, especially relevant when stainless steel collectors are used in halogen-containing systems [88].

4.2 Thermal influence on ECs

4.2.1 Adverse effect due to high temperature:

Many applications require a wide range of temperature stability of the ECs. Without good temperature compatibility, the deterioration of all the structural components of the device including electrodes, electrolytes, and separators is inevitable. Consequently, occurring of some adverse effects, such as pressure evolution, oxides formation, electrolyte evaporation, self-discharge rates increase, are very common that accelerate the device aging [89]. As the device ages, the decrease of capacitance and increase of ESR leads to an even higher margin of temperature fluctuation. Aging rate increases by a factor of 64 by either increasing the temperature by about 40 °C above room temperature or by charging to a voltage of 200 mV above the rated voltage [90]. Moreover, temperature differences in systems with large SC modules (connected in series or parallel) could initiate voltage imbalance and results in overvoltage of individual devices that could destroy the whole system. Even devices aimed for room temperature application can be exposed to elevated temperature upon repetitive charge/discharge as a portion of the electrical energy gets lost as heat [91]. Of course, the heat generation rate depends on the device design, material properties, and operating conditions but

generally, the security and performance reliability of SCs are still overwhelmingly threatened at elevated temperature. At the current state of technology, heat generation in SCs is handled by thermal management systems within an EC pack. They are designed to maintain a set average temperature with uniform temperature distribution. However, this adds additional volume and mass as well as the cost to the whole system let alone reduced reliability. Moreover, it is contrary to one of the main striking features of SC– low maintenance.

4.2.2 High-temperature influence on the components

Among all the constituents in a device, the electrolyte is the most vulnerable at off-design temperature. For instance, at low temperatures, both the energy density and power density reduces because of lowered ionic conductivity of the electrolytes. Similarly, at high temperatures, a series of side reactions accelerate the decomposition of the electrolyte and shorten the lifetime of the device [92]. Therefore, a thermally and electrochemically stable electrolyte is highly crucial for performance and reliability. Fig. 24 demonstrates the temperature influence on the physiochemical properties of the electrolytes and their correlation with the capacitive performance and can thus be a good reference frame for scrutinizing electrolytes in a wide temperature range [90].

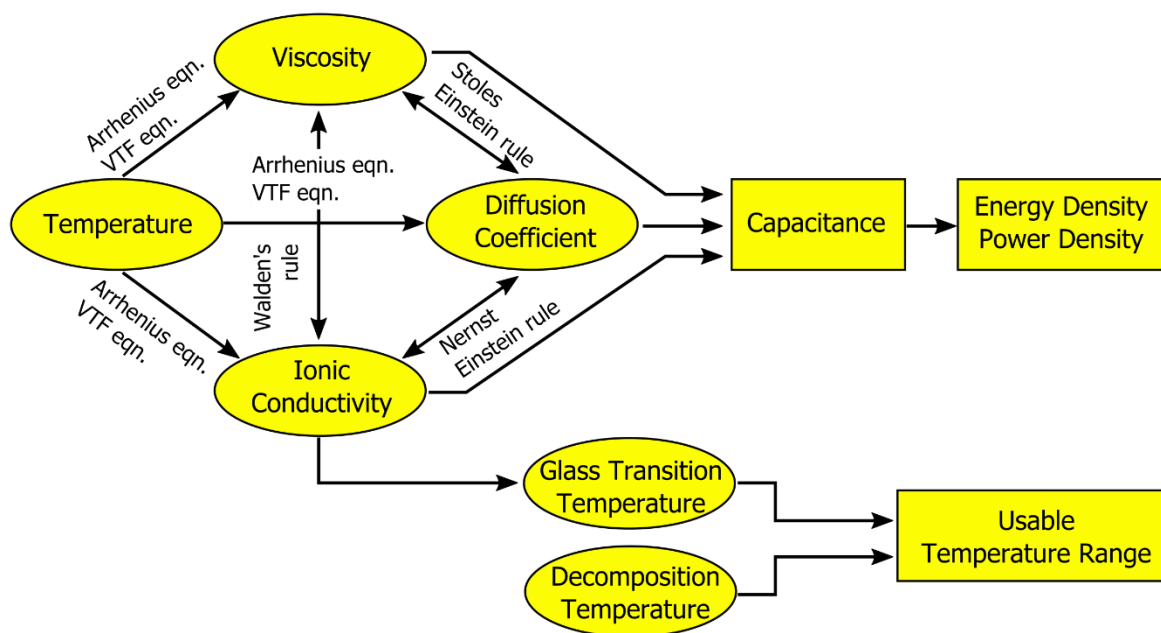Figure 24: Relation network of temperature and different thermophysical properties of electrolytes. The numbers and arrows in the network represent specific relations among different parameters. (Reproduced with permission from Springer)

Generally, the commercial supercapacitors containing organic electrolytes are rated in the temperature range of -40 to 70 °C. Both the typical solvents used in the organic electrolytes, ACN

and PC are prone to be affected by elevated temperatures [93]. Especially, ACN possesses a low boiling point (80 °C), low flash point (around 5 °C) and therefore not recommended to be used at a temperature above 70 °C [94]. The concern is mainly due to its high toxicity and flammable nature. If there is thermal, mechanical, or electrical abuse ACN could generate highly toxic gas like hydrogen cyanide. In some countries such as Japan, ACN is not even allowed to be used in supercapacitors due to its severe safety concern [90]. Aqueous electrolytes are also not very suitable in the high-temperature operation due to the low boiling point of water and are not recommended to be used more than 80 °C [90].

4.2.3 Prospect of IL at high temperature:

In this regard, solvent-free IL electrolytes are very promising for high-temperature application due to their low flammability, low volatility, negligible vapor pressure, and high electrochemical stability in a wide range of temperatures [95]. The salts which solely consist of cations and anions with a melting point below 100 °C are categorized as ILs or room temperature molten salts [95]. They are composed of bulky, asymmetric organic cations and weakly coordinating inorganic/organic anions. This unique combination of large cation and charge-delocalized anion prohibits an easy formation of an ordered crystal structure, which is responsible for their low melting point. By taking different combinations of cations and anions their physical and chemical properties can be tuned virtually unlimited way, which is a very attractive feature for an electrolyte [10]. For instance, electrolyte composition can be tailored in such a way that they meet certain requirements needed for EC, such as high operating voltage, or high ionic conductivity (reduced ESR), or a wide temperature range. Generally, ILs are classified into three types, aprotic, protic, and zwitterionic based on their composition that are suitable in different applications [95]. Aprotic ionic liquids based on pyrrolidinium and imidazolium cations are widely used in ECs. Imidazolium-based ILs have low viscosity and high ionic conductivity whereas, pyrrolidinium-based ILs are more stable against oxidation and reduction that provides a large electrochemical stability window [96]. Therefore, a trade-off has to be taken into account depending on the specific requirements.

Besides the attractive features, ionic conductivities of ILs are still quite low compare to aqueous or organic electrolytes. For instance, EMIm BF$_4$ IL with one of the highest ionic conductivity among commonly used ILs has an ionic conductivity of 14 mS cm^{-1} at 25 °C, which is considerably lower compared to a typical organic electrolyte TEABF$_4$/ACN with ionic conductivity of 59.9 mS cm^{-1} at 25 °C [10]. However, at high temperatures, the electrostatic interaction between the cations and anions becomes weaker which decreases viscosity quite remarkably. A viscosity decrease by a factor of 32 from RT to 120 °C was reported for an acetate-based IL [97]. It has been also shown that the best performance of IL can be achieved around 60 °C [90].

Taking all these properties into account, ILs are ideal candidates for high-temperature operation and their thermal stability could reach as high as 300-400 °C with negligible vapor pressure [95]. Although the presence of impurity or water content can compromise their electrochemical or thermal stability in principle, they can function well as long as the operation is carried out under the decomposition point. However, it is worth pointing out that at extremely high temperatures the interaction among the different components becomes very critical that will lower the thermal tolerance of the electrochemical operation of the device compared to the thermal tolerance of pristine IL.

In **Paper II**, we have carried out a thorough electrochemical characterization of EC containing EMIm OAc IL in a wide temperature range of RT to 150 °C. Although thermal gravimetric analysis shows that the thermal degradation of EMIM OAc occurs around 240 to 250 °C, electrochemical measurements reveal a considerable deterioration already at 150 °C. Moreover, at extremely high temperatures, the difference in the thermal expansion coefficients of different materials can be quite prominent. Therefore, typical test cells such as a Swagelok cell, which contains stainless steel current collector attached to a Teflon body will loosen the contact between the electrodes due to a mismatch in the thermal expansion coefficients. A Coin cell is also not suitable at extremely high-temperature operation because the encapsulation will wear out due to high pressure that builds up in the cell with temperature, in addition to the thermal instability of the plastic gasket ring that keeps the two electrodes separated. Therefore, a specially designed test cell is required for operation above 100 °C, as shown in Fig. 25, which we designed and used for the experiments in **Paper II.**
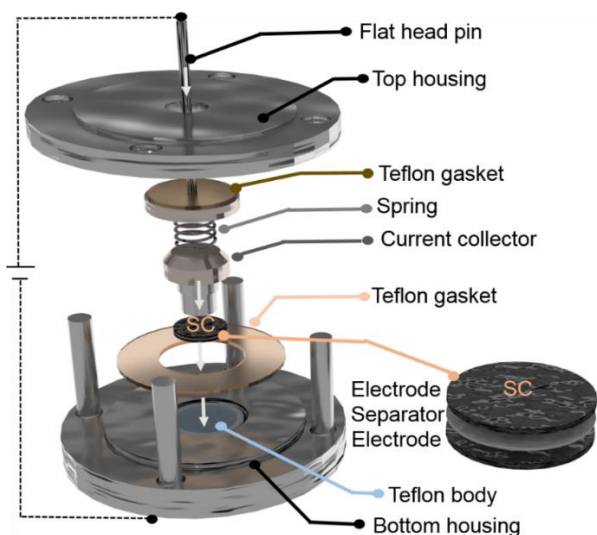

Figure 25: Schematic of the customized chamber and SC cell assembly for high-temperature operation (**Paper II**).

The customized cell chamber consists of two housings (top and bottom) made of stainless steel. The housings connect one side of the SC sandwich to the external power supply. The other side of the sandwich is connected to the power supply by a flat head pin (made of stainless steel) through the top housing. A thin Teflon gasket between the top housing and the flat head pin avoids any short circuit with the rest of the housings. An inner Teflon body inside the cavity of the bottom housing keeps the sandwich separated from the cavity wall and makes sure that the external connection is maintained only by the flat head pin through the top housing. A thin Teflon gasket on the surface of the bottom housing provides isolation for the piston-shaped current collector attached to the flat head pin with a stainless steel spring, which essentially compensates for the mismatch in the thermal expansion issues at elevated temperatures.

Table 4 Performance metrics of the supercapacitor from GCD measurements (**Paper II**)

Temperature (°C)	Max. voltage (V)	IR drop [a] (mV)	Useable voltage (V)	Energy density (Wh kg^{-1})	Max. Power density (kW kg^{-1})	Rate capability (%)	Capacitance [b] (F g^{-1})
RT	1.5	186	1.31	4.3	4.6	62	84
40	1.5	79	1.42	6.1	12.8	78	98
80	1.5	35	1.46	8.3	30.5	82	122
100	1.4	29	1.37	7.3	32.5	85	121
120	1.4	26	1.37	7.4	36.0	85	121
RT/120	1.5	134	1.36	4.9	6.9	66	88
150	1.3	23	1.28	7.7	35.6	87	142

[a] IR drop at 3 A g^{-1}

[b] Maximum capacitance is achieved at 1 A g^{-1} while 2 A g^{-1} for 150 °C

Different electrochemical measurements CV, GCD, and EIS are carried out at specified temperatures and the capacitive performance from GCD measurements is listed in Table 4. The operating voltage at different temperatures is determined by a series of CV measurements with a gradual increase of the voltage window. Accordingly, the highest voltage with less than 10 % accelerated relative standard deviation of anodic current is set as the voltage limit at a specified temperature. Consequently, a maximum voltage of 1.5 V is maintained up to 80 °C followed by 1.4 V up to 120 °C and finally down to 1.3 V at 150 °C. It is worth noting that due to the high viscosity, and low ionic conductivity of the electrolyte at RT, the IR drop is quite large, and therefore the usable voltage becomes lower. When operated at a higher temperature, due to increased ionic conductivity, the IR drop reduces and provides larger usable voltage in addition to increased capacitance. Consequently, both the energy density and the power density at elevated temperature increase compared to RT. EIS measurements in a wide frequency range show a characteristic change in the impedance behavior with elevated temperature. At the highest frequency, the resistance decreases quite significantly supporting an increased ionic

conductivity in the device. However, at the lowest frequency, the impedance behavior severely deviates from the ideal capacitive behavior with increasing temperature indicating that the leakage current and self-discharge rate is drastically increasing with temperature. In **Paper III**, we have conducted a thorough investigation regarding the origin of the self-discharge behavior and quantify the underlying mechanisms.

Cyclic stability test (Fig. 26 a) at specified temperatures demonstrate good stability and coulombic efficiency (Fig. 26 b) throughout the temperature range besides 150 °C indicating an upper-temperature limit of 120 °C for long term use.
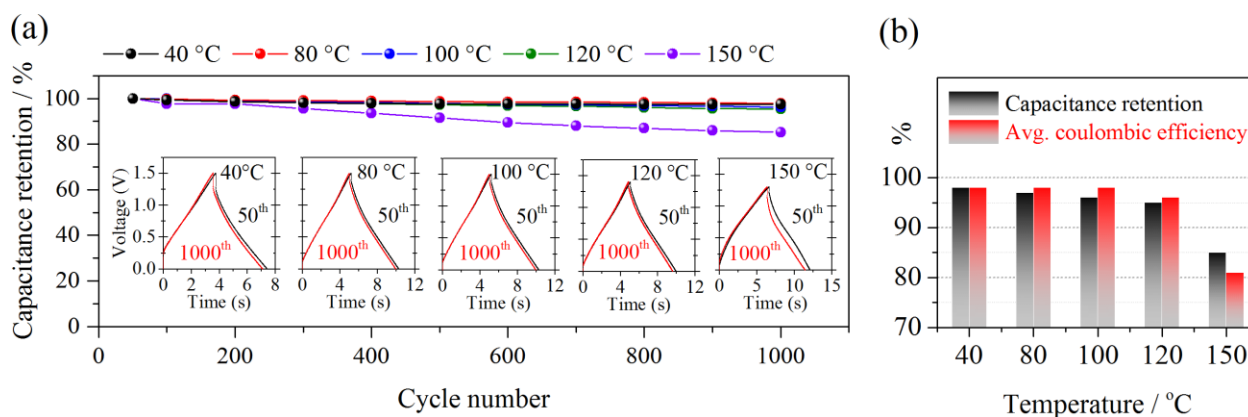

Figure 26: (a) CCD test at 40, 80, 100, 120, and 150 °C for 1000 cycles (b) capacitance retention at 1000th cycle and average coulombic efficiency as a function of temperature (**Paper II**).

A high operating voltage provides high energy density. However, at elevated temperatures, the risk of accelerated aging increases quite drastically. Therefore, lowering the operating voltage range to gain better stability is mutual. Most importantly, in the studied system, there is no sacrifice in power or energy density by lowering the operating voltage. The benefit of gaining better stability without sacrificing energy or power can be applied to other ionic liquid systems as well. It is worth pointing out that the selection of EMIm OAc electrolyte was largely due to a project requirement where the devices needed to be assembled in an uncontrolled environment and, for personnel safety the components (EMIm OAc) [98, 99] needed to be less toxic nature.

4.3 Quantifying self-discharge mechanism at elevated temperature

From a thermodynamic point of view, the fully charged state of an EC is at a higher free energy level compared to the discharged state or partially charged state. If there is a self-discharge mechanism or pathway, the Gibbs free energy spontaneously pushes the system towards lower energy levels [12] as shown in Fig. 27.
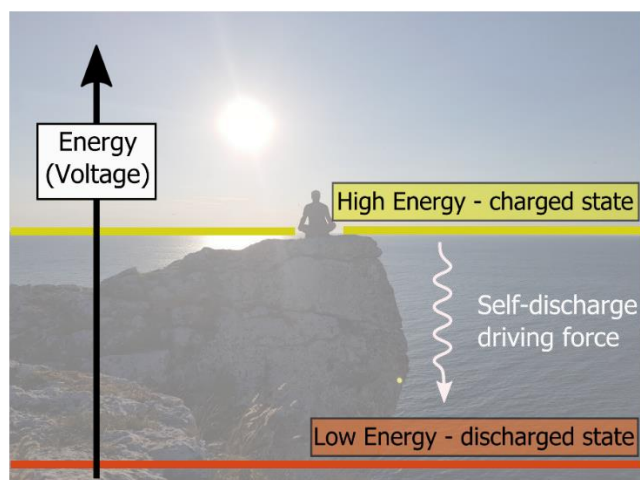
Figure 27: Gibbs energy, a driving force for the self-discharge of EES.

4.3.1 Underlying mechanisms:

This spontaneous energy fading process occurs due to different mechanisms related to different kinds of driving forces that build up during a charging process. Conway *et al.* proposed three kinetic models for determining the self-discharge mechanism [12].

Firstly, self-discharge occurs due to an activation-controlled mechanism that originates from the oxidation and reduction reaction when a high concentration of impurities are attached to the electrodes (surface functional groups), or in electrolytes (transition metal ions) [100], or when a device is charged beyond the operating voltage window (electrolyte decomposition) [101]. The spontaneous decay related to self-discharge continues until the overvoltage reaches zero [12]. In an activation-controlled mechanism, transport limitations are negligible and electron transfer determines the self-discharge rate [11, 12]. The mechanism kinetically follows the Tafel equation and the measured potential (V) is related to the self-discharge time (t) through the following equation [12]:

$$V = V_o - \frac{R_g T}{\alpha F} \ln \frac{\alpha F i_o}{R_g T C} - \frac{R_g T}{\alpha F} \ln \left(t + \frac{CK}{i_0} \right) \qquad \text{Equation 44}$$

where V is the voltage that changes over time, V_o is the initial voltage, R_g is the ideal gas constant, T is the temperature, α is the charge transfer coefficient, F is the Faraday's constant, i_o is the exchange current density, C is the interfacial capacitance, and K is an integration constant. Voltage declines linearly with log t after an initial plateau.

Secondly, the diffusion-controlled mechanism rises due to the presence of a low concentration of depolarizing impurities in the electrode (parasitic species such as adsorbed oxygen) or electrolyte (impurities, transition metal ions) that go through the Faradaic reaction (e.g. shuttle

reaction of Fe^{2+}/Fe^{3+}) within the potential range [74]. In a diffusion-controlled mechanism, the electron transfer is fast and transport of the parasitic species to the electrode determines the rate. The governing self-discharge equation is derived from the Fick's diffusion laws and can be expressed as [12]:

$$V = V_o - C^{-1}2zF \cdot AD^{\frac{1}{2}}\pi^{-\frac{1}{2}}c_o t^{\frac{1}{2}}$$

<div align="right">Equation 45</div>

where z is the charge number of the impurity ions, A is electrode surface area, D is a diffusion coefficient, and c_o is the initial concentration of impurities. Although the Fick's law models the dynamics of the potential decay for a planar electrode, in principle, the model can be applied to porous electrodes as well [11], where the diffusion process initiates due to an excess ionic concentration near the electrode surface [102] and voltage declines linearly with $t^{1/2}$.

Thirdly, the self-discharge can occur when there is an ohmic leakage pathway in the device due to faulty construction, or an undesired conductive pathway between the electrodes because of separator shrinkage, or an incomplete sealing of bipolar electrodes. The voltage decay due to self-discharge depends on the resistance of the ohmic leakage and the capacitance. The governing equation is expressed in terms of RC time constant as follows [12]:

$$V = V_0 e^{-t/RC}$$

<div align="right">Equation 46</div>

where C is the capacitance, R is the leakage resistance. ln (V) decays linearly with t.

Electronic charge redistribution (CR) in the porous carbon electrodes and the ionic CR in the electrolyte is considered to be the main reason for self-discharge in a typical carbon-based EC [13, 103]. As the porous carbon contains different sized pores with diverse distributions, typically the pore mouth responds more quickly to the applied voltage than the pore base (Fig. 28 b). The CR is described by a transmission line model (TLM) with a vertical ladder network (Fig. 28 a), where charging different pores is equivalent to charging different resistor (R_n)/capacitor (C_n) circuits with different RC time constants [13].
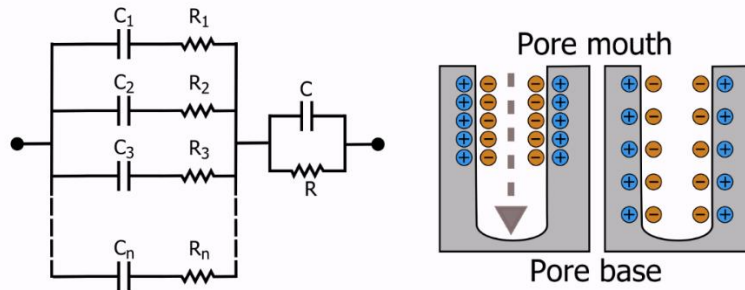

Figure 28: (a) TLM with vertical ladder network, and (b) charge redistribution in pores.

As the charging/discharging process does not proceed evenly in the entire interface, there exists a nonequilibrium charged state. In an open circuit configuration, CR drives the nonequilibrium state towards equilibrium by pushing the charges from a higher to a lower surface charge density. Consequently, an apparent voltage decay is observed when the device is in an open circuit condition. It has been shown that the voltage decay follows the same mathematical expression as the voltage decay due to activation-controlled self-discharge in the form as follows [104]:

$$V = V_0 - a \ln(t + b)$$ Equation 47

where a and b are constants.

4.3.2 Self-discharge profile:

By plotting the observed voltage decay according to their mathematical treatment, self-discharge mechanisms can be identified to some extent. The relationship between potential and time and their representative profile is summarized in Table 5.

Table 5. Self-discharge mechanisms and voltage relationship with time

Self-discharge Mechanism	Source	V vs. t	Graphical profile
Activation-controlled Faradaic process	High concentration of impurities, or overcharging	V vs. $\log t$	Linear drop after plateau
Diffusion-controlled Faradaic process	Low concentration of impurities, or ionic concentration mismatch	V vs. $t^{1/2}$	Linear drop
Ohmic leakage	Fault in construction	$\ln (V)$ vs. t	Linear drop
Charge redistribution	Different RC time constant	V vs. $\log t$	Linear drop after plateau

Experimental results can be fitted by taking into account all the different mathematical treatments related to self-discharge and therefore, can be identified and quantified the contribution of individual mechanisms.

Although ECs containing ILs are suitable for high-temperature application and perform even better than at RT they suffer adversely from undesired accelerated self-discharge and leakage current. In **Paper III**, we have carried out a systematic investigation of temperature influence on the self-discharge behavior of 4 devices (D_1, D_2, D_3, and D_4) containing EMIm OAc IL from RT to 60 °C with maximum operating voltage ranging from 1 to 1.5V.

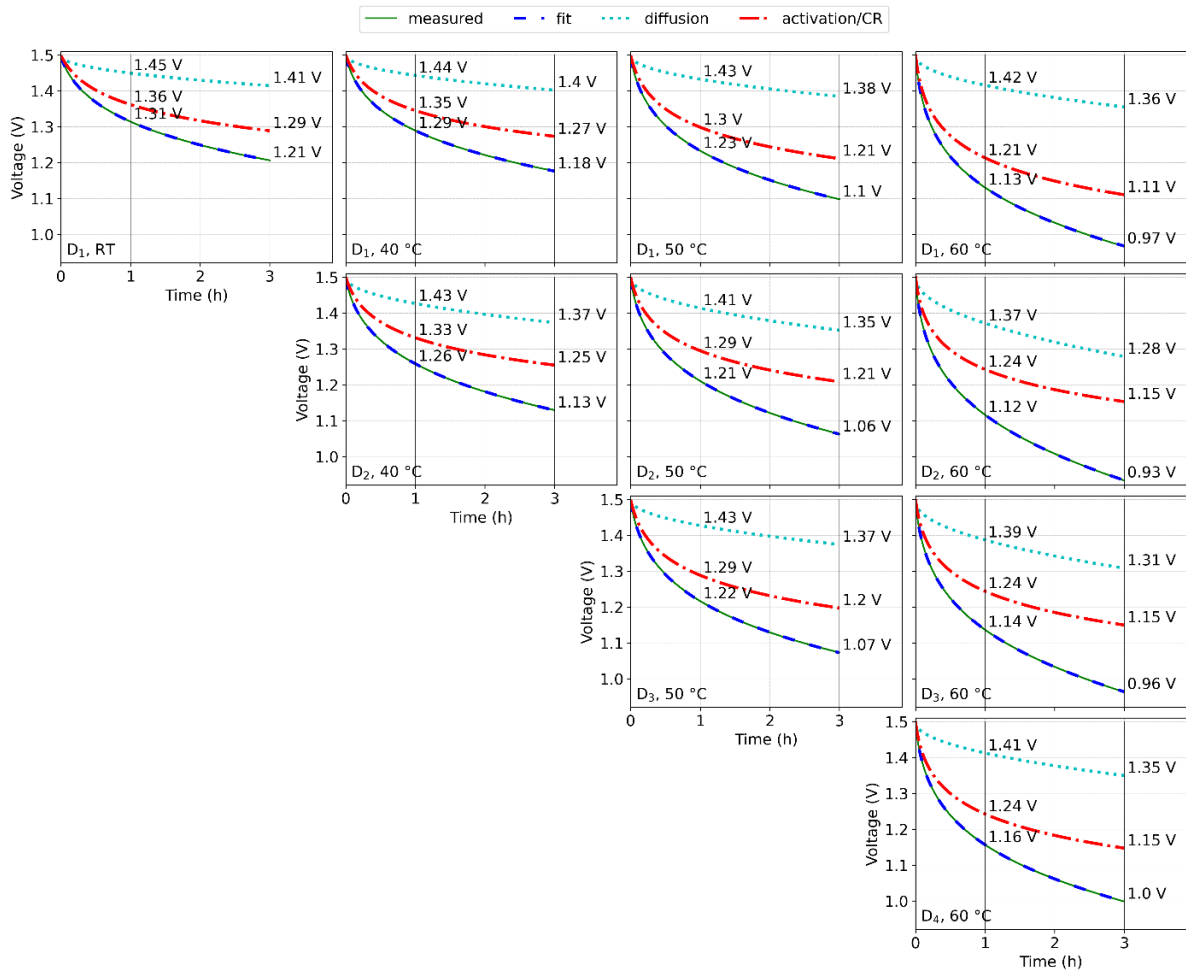### 4.3.3 Instantaneous temperature influence:

Figure 29: Self-discharge profiles of D1, D2, D3, and D4 at different temperatures with experimental and fitted data (**Paper III**).

Systematic temperature exposure on four devices (Fig. 29) shows that the self-discharge rate increases linearly with temperature. The measured data are plotted and fitted with the governing equations related to the self-discharge mechanisms. The self-discharge due to ohmic leakage is discarded because the plot of ln V vs t does not exhibit any linear drop. Considering that the contribution from ohmic leakage occurs due to an undesired conducting pathway between the electrodes, the obtained non-linear drop in voltage suggests that there is no fault in the construction of the device.

Regardless, the voltage loss at 1.5 V for all four devices in the whole temperature range is accurately described with a combination of activation/CR- and diffusion-controlled mechanisms. The loss ratio calculated from diffusion- over activation/CR-controlled mechanism lies between 0.4-0.6 for all the devices at each temperature, even though they have a different operating

history. The similar voltage loss ratio at a particular temperature suggests that the instant temperature strongly dictates the extent of voltage loss (higher loss at a higher temperature) rather than the previous history.
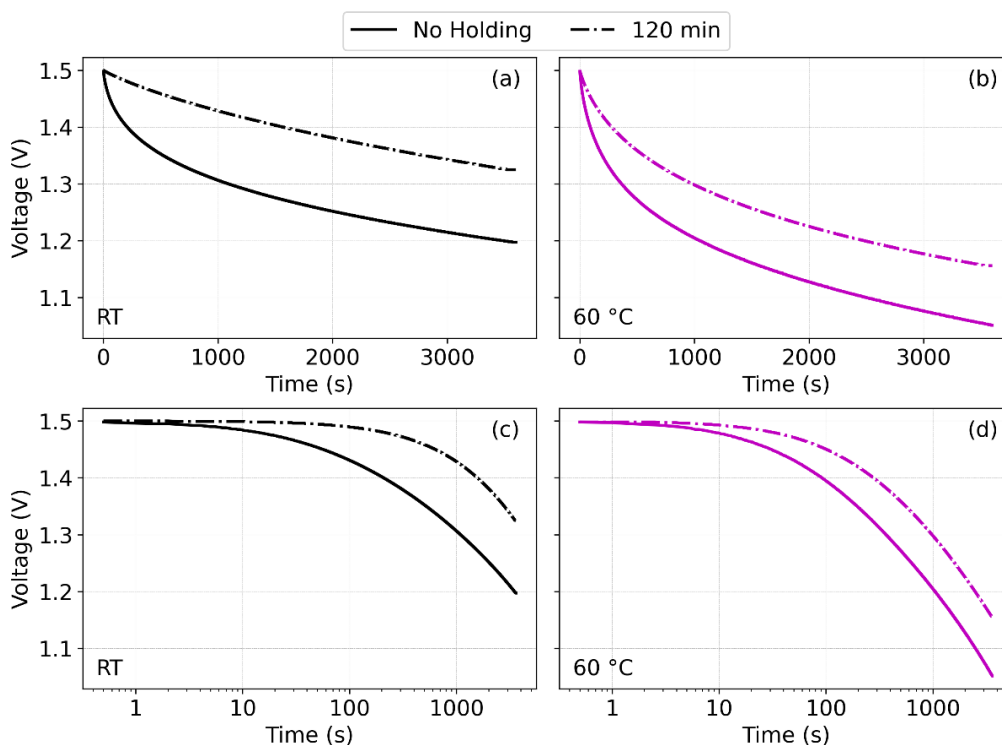
4.3.4 Identification of underlying mechanisms:

Figure 30:Self-discharge after different holding times: (a, b) voltage decay with time (t), and (c, d) voltage decay as a function of time (t) in logarithmic scale (**Paper III**).

Recalling from Table 5 that the voltage decay profile due to CR is very similar to the voltage decay caused by activation-controlled mechanism and so are the governing mathematical expressions. Therefore, besides the diffusion-controlled mechanism, Fig. 29 does not reveal whether activation- or CR-controlled mechanism, dictates the self-discharge. One way to separate the underlying mechanism is to add a potential hold at the end of a charging ramp or charge at a lower rate which then influences the voltage decay related to CR but not on the activation-controlled mechanism [11]. Consequently, the voltage decay of D_4 at RT and 60 °C with 120 minutes of holding and without any holding step after the initial charging to 1.5 V exhibits a noticeable change in the plateau length and slope of the voltage decay (Fig. 30).

This demonstrates that the self-discharge at 1.5V is driven by the CR-controlled mechanism in addition to the diffusion-controlled mechanism. Inherently, CR occurs due to incomplete charging of the different RC subsystems in the porous carbon electrodes that result in a

distributed potential and equilibrates during self-discharge. Therefore, with a longer holding time or with a slow charging rate, more RC subsystems (related to more of the bulk material) get charged, and the voltage loss suffers less from the CR effect. Accordingly, the slopes of the linear voltage decay also decrease, and a higher voltage is retained with the subsequent holding step.

4.3.5 Quantification of underlying mechanism:

Voltage decay due to the CR-controlled mechanism is also influenced by the initial polarizing voltage [11]. In order to isolate and quantify the CR and diffusion contribution at different nominal voltages, D_4 was subjected to different initial polarization voltages ranging from 1 to 1.5 V at both RT and 60 °C, and the results are shown in Fig. 31 (a, b).
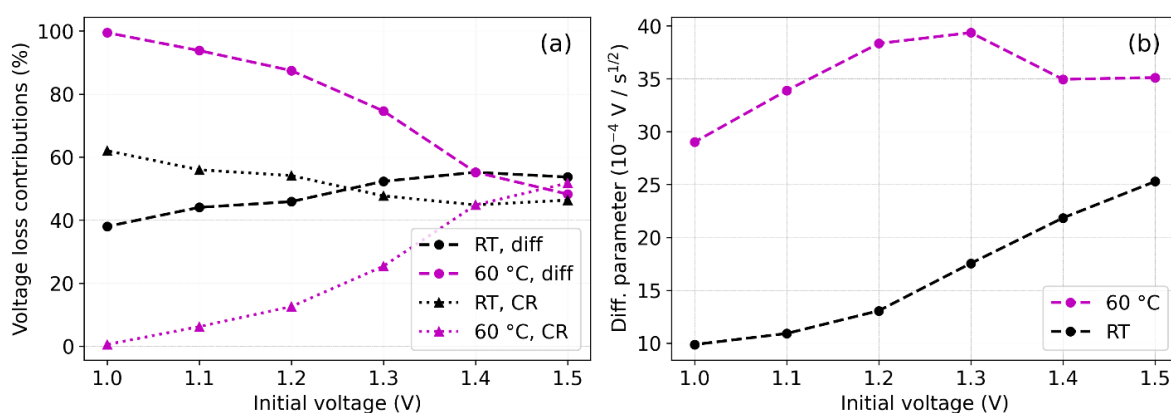

Figure 31: (a) Voltage loss contribution from CR and diffusion mechanisms, and (b) diffusion parameter at different initial voltages at RT and 60 °C (**Paper III**).

Both the mechanisms are occurring at different initial voltages, the device at RT has a similar contribution from diffusion and CR, although until 1.2 V voltage the loss due to CR is slightly higher than that from the diffusion. However, a distinctive competing mechanism can be noticed at 60 °C. At lower initial voltages until 1.3 V, diffusion dominates over CR and gradually becomes quite similar at 1.5V. Generally, CR in porous electrodes is dictated by the finite conductance of electrolytes and is a limiting factor for the migration of the ions in the micro and mesopores located in the deeper part of the surface. With high temperature, the increased ionic conductivity of the electrolyte ensures a more complete charging among different pores, and the contribution of CR to the voltage decay is much less. At a higher initial voltage, the magnitude of thermal agitation of the electrolyte is more pronounced and creates an unbalanced ionic distribution resulting in more unstable double layers that promote CR, as can be seen, at 1.5V. In Fig. 31 (b), the dominance of the diffusion mechanism can be seen at all initial voltages at the higher temperature.

Measured leakage current also increases with elevated temperature and follows an Arrhenius relation.

$$I_L = A \exp(-\frac{E_a}{RT})$$ <div align="right">Equation 48</div>

where I_L is the leakage current, E_a is the activation energy, R is the gas constant, and T is the temperature.

The activation energy calculated from the Arrhenius plot is 21±1 kJ mol^{-1}, which is very close to the activation energy related to diffusion-controlled processes (16-20 kJ mol^{-1}). Whereas a 40-80 kJ mol^{-1} is representative of an activation-controlled process. Therefore, In this regard, the activation energy associated with this device strongly indicates that the self-discharge mechanism is driven by a diffusion-controlled mechanism in addition to the CR effect.

4.4 Suppressing self-discharge with liquid crystal additive

4.4.1 Approach to reducing self-discharge:

As the driving force of self-discharge and leakage current is a thermodynamic process, complete mitigation is not entirely possible. However, by suitable modification of the components of the device such as electrodes, electrolytes, separators, and current collectors the driving force for the self-discharge rate can be slowed down kinetically to some extent. For instance, an ultra-thin insulating layer of poly (p-phenylene oxide) (PPO) was electrodeposited on activated carbon electrodes which could lower parasitic Faradaic reaction in the device and in turn reduce leakage current by 78%. However, the specific capacitance was also decreased by 56% [105]. A modification of a cellulose separator with polyethyleneimine (PEI) with positive surface charges could reduce the diffusion of ions in the device and suppress the self-discharge rate, however, the rate capability reduced with PEI inclusion [106]. By using copper foil as a positive electrode current collector and zinc foil as a negative electrode current collector a galvanic effect was introduced in the cell where the micro-current from the collectors can compensate the self-discharge current. However, the device life was only limited to 2000 cycles [107]. The addition of surfactants such as Triton X-100 (p-t-octylophenol), SDS (dodecyl) in aqueous electrolyte could reduce self-discharge where the long alkyl chain in the surfactants function as a microinsulator and hiders the leakage current [108]. Liquid crystals were also used as an additive to an organic electrolyte-containing device that could suppress self-discharge by taking advantage of the electrorheological effect of the liquid crystals [109]. Among the different strategies, electrolyte modification seems a quite promising solution to suppress the self-discharge rate without significant sacrifice on the capacitive performance. In **Paper IV**, we have carried out a thorough electrochemical investigation of an EC containing a mixture of a small amount of thermotropic

nematic liquid crystal, 4-n-pentyl-4'-cyanobiphenyl (5CB), in 1 M Li₂SO₄ electrolyte to suppress the self-discharge behavior.

4.4.2 Liquid crystals:

Liquid crystals (LCs) are intermediate between a crystal and an isotropic liquid, which has thermodynamically stable phases defined by their long-range orientational order and various degrees of positional order of the building blocks (mesogens). LCs combine the fluidity of liquids and the anisotropy (optical, mechanical, electrical, and magnetic) typical of crystals. The simplest LC phase (nematic) is a 3-dimensional anisotropic liquid characterized by a long-range orientational order [110]. In the nematic phase, the ensemble of the molecules takes an ordered arrangement with their long axes pointing toward a particular direction defined by the director **n**, which is the local average direction of the molecule axes (Fig. 32). The orientational order parameter is expressed as $S = 1/2 < 3\cos^2\beta -1 >$, where β is the angle between an individual molecular long axis and **n**, and the brackets represent the statistical average. The value of S for a typical nematic LC lies in the range between 0.3 and 0.8, while S would equal 1 for perfect orientational order and 0 in the isotropic phase. With increasing temperature, the S value goes discontinuously to zero at the thermally induced nematic to an isotropic phase transition [110].
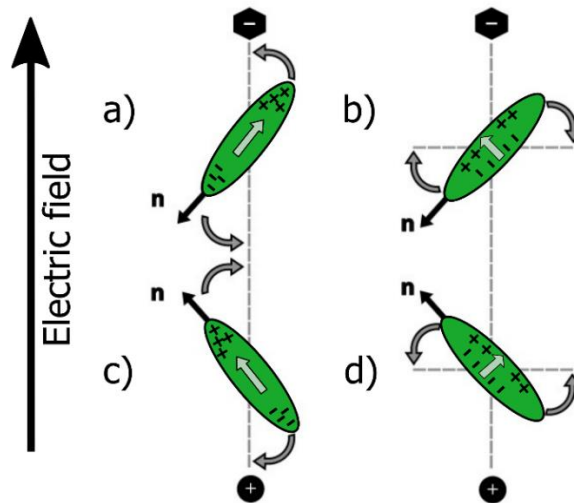
Figure 32: Reorientation of LC director with electric field: (a, c) LC with positive dielectric anisotropy, and (b, d) LC with negative dielectric anisotropy.

The dielectric anisotropy is determined by the following equation [111],

$$\Delta\varepsilon = \varepsilon_{||} - \varepsilon_{\perp} \neq 0 \qquad\qquad \text{Equation 49}$$

where $\varepsilon_{||}$ and $\varepsilon_{\perp}$ are the dielectric permittivities measured along and normal to the director, respectively.

If the dipole moment is parallel to the long molecular axis then the parallel part of the dielectric constant is the largest, thus $\Delta\varepsilon > 0$ (positive dielectric anisotropy). However, if the molecules carry dipole moments that are more or less normal to the long molecular axis then the perpendicular part of the dielectric constant is the largest and $\Delta\varepsilon < 0$ (negative dielectric anisotropy).

With an applied electric field, LC molecules respond collectively and cause the distortions of the director **n**. LC with positive dielectric anisotropy responds to the electric field predominantly parallel to the **n** director (Fig. 32(a and b)), while the LC with negative dielectric anisotropy responds perpendicular to the electric field (Fig. 32(c and d)). The larger the dielectric anisotropy the smaller the electric field is needed to reorient the LC molecules.

The material 5CB is a well-known, well-studied commercial thermotropic LC with robust electrochemical stability. It is composed of two phenyl aromatic rings terminated by a CN (cyanonitrile) head group at one end and a 5 membered alkyl chain (pentyl) at the other end with a positive dielectric anisotropy ($\Delta\varepsilon = +13$). It is part of the nCB family (n is the number of members in the alkyl chain). Generally, the alkyl chain determines the melting point, introduces flexibility, and controls the stability of the LC phases [112]. The nematic phase of 5CB exists below the nematic to the isotropic phase transition temperature, which is at 308.5 K (35 °C) [112]. The molecular structure of 5CB is shown in Fig. 33.

4.4.3 Role of liquid crystal in suppressed self-discharge:

Fig. 33 shows a simplified version of the mechanism on the negative side of the device during the discharged state, and the charged state without the solvent molecule (water), and hydrated ions.
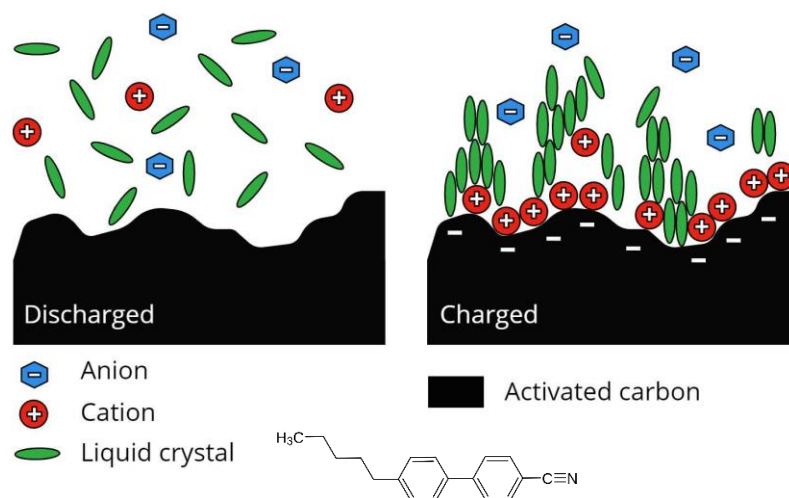

Figure 33: Schematic representation of 5CB alignment in the charged state and discharged state.

In a fully charged EC, the population of unhydrated electrolyte free ions is expected to be more in the compact layer part of the interface leaving the LC molecules to reside in the diffuse layer where they could possibly be localized forming a thin film along with the interface. In the open-circuit configuration, when the ions from the interface tend to diffuse out to the bulk in order to reach its equilibrium of disorder (diffusion) this thin film act as a "blocking layer" (Fig. 33) that is unfavorable for the cross-diffusion of the active electrolyte ions, which eventually suppresses the rate of self-discharge. The blocking layer could also form as a consequence of the reorientation of LC molecules. In a fully charged state, the electric field strength within the EDL could reach up to 10^7 V/mm decreasing exponentially from the compact layer to the bulk solution [113]. The electric field originating from the double layer may align the local director of the 5CB parallel to the electric field (due to positive dielectric anisotropy of 5CB) and create the "blocking layer" that suppresses the self-discharge. In the discharged state, there is no electric field that could facilitate the orientational polarization and thus the LC molecules are more or less randomly distributed throughout the electrolyte.

Fig. 34 shows the self-discharge behavior of the EC at different initial voltages. Devices with 5CB show a slower self-discharge rate compared to the device without 5CB in the entire voltage range. Capacitance is similar for both the devices **(Paper IV)**.
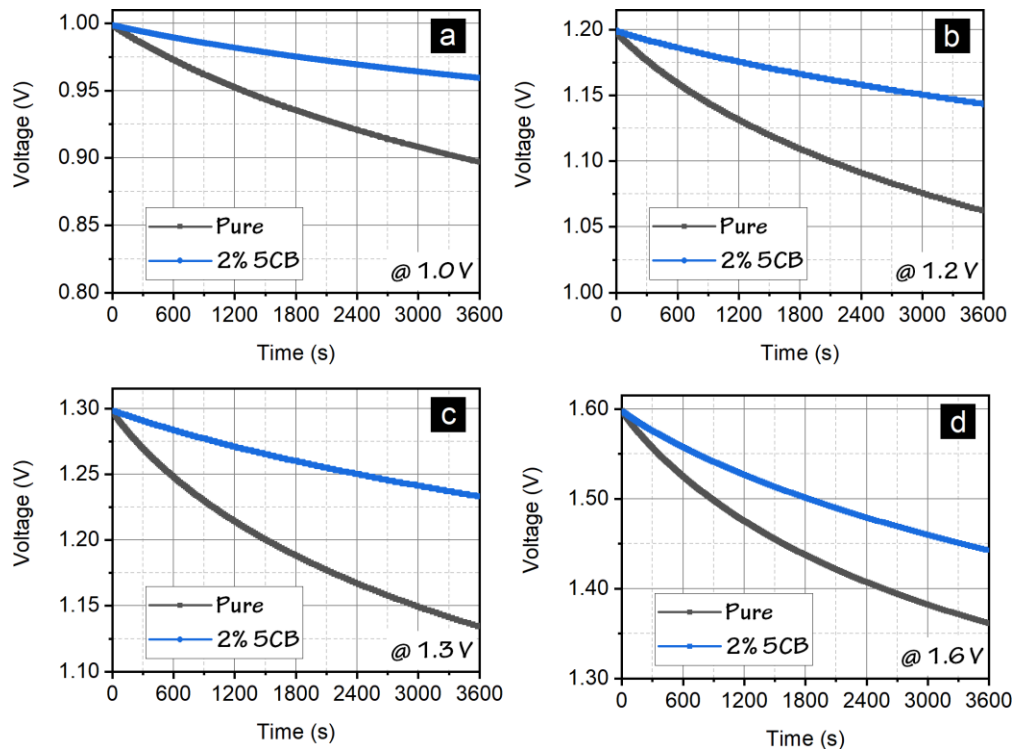

Figure 34: self-discharge of ECs from different initial voltage (a) 1 V (b) 1.2 V (c) 1.3 V (d) 1.6 V (**Paper IV**).

The influence of the LC in the charged state is verified with the EIS analysis, Nyquist plot (Fig. 35). It can be noticed that at the charged state of the EC with 5CB, the interfacial resistance increases almost two orders of magnitude compared to the EC without 5CB, confirming an increased solution resistance as a consequence of the localization or realignment of the LC molecules in the vicinity of the interface. The reduction of the self-discharge in this system is in line with the observation reported by Xia *et al.* [109], where the role of LC in self-discharge reduction is related to electrorheological effect (increased viscosity in the vicinity of the interface due to reorientation of LC molecules).
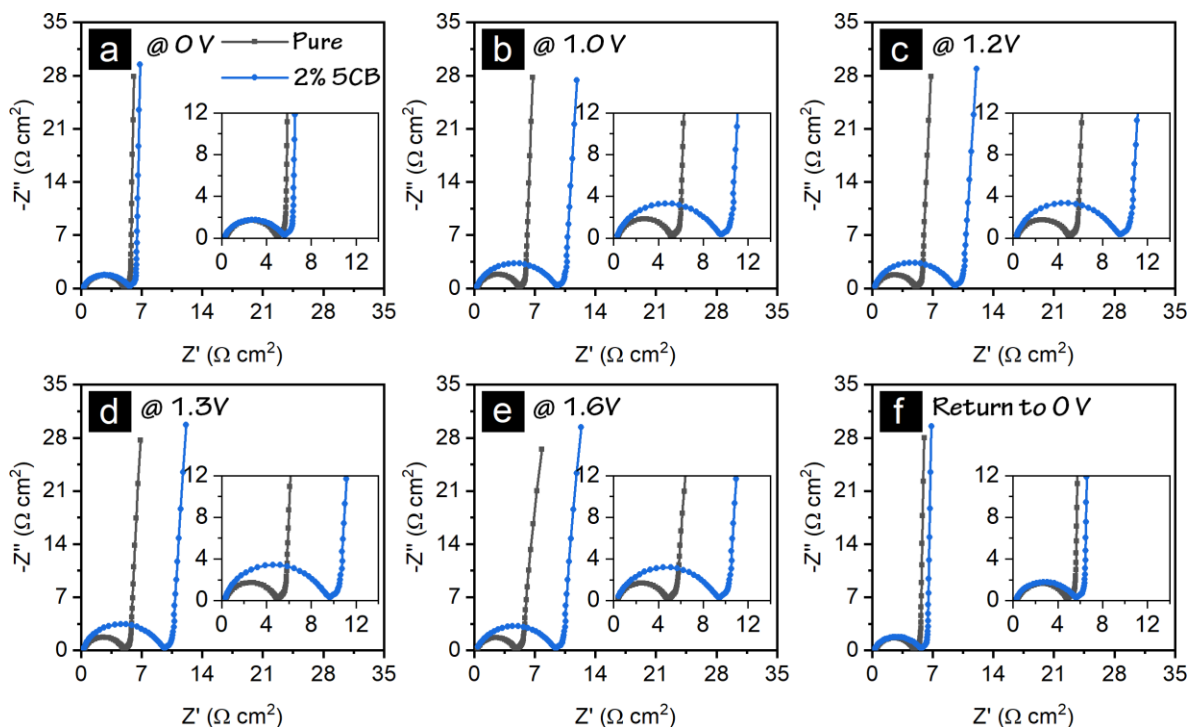
Figure 35: EIS at different DC voltage (a) 0 V (b) 1 V (c) 1.2 V (d) 1.3 V (e) 1.6 V and (f) return to 0 V (**Paper IV**).

However, it is still not clear from a physics point of view how the reorientation of the LC actually decreases the ionic conductivity. Normally, the ionic conductivity in a nematic LC is larger along with the director than perpendicular to it [112, 114], which seems to contradict the picture that field-induced reorientation of the director into the field direction should decrease the conductivity.

It should also be pointed out that the porous carbon electrodes are not flat. Instead, they have diverse pores, valleys, and hills with characteristic dimensions from nanometers up to several micrometers. Hence, close to the electrodes, the LC director field is probably significantly non-uniform and might even contain topological defects. It is not clear whether these topological

defects and their response to electric fields could have an impact on the field-controlled effective conductivity. Further investigation is required to fully understand the microscopic scenario.

4.5 Utilizing low-grade waste heat to recover charge from an EC

4.5.1 Low-grade waste heat:

A vast amount of thermal energy is ubiquitously available generated as a byproduct of various industrial processes and from non-industrial sources such as power plants, heat pumps, heat exchangers, dryers, big data centers, automobile engines, domestic cooling and refrigeration processes, and not to mention in a variety of temperature gradients produced by the sun. A huge portion (63 %) of this thermal energy stays in the surroundings below 100 °C which is known as low-grade waste heat [115]. Recovery of this waste heat constitutes attractive energy resources to power electronics.

4.5.2 Typical thermoelectric devices:

There are commonly three methods to convert heat into electricity. Firstly, mechanical heat engines [116], which utilize the thermal energy of a fluid that is transported between a heat source of high temperature to a heat sink of low temperature. Initially, thermal energy transforms into mechanical work that is successively utilized to drive an electric generator. Although they work with high-energy conversion efficiency, their moving mechanical parts make them impractical to apply to a distributed heat source [116].

Secondly, the more straightforward converter is known as thermoelectric engines or thermoelectric generators that avoid the intermediate mechanical step and convert heat directly into electrical current [117]. The conventional thermoelectric generators, based on thermoelectric materials that are typically composed of semiconductors [118], half-metal alloys [119], or conducting polymers [120]. The working principle is based on the well-known Seebeck effect, which is a generation of electrical potential difference due to a temperature gradient along with the thermoelectric materials. Generally, they work well at higher temperatures (> 350 °C) and exhibit poor efficiency when it comes to capturing low-grade thermal energy [117, 121]. This is particularly due to difficulties to maintain a fixed temperature gradient because of a large amount of heat conduction from the thermal shortening effect [122].

Thirdly, the ionic thermoelectric system, which is receiving increased attention owing to its capability of producing a large output voltage from a small temperature gradient [123]. Unlike conventional solid-state thermoelectric generators where the transport of charge carriers (electrons or holes) are bound by the band structures, an ionic thermoelectric system holds the freedom of harvesting different forms of entropy carried by ions. Typically, an ionic thermoelectric system exploits either the thermogalvanic effect or the ionic thermodiffusion

effect, also known as the Soret effect, or synergies of both [124]. The thermally induced voltage from the thermogalvanic effect originates from the temperature-dependent thermodynamic shift in the chemical potential of the redox couple present in the cell. On the other hand, the voltage output from the ionic thermodiffusion effect rises due to temperature-dependent kinetics of the electrolyte solution such as the relative motion of the cations and anions. Different concentrations of ions accumulate in the hot and cold boundaries creating a macroscopic electric field that manifests as a potential difference in an electrochemical cell [124, 125].

4.5.3 Performance metric of thermoelectric devices:

Although all the above-mentioned thermoelectric systems evaluate the same thing, which is a certain amount of voltage output in a given temperature gradient, the operation mode is slightly different due to their different working mechanisms [126] listed in Table 6.

Table 6: Working mechanism and performance metric of the different thermoelectric systems

Thermoelectric systems	Device	Underlying Physics	Expression	Mechanism
Solid-state thermoelectric generator	Thermoelectrics	Seebeck effect	$S_e = \left\vert \dfrac{\Delta V}{\Delta T} \right\vert$	Diffusion of electrons or holes
Ionic-thermoelectric system	Thermocell	Thermogalvanic effect	$\alpha = \dfrac{V_h - V_l}{T_h - T_l} = \left\vert \dfrac{\Delta S_{h,l}}{nF} \right\vert$	Temperature-dependent redox reaction
Ionic-thermoelectric system	Thermoionic capacitor	Soret effect	$S_i = \left\vert \dfrac{\Delta V}{\Delta T} \right\vert$	Diffusion of ions

where S_e is electronic Seebeck coefficient, α is the temperature coefficient, S_i is the ionic Seebeck co-efficient or Soret coefficient, ΔV is the voltage output, ΔT is the given temperature gradient, V_h is the voltage at high temperature (T_h), V_l is the voltage at low temperature (T_l), $\Delta S_{h,l}$ is the reaction entropy for the redox species, n is the number of electrons participating in the reaction, and F is Faraday's constant. The sign convention of Seebeck coefficient or temperature coefficient is either positive or negative based on the direction of the charge carriers.

The temperature coefficient of a thermocell can be thought of as the electrochemical version of the electronic Seebeck effect. A typical thermoelectric module, made of metal/semiconductor/metal stack, generates a constant and continuous electrical output that can be delivered to an external load, and during the process, there is no net transfer of material involved. On the other hand, a net transfer of redox-active species occurs between the hot and

cold electrodes in the case of a thermocell with a negative temperature coefficient. Mass balance is satisfied with ionic diffusion of oxidized species from the hot to the cold electrode and reduced species from the cold to the hot electrode. The opposite applies to the thermocell with a positive temperature coefficient. Therefore, the voltage rise in a thermogalvanic cell occurs due to a combination of the thermodynamic shift in the chemical potential of redox species and thermodiffusion of ionic species driven by the temperature gradient [124]. This working principle allows the thermocell to operate in a continuous mode like thermoelectrics and, the power density becomes the most relevant performance metric [123, 127]. In a thermoionic capacitor considering zero redox activity, the thermodiffusive ions are the sole charge carriers and they can not pass through the external circuit. Rather, the ions accumulate at the electrodes and form an electric double layer (thermocapacitive effect [128]), inducing a transient current that decreases over time [123]. Therefore, the operation mode is not continuous but intermittent and both the energy density and power density are the relevant performance metric [127].

4.5.4 Potential of EC as thermoionic system:

Utilizing a fixed temperature gradient between the two interfaces is the most typical approach for a thermoionic system, which requires the electrodes to be quite far from each other to maintain that temperature gradient. The large distance between the electrodes unfavorably affects the power performance [129]. However, if the two interfaces hold dissimilar interfacial properties then the fixed temperature gradient is not essential, instead, a homogenously varying temperature can create a mismatch in the thermal responses of the interfaces resulting in a voltage output with the thermocapacitive effect [129, 130]. Thermoionic system working in a homogenously changing temperature offers a significant advantage from a design perspective as maintaining a fixed temperature gradient is very difficult in a low-grade waste heat regime [126]. Moreover, as there is no need to maintain the fixed temperature gradient, the distance between the electrodes could be minimized, and essentially the structure of the device would be similar to an electrochemical capacitor [131].

Carbon with its high surface area is recognized to be the material of choice for many commercial ECs due to its ability to facilitate both types of charge storage mechanisms thanks to its' versatile forms and the range of attachable functional groups [132, 133]. Porous carbon electrodes soaked in electrolyte produce a spontaneous net interface potential without any electrical bias. The potential difference in the double layers rises due to different ion-ion, ion-solvent, and ion-surface functional group interactions [134, 135]. These interactions in the interfacial double layer are strongly influenced by temperature [136, 137], and an increased potential difference can be achieved with increasing temperature. Besides, ionic and electronic charge redistribution effects in the interface containing the porous carbon electrodes are unavoidable due to the difference in kinetics between the fast movement of free electrons and the slower movement of

counterions. As a result, a significant portion of the charge stays unused in a typical electrical charging/discharging cycle. At the end of discharge, this unused charge, also known as the "*voltage rebound*" effect slowly rises and increases the open-circuit voltage [138]. By applying heat to the device the movement of counterions can be accelerated and the unused charge can be recovered to a larger extent and at a faster pace.

In **Paper V**, we have demonstrated the potential of utilizing low-grade waste to charge ECs and also to recover the unused charge in a typical electrical charge/discharge operation, in a homogeneously increasing temperature from RT to 60 °C. The investigated ECs consist of activated carbon electrodes and two different IL electrolytes namely: 1-Ethyl-3-methylimidazolium bis (trifluoromethylsulfonyl) imide, EMIm TFSI, and 1-Ethyl-3-methylimidazolium acetate, EMIm OAc. In addition to the high thermal and electrochemical stability of ILs, the absence of solvents make them particularly suitable to study the different ionic interactions that result in asymmetry in the electrical double layers responsible for voltage output in ionic thermoelectric system [10, 139].
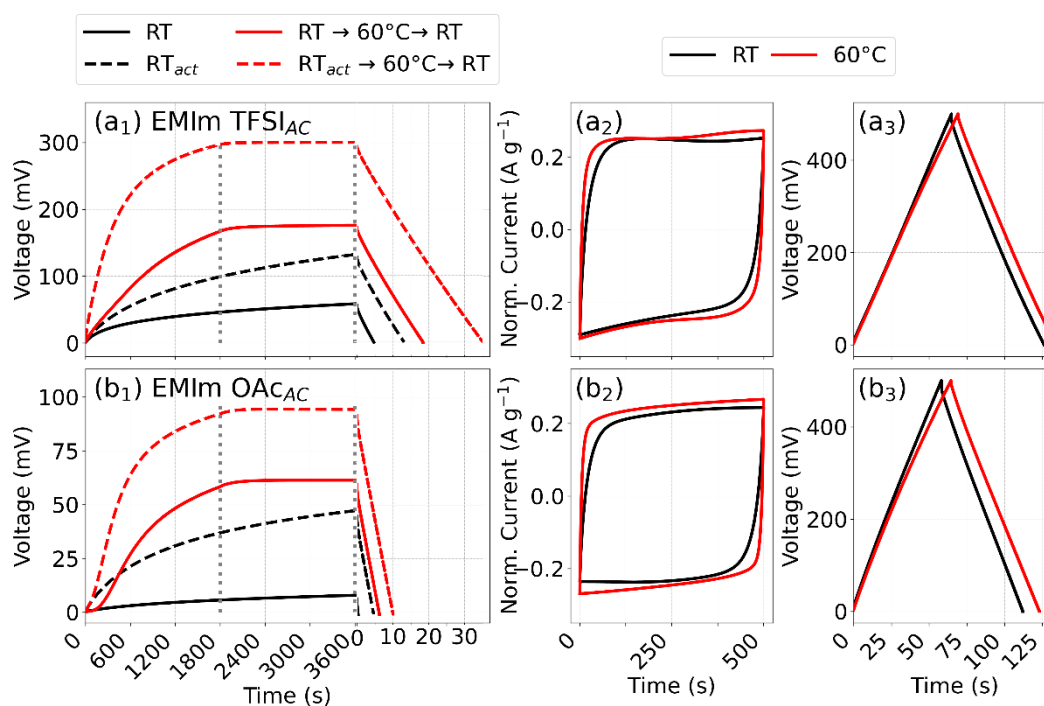
Figure 36: Thermal and electrical characterization of ECs containing AC electrodes and IL electrolytes: voltage output (a$_1$) EMIm TFSI, (b$_1$) EMIm OAc with different conditionings, CV (a$_2$) EMIm TFSI, (b$_2$) EMIm OAc with a scan rate of 20 mV s^{-1}, GCD (a$_3$) EMIm TFSI, (b3) EMIm OAc with a constant of current of 10 mA g^{-1} (**Paper V**).

Fig. 36 (a$_1$, b$_1$) shows the voltage rise of the devices for 1800 s when exposed to heat with different conditionings such as (i) spontaneous voltage rise at RT, (ii) voltage rise after one

electrical charge/discharge (1.5 V) cycle at RT (termed RT$_{act}$-cycle), (iii) voltage rise at the high-temperature environment, and (iv) voltage rise at high-temperature environment after one RT$_{act}$-cycle. The achieved voltages from the heat exposures retain even if the devices are taken out from the high-temperature environment, which gives the opportunity to utilize the harvested energy also at RT. Although the electrochemical signature of both the devices is very similar (Fig. 36 a$_2$, b$_2$, and a$_3$, b$_3$) at RT and 60 °C, the voltage output from the heat exposure is significantly higher for the EMIm TFSI containing devices in all conditionings compared to EMIm OAc containing devices.

Further investigation reveals that the observed difference originates from the dissimilar diffusivity of the ions in the two ILs as can be seen in Fig. 37 which demonstrates the calculated self-diffusion coefficients for all the ions in the whole temperature range.
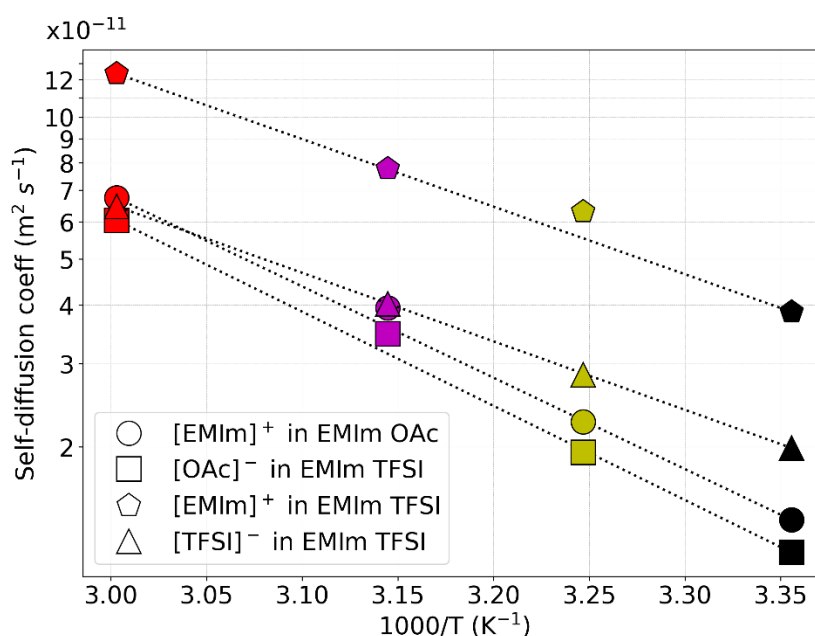

Figure 37: Arrhenius plot of self-diffusion coefficients of individual ions in the studied temperature range (**Paper V**).

It turns out that even if both the ILs share different anions [OAc]$^-$ and [TFSI]$^-$, the observed difference is originating from the self-diffusion coefficients of cation [EMIM]$^+$ (volume of 69 Å^3 [140]) depending on the surrounding anions. The mobility of ions in IL largely depend on the coulombic interaction between the ions. Therefore, the [OAc]$^-$ anion with a small volume of 39 Å^3 [140] has a much higher charge density than the big [TFSI]$^-$ anion with a volume of 100 Å^3 [140]. Consequently, the coulombic interactions between [EMIM]$^+$ and [OAc]$^-$ are much stronger which results in a strong ion pairing. Therefore, the diffusivity of these ions in EMIm OAc is very similar. In contrast, [TFSI]$^-$ anion with a large size moves more independently as single ionic

species as there is weak coulombic interactions between the ions. Consequently, there is a large difference in the self-diffusion coefficients of [TFSI]$^-$ and [EMIm]$^+$ in EMIm TFSI electrolyte. It should be pointed out that the self-diffusion coefficient of [EMIm]$^+$ is significantly higher than that of [TFSI]$^-$ demonstrating the relevance of the ion sizes in the ionic mobility when the coulombic interaction is weak. Several studies [141, 142] reported this phenomenon with different anions including the ions studied in this work.

A large mismatch between the self-diffusion coefficients of individual ions results in a notable voltage output in EMIm TFSI containing devices. In order to demonstrate the feasibility of recovering even larger voltage output, two EMIm TFSI containing devices with AC electrodes, D_1, D_2, and (D_1+D_2) stacked device in series, are exposed to 60 °C after one RT_{act} cycle at 2.5V (single device) and 5 V (stacked device) and the voltage output is recorded as shown in Fig. 38 (a).
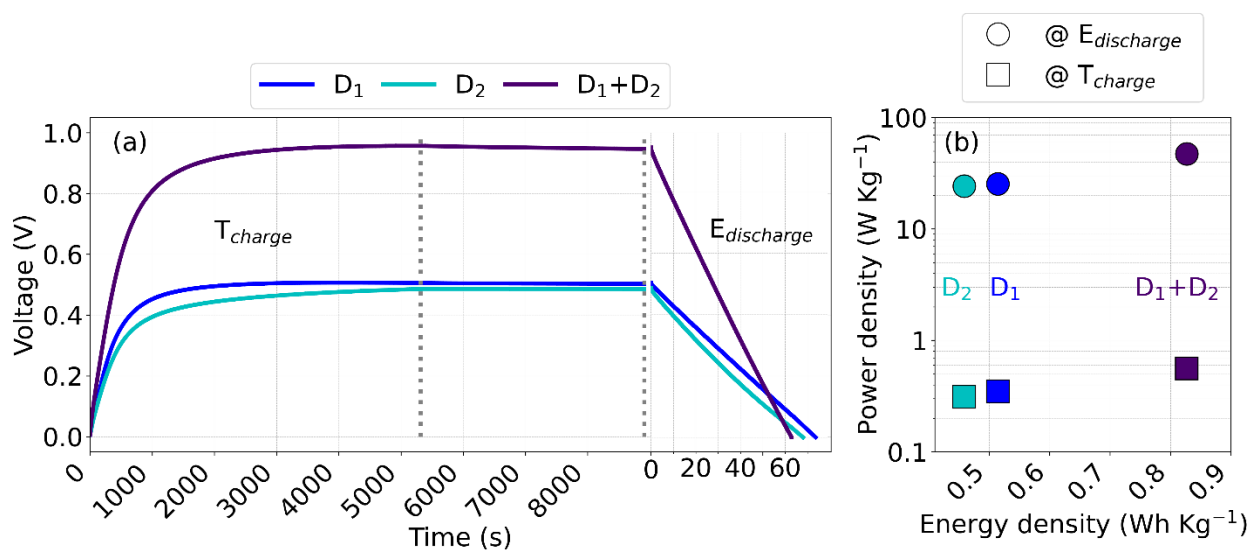
Figure 38: (a) Voltage output of devices, D_1, D_2, and in series D_1+D_2, containing EMIm TFSI electrolyte and AC electrodes, (b) Ragone plot comparing energy density and power density from both thermal charging and electrical discharging (**Paper V**).

A high voltage output of 502, 486, and 943 mV is achieved for D_1, D_2, and, D_1+D_2, respectively. Afterward, the devices are electrically discharged with a constant current of 10 mA g^{-1} at RT and the extracted energy density is calculated to be 0.51, 0.46, and 0.83 W h kg^{-1}, which is plotted in the Ragone plot along with power density, Fig. 38 (b). Increased energy and power density of the stacked device point out the possibility of connecting more devices in series or parallel depending on the application requirements.

Conclusions and future work

5.1 Conclusions

Over the decades, numerous research efforts have focused on the development of EC technology regarding advanced electrode materials, novel electrolytes, and ingenious device architectures; ultimately, with the goal of achieving performance metrics such as high energy and power density, long cycle life, low self-discharge rate, low leakage current, operation in a wide temperature range, cost-efficiency, easy fabrication, and encapsulation. However, it is almost impossible to achieve all these goals from one device as the working principle of these metrics to achieve maximum performance contradict each other. For instance, the achievement of high power density is essentially based on a compromise of the energy density. Therefore, trade-offs are inevitable and largely depend on the application requirements.

This work has focused on the investigation of the diverse phenomena at the interface of carbon-based ECs with different electrolytes and addresses several strategies to improve the most critical performance metrics with minimal sacrifice of others. Notable conclusions are the followings:

Typical aqueous acidic and basic electrolytes can deliver very high capacitance due to their high ionic conductivity, but they suffer from a small voltage window limited by the thermodynamic water decomposition limit. By utilizing an overpotential, the neutral aqueous electrolyte can extend the operating voltage window, but the capacitive performance goes down due to the absence of acidity or basicity. In this regard, a neutral redox-active electrolyte like KBr is promising for boosting the energy density of an aqueous-based system while keeping a high power density. KBr, being a neutral electrolyte, keeps the extended voltage window, and at the same time can deliver improved capacitance originating from the Br^- / Br_3^- redox species at a high redox potential. A symmetric EC can function at a high voltage of 1.9 V where the device operates as an EDLC until 1.6 V and beyond this voltage limit turns into a redox-EDLC. More importantly, redox activity gained from pre-cycling the device at 1.9 V ("triggering effect") can be utilized at a lower potential of 1.6 V with a 22% increase of energy density with a marginal compromise in rate capability compared to the device without pre-cycling at 1.9 V. The history-dependent "triggering effect" is accompanied by the variation of the potential limit of the positive and negative electrode and the *PZV*, which is explained in terms of the complex redox chemistry as well as transport and storage of redox ions. The observations are not limited to only

KBr but also apply to other redox-EDLC as well. Therefore, a careful evaluation regarding the storage mechanism is essential before practical application.

Due to the solvent decomposition, and severe safety concerns aqueous and organic electrolytes are not suitable for extremely high-temperature operation. In this regard, solvent-free ILs are ideal candidates due to their high thermal and electrochemical stability. EC containing EMIm OAc electrolyte can function up to a high temperature of 150 °C but is suggested to be used up to 120 °C for long-term use. A maximum operating temperature is gained by lowering the operating voltage. However, the usable voltage range is not compromised due to low IR drop, thanks to the increased ionic conductivity of IL at elevated temperature. Consequently, the energy density and power density also increases at elevated temperature compared to RT. The mutually beneficial compensation between the operating voltage and high-temperature operation can be implemented in other neat IL-based electrolytes. At extremely high temperatures, special attention has to be given to address the mismatch in the thermal expansion coefficient among the different components.

Even though ILs are suitable at high temperature they show accelerated self-discharge and leakage rates compromising a reliable operation of EC. A systematic investigation on EMIm OAc containing ECs from RT to 60 °C reveals that instantaneous temperature exposure is mostly responsible for accelerated self-discharge rather than operating history considering operation is carried out within the electrochemical potential window and with an appropriate charging current. With experimental results and mathematical treatment, it is found out that at high-temperature diffusion-controlled mechanisms strongly dominate over CR-mechanisms in the observed self-discharge behavior at lower initial voltages, whereas, the contributions from both these mechanisms are comparable at RT. A very small contribution to the CR-mechanism is related to the decreased time constant as a consequence of improved ion dynamics at elevated temperatures.

The driving force of self-discharge is thermodynamic by nature; therefore, it can not be completely stopped. The kinetics can be slowed down with component modifications. In this regard, a small amount of the nematic LC 5CB shows great potential when added to an aqueous Li_2SO_4 electrolyte. The observed reduction of self-discharge behavior originates from the dielectric anisotropy of the LC. We speculate that at a charged state, LC molecules align together close to the interfaces and create a pseudo-blocking layer which slows down the diffusion of ions and results in a lower self-discharge. Voltage-dependent ion dynamics with 5CB containing EC is revealed by the EIS measurements, which show an increased interfacial resistance of the 5CB/electrolyte composite at different charged states, whereas no change is observed for the device without 5CB. Self-discharge reduction with liquid crystal additive does not seem to be restricted to a particular liquid crystal/electrolyte combination, since a previous study showed

similar self-discharge reduction in an organic electrolyte-containing device [109]. However, a further mechanistic study is required to fully understand the microscopic scenario of the role LC is playing.

Improved performance of the IL electrolyte at elevated temperature opens up the possibility to utilize EC as a thermoionic system where a spontaneous voltage output can be achieved by exposing the device to a low-grade waste heat regime (below 100 °C) without any electrical bias. The generated voltage originates from a thermocapacitive effect due to dissimilar interfacial properties in the two EDLs. Furthermore, unused charge in a typical electrical operation, also known as the *"voltage rebound effect"*, can be recovered quickly by utilizing heat. Significantly higher voltage output is observed for the device containing EMIm TFSI compared to EMIm OAc. The observed difference originates from different self-diffusion coefficients of $[EMIM]^+$ cation and $[TFSI]^-$ anion in EMIm TFSI electrolyte whereas, $[EMIM]^+$ cation and $[OAc]^-$ anion has similar sellf-diffusion coefficients in the EMIm OAc electrolyte. Heat exposure (60 °C) to two devices containing EMIm TFSI in series shows a high voltage recovery of over 0.9 V.
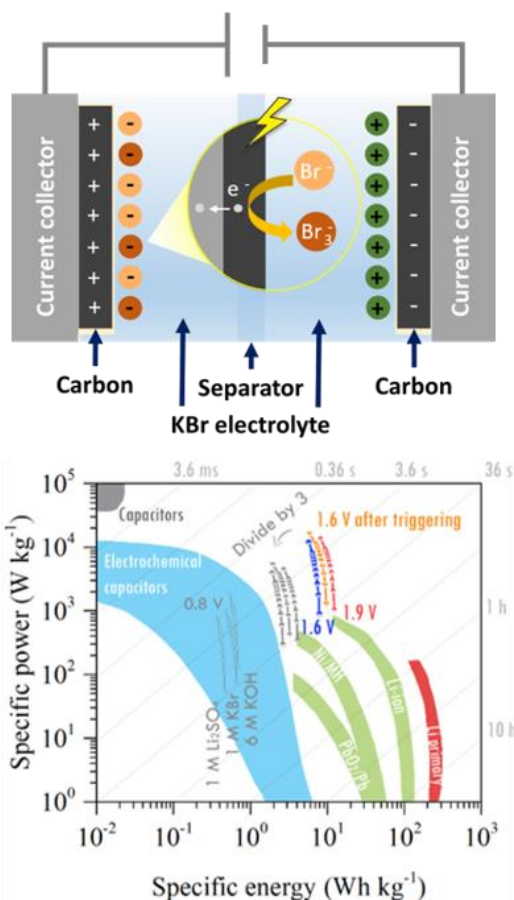
5.2 Future work

Several strategies can be implemented to improve the performance of ECs to a large extent. For instance, the inclusion of multi-redox species in the aqueous system can further increase the energy density, where catholytes and anolytes participate simultaneously in two electrodes and match the redox activity of each other. Moreover, special attention should be given to address the cross-diffusion of redox species that adversely affect the self-discharge behavior. Liquid crystals with different dielectric anisotropies and high phase transition temperature as the electrolyte additives should be further scrutinized to mitigate the self-discharge behavior. *In-situ* measurements such as Small-angle X-ray scattering, Nuclear magnetic resonance spectroscopy can be utilized for detailed study of the orientation and kinetics of the liquid crystals. Incorporation of phase change materials that are able to store and release a large amount of latent heat through a phase transition at constant temperature could be utilized within the device as an efficient *in-situ* thermal management system. Last but not least, combining ionic liquids with varieties of cations and anions or eutectic mixtures is very promising not only regarding extending the temperature range, but also creating a larger asymmetry in the interfaces that could be used to produce electricity from the low-grade waste heat.

Summary of appended papers

Paper-I: Redox enhanced energy storage in an aqueous high-voltage electrochemical capacitor with a potassium bromide electrolyte.

This study reports an effective way to increase the energy density of a symmetric activated carbon-based device containing a redox-active neutral KBr electrolyte with a negligible sacrifice of the power density. Systematic electrochemical investigation reveals that the device behaves as a typical EDLC until 1.6 V. At higher voltages, redox reactions from the KBr electrolyte, specifically Br^- / Br_3^- redox species come into play and increases not only the energy density but also demonstrates excellent stability, a high coulombic and energy efficiency even at 1.9 V. Subsequently, at this high voltage, the device demonstrates a hybrid behavior. Most importantly, the redox contribution can be triggered by pre-cycling the device at 1.9 V and can be retained at a lower voltage. As a consequence, the energy density of the device at 1.6 V after "triggering" is significantly higher, 9.0 Wh Kg^{-1}, a 22% increase compared to the device with no pre-cycling. The increase of the energy density without significant sacrifice of power density has been achieved with a controlled manipulation of the redox activity of the KBr electrolyte.

Redox activity of Br^- / Br_3^- at the positive electrode and comparison of energy density and power density with other systems

The intriguing behavior of the "triggering effect" is accompanied by a series of complex variations including, a positive shift of the electrode potential limits of the positive electrode, negative electrode, and potential of zero voltage. The observed phenomenon is qualitatively explained by the electro-oxidation of the positive electrode and the slow kinetics of the Br^- / Br_3^- reaction. These findings are not restricted to only bromine but also other redox species with a high electrode potential and provide valuable insights for designing high voltage redox-active EDLC.

Paper-II: Thermal Influence on the Electrochemical Behavior of a Supercapacitor Containing an Ionic Liquid Electrolyte.

The interaction between all the different components of the EC, such as electrodes, electrolytes, separators, and current collectors at elevated temperatures, becomes a critical issue for EC operation in harsh environments. This work presents a comprehensive electrochemical study of the thermal influence on an EC containing 1-ethyl-3-methylimidazolium acetate (EMIM Ac) electrolyte and activated carbon (AC) electrodes in a wide temperature range from room temperature (25 °C) to 150 °C. The results show a low ESR value of 2.5 Ω cm^2 at room temperature, revealing excellent compatibility of the EMIM Ac electrolyte and the AC electrode. Several sets of CV and GCD measurements show that the device could operate in a voltage range of 0-1.5 V up to 80 °C. Even though a high operating voltage is necessary to achieve a high energy density, a reduction of the operating voltage is quite essential to avoid accelerated aging that originates from elevated temperatures. Consequently, the operating voltage was lowered to 1.4 V up to 120 °C and further lowered to 1.3 V at 150 °C. Interestingly, both the specific energy density and power density were not reduced because of lowering the operating voltage range; instead, it increased quite significantly compared to room temperature performance. Due to the high viscosity and low ionic conductivity of EMIM Ac at room temperature, the device suffers from a high IR drop resulting in a lower usable voltage of 1.31 V. The ionic conductivity of the neat ionic liquid increases with increasing temperature, which facilitates an increased capacitance and a significant decrease of IR drop. Therefore, even though the operating potential is lowered, the usable voltage is enlarged, and the device could maintain a high energy density and power density at elevated temperatures. Cyclic stability tests show that the device could be well functional up to 150 °C within 0-1.3 V, but 120 °C and 1.4 V are suggested to be the upper temperature and voltage limits for long-term use.

Performance metrics of the supercapacitor from GCD measurements

Temperature (°C)	Max. voltage (V)	IR drop [a] (mV)	Useable voltage (V)	Energy density (Wh kg^{-1})	Max. Power density (kW kg^{-1})	Rate capability (%)	Capacitance [b] (F g^{-1})
RT	1.5	186	1.31	4.3	4.6	62	84
40	1.5	79	1.42	6.1	12.8	78	98
80	1.5	35	1.46	8.3	30.5	82	122
100	1.4	29	1.37	7.3	32.5	85	121
120	1.4	26	1.37	7.4	36.0	85	121
RT/120	1.5	134	1.36	4.9	6.9	66	88
150	1.3	23	1.28	7.7	35.6	87	142

[a] IR drop at 3 A g^{-1}, [b] Maximum capacitance is achieved at 1 A g^{-1} while 2 A g^{-1} for 150 °C

Paper-III: Identification of self-discharge mechanism of ionic liquid electrolyte-based supercapacitor under high-temperature operation.

Ionic liquids (ILs) are suitable electrolytes for high-temperature operations due to their good thermal stability. Especially due to their high viscosity at RT, the optimum electrochemical performance is expected to be around 60 °C. However, a high-temperature operation also accelerates the self-discharge rate, in fact, the self-discharge current doubles in every 10 K increase in temperature. Therefore, this study focuses on identifying the underlying self-discharge mechanisms of SCs containing an IL, 1-ethyl-3-methylimidazolium acetate (EMIM Ac) electrolyte at different temperatures, ranging from RT-60 °C. A systematic temperature exposure of multiple devices indicated that the increased self-discharge rate is strictly influenced by the instantaneous temperature exposure rather than the operating history of the devices. The voltage loss due to ohmic leakage and activation-controlled Faradaic processes were ruled out based on the correlations with models based on the governing equations of different self-discharge mechanisms, as well as activation energy calculations. A mixed mechanism of charge redistribution and diffusion is identified to be responsible for the observed voltage decay. At an elevated temperature of 60 °C, the diffusion-controlled mechanism dominates at lower initial voltages over the charge redistribution (CR) effect, while at RT both mechanisms contribute comparably. The reduced contribution from CR at 60 °C in the lower initial voltage is due to a decreased RC time constant (τ_{RC}), which is confirmed by the impedance measurements.
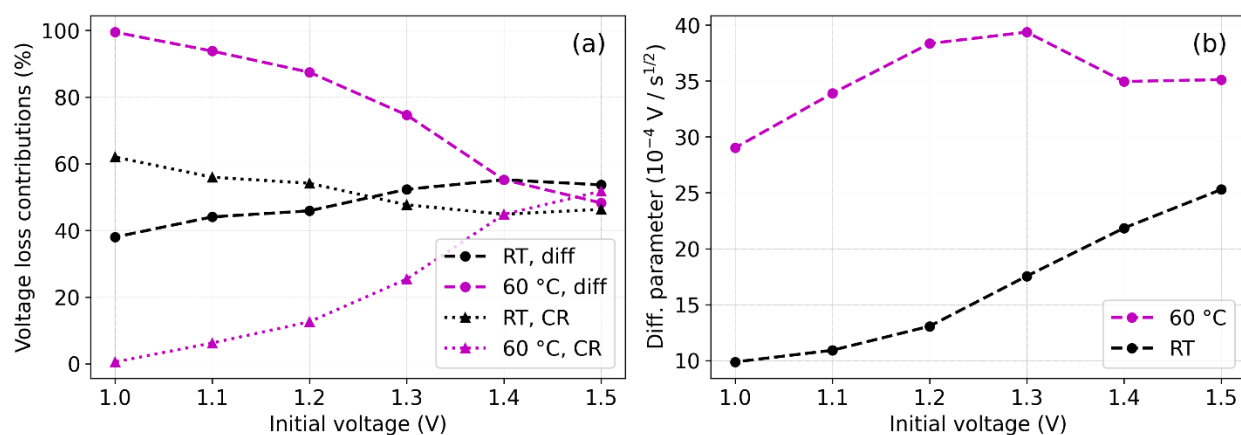
(a) Voltage loss contribution from charge redistribution (CR) and diffusion mechanisms and (b) diffusion parameter at different initial voltages at RT and 60 °C

Paper-IV: Self-discharge and leakage current mitigation of neutral aqueous-based supercapacitor by means of liquid crystal additive.
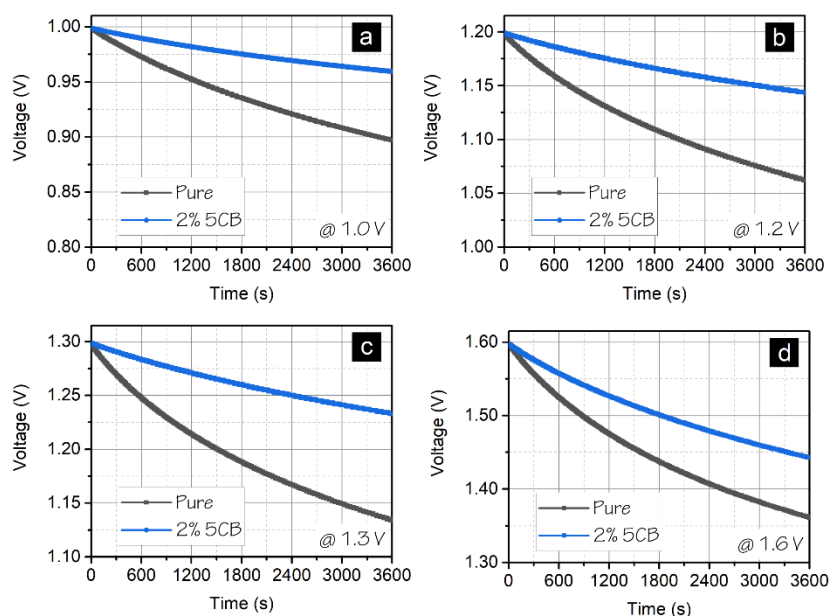

Open circuit voltage decay from different initial voltages (a) 1 V (b) 1.2 V (C) 1.3 V and (d) 1.6 V

Relatively high self-discharge and leakage currents are among the main obstacles to implementing ECs in self-powered systems. In this work, a thorough electrochemical investigation is carried out to address the self-discharge and leakage current reduction of a neutral aqueous electrolyte-based ECs containing Li_2SO_4 and activated carbon cloth electrodes. A liquid crystal 2% 4-n-pentyl-4'-cyanobiphenyl (5CB, is used as an additive to the 1 M Li_2SO_4 to suppress the self-discharge and leakage current without compromising other critical capacitive performance such as capacitance, energy density, power density, and cyclic stability. Open circuit voltage decay at different nominal voltages reveals that the EC device with 5CB additive shows a reduced self-discharge and leakage current compared to the device without 5CB additive. The observed reduction of self-discharge and leakage current is believed to be originating from the slower diffusion of electrolyte ions from the surface to the bulk of the electrolyte as a result of the intrinsic positive dielectric anisotropic properties of the 5CB. At a charged state, due to a high electric field inside the EC, the phase-separated liquid crystal molecules align themselves in the diffuse layer, where they form a continuous thin film along the electrodes and slow down the diffusion of electrolyte ions. At a discharged state, there is no electric field keeping the thin film alignment, and the liquid crystal molecules are randomly distributed in the bulk electrolyte facilitating similar charging behavior as the device without 5CB. The beneficial effect can be maintained up to 1.6 V and is not only restricted to this particular electrolyte-liquid crystal mixture but could be extended to other electrolytes and liquid crystal combinations with different dielectric anisotropy.

Paper-V: Exploiting low-grade waste heat to produce electricity through supercapacitor containing carbon electrodes and ionic liquid electrolytes.
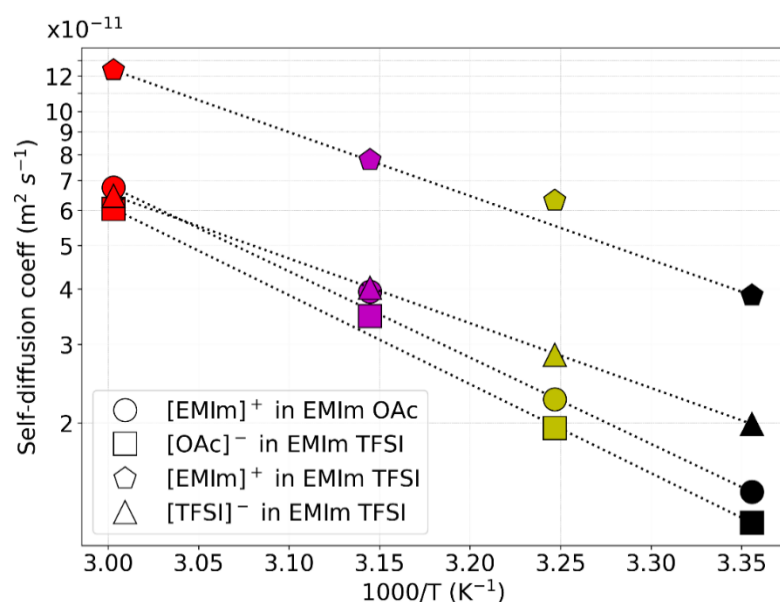
Arrhenius plot of self-diffusion coefficients of individual ions in a temperature range from 25 to 60 °C

Thermal energy is an attractive energy resource, originating as a by-product of different industrial and non-industrial processes. The majority of this energy is unused and stays in the surroundings as waste heat. Low-grade waste heat, readily available below 100 °C, constitutes as much as 63 % of this potential resources. Recovering or utilizing this waste heat holds enormous prospects not just limited to improving energy efficiency but also opening the possibility to capture energy from abundant resources like solar thermal energy, geothermal energy, and ocean thermal energy. In this study, we focus on exploring the feasibility of utilizing low-grade waste heat to store or recover charge in a supercapacitor containing two different ionic liquids (ILs), 1-Ethyl-3-methylimidazolium bis (trifluoromethylsulfonyl) imide, EMIm TFSI, and 1-Ethyl-3-methylimidazolium acetate, EMIm OAc, and activated carbon electrodes. When supercapacitors are exposed to heat (60 °C), a spontaneous voltage develops due to thermally induced changes in the ionic charge density at the electrode/electrolyte interface known as the "thermocapacitive effect". Moreover, due to the difference in kinetics between the fast movement of free electrons and the slower movement of counterions at the interface, a significant portion of the charge stays unused in a typical electrical charge/discharge cycle, which emerges slowly with a voltage rise in open circuit conditions. When the devices are subjected to heat after an electrical charge/discharge cycle, the unused charge is recovered faster and to a larger extent. The observed difference in voltage output between two ILs containing devices is confirmed by a Pulsed-field gradient NMR spectroscopy, which shows that due to a large difference in the self-diffusion coefficients of [EMIm]+ in EMIm TFSI electrolyte compared [EMIm]+ in EMIm OAc, the voltage output is significantly higher for EMIm TFSI containing devices in different conditioning.

References

[1] X. Lin, M. Salari, L.M. Arava, P.M. Ajayan, M.W. Grinstaff, Chem. Soc. Rev., 45 (2016) 5848-5887.

[2] A. Noori, M.F. El-Kady, M.S. Rahmanifar, R.B. Kaner, M.F. Mousavi, Chem. Soc. Rev., 48 (2019) 1272-1341.

[3] J.R. Miller, P. Simon, Science, 321 (2008) 651-652.

[4] J.R. Miller, A.F. Burke, Electrochem Soc Interface, 17 (2008) 53.

[5] M.R. Lukatskaya, B. Dunn, Y. Gogotsi, Nat. Commun., 7 (2016).

[6] J. Lee, P. Srimuk, S. Fleischmann, X. Su, T.A. Hatton, V. Presser, Prog Mater Sci, 101 (2019) 46-89.

[7] L. Xia, L. Yu, D. Hu, G.Z. Chen, Mater. Chem. Front, 1 (2017) 584-618.

[8] J.M. Miller, Ultracapacitor applications, Stevenage: The Institution of Engineering and Technology, 2011.

[9] P. Simon, Y. Gogotsi, Nat. Mater., 7 (2008) 845-854.

[10] C. Zhong, Y. Deng, W. Hu, J. Qiao, L. Zhang, J. Zhang, Chem. Soc. Rev., 44 (2015) 7484-7539.

[11] H.A. Andreas, J. Electrochem. Soc., 162 (2015) A5047-A5053.

[12] B.E. Conway, W. Pell, T. Liu, J. Power Sources, 65 (1997) 53-59.

[13] S. Fletcher, V.J. Black, I. Kirkpatrick, J. Solid State Electrochem., 18 (2014) 1377-1387.

[14] C. Hao, X. Wang, Y. Yin, Z. You, J. Electron. Mater., 45 (2016) 2160-2171.

[15] B.E. Conway, Electrochemical supercapacitors: scientific fundamentals and technological applications, Springer Science & Business Media, 2013.

[16] M.R. Palacín, A. de Guibert, Science, 351 (2016).

[17] G.Z. Chen, Int. Mater. Rev., 62 (2017) 173-202.

[18] A. Yu, V. Chabot, J. Zhang, Electrochemical supercapacitors for energy storage and delivery: fundamentals and applications, CRC press, 2013.

[19] M. Jayalakshmi, K. Balasubramanian, Int. J. Electrochem. Sci, 3 (2008) 1196-1217.

[20] https://www.nmr.mgh.harvard.edu/~reese/electrolytics/tec1.pdf

[21] J.R. Miller, Electrical Insulation Magazine, IEEE, 26 (2010) 40-47.

[22] L.L. Zhang, X. Zhao, Chem. Soc. Rev., 38 (2009) 2520-2531.

[23] H.v. Helmholtz, Annalen der Physik, 165 (1853) 353-377.

[24] F. Béguin, V. Presser, A. Balducci, E. Frackowiak, Adv. Mater. (Weinheim, Ger.), 26 (2014) 2219-2251.

[25] M. Gouy, J. Phys. Theor. Appl (1910).

[26] D.L. Chapman, The London, Edinburgh, and Dublin philosophical magazine and journal of science, 25 (1913) 475-481.

[27] O. Stern, Zeitschrift für Elektrochemie und angewandte physikalische Chemie, 30 (1924) 508-516.

[28] D.C. Grahame, Chem. Rev. (Washington, DC, U. S.), 41 (1947) 441-501.

[29] L. Pilon, H. Wang, A. d'Entremont, J. Electrochem. Soc., 162 (2015) A5158-A5178.

[30] K.S. Sing, Pure Appl. Chem., 57 (1985) 603-619.

[31] M. Thommes, K. Kaneko, A.V. Neimark, J.P. Olivier, F. Rodriguez-Reinoso, J. Rouquerol, K.S. Sing, Pure Appl. Chem., 87 (2015) 1051-1069.

[32] E. Raymundo-Piñero, K. Kierzek, J. Machnikowski, F. Béguin, Carbon, 44 (2006) 2498-2507.

[33] J. Chmiola, G. Yushin, Y. Gogotsi, C. Portet, P. Simon, P.-L. Taberna, Science, 313 (2006) 1760-1763.

[34] J. Huang, B.G. Sumpter, V. Meunier, Chem. Eur. J., 14 (2008) 6614-6626.

[35] J. Huang, B.G. Sumpter, V. Meunier, Angew. Chem. Int. Ed., 47 (2008) 520-524.

[36] J.P. Zheng, J. Huang, T. Jow, J. Electrochem. Soc., 144 (1997) 2026.

References

[37] B. Conway, V. Birss, J. Wojtowicz, J. Power Sources, 66 (1997) 1-14.

[38] J.H. Chae, X. Zhou, G.Z. Chen, Green, 2 (2012) 41-54.

[39] T. Brousse, D. Bélanger, J.W. Long, J. Electrochem. Soc., 162 (2015) A5185-A5189.

[40] V. Augustyn, P. Simon, B. Dunn, Energy Environ. Sci, 7 (2014) 1597-1614.

[41] G.Z. Chen, Prog. Nat. Sci., 23 (2013) 245-255.

[42] A. Jagadale, X. Zhou, R. Xiong, D.P. Dubal, J. Xu, S. Yang, Energy Storage Mater., 19 (2019) 314-329.

[43] S. Senthilkumar, R.K. Selvan, J. Melo, J. Mater. Chem. A, 1 (2013) 12386-12394.

[44] S.-E. Chun, B. Evanko, X. Wang, D. Vonlanthen, X. Ji, G.D. Stucky, S.W. Boettcher, Nat. Commun., 6 (2015).

[45] J. Lee, P. Srimuk, S. Fleischmann, A. Ridder, M. Zeiger, V. Presser, J. Mater. Chem. A, 5 (2017) 12520-12527.

[46] J. Lee, B. Krüner, A. Tolosa, S. Sathyamoorthi, D. Kim, S. Choudhury, K.-H. Seo, V. Presser, Energy Environ. Sci., 9 (2016) 3392-3398.

[47] E. Frackowiak, K. Fic, M. Meller, G. Lota, ChemSusChem, 5 (2012) 1181-1185.

[48] J. Lee, A. Tolosa, B. Krüner, N. Jäckel, S. Fleischmann, M. Zeiger, D. Kim, V. Presser, Sustain. Energ. Fuels, 1 (2017) 299-307.

[49] B. Krüner, J. Lee, N. Jäckel, A. Tolosa, V. Presser, ACS Appl. Mater. Interfaces, 8 (2016) 9104-9115.

[50] B. Akinwolemiwa, C. Peng, G.Z. Chen, J. Electrochem. Soc., 162 (2015) A5054-A5059.

[51] R. Signorelli, D.C. Ku, J.G. Kassakian, J.E. Schindall, Proceedings of the IEEE, 97 (2009) 1837-1847.

[52] H. Lindström, S. Södergren, A. Solbrand, H. Rensmo, J. Hjelm, A. Hagfeldt, S.-E. Lindquist, J. Phys. Chem. B, 101 (1997) 7717-7722.

[53] T. Liu, W. Pell, B. Conway, S. Roberson, J. Electrochem. Soc., 145 (1998).

[54] T. Brezesinski, J. Wang, J. Polleux, B. Dunn, S.H. Tolbert, J. Am. Chem. Soc., 131 (2009) 1802-1809.

[55] J. Wang, J. Polleux, J. Lim, B. Dunn, J. Phys. Chem. C, 111 (2007) 14925-14931.

[56] H.D. Yoo, J.H. Jang, J.H. Ryu, Y. Park, S.M. Oh, J. Power Sources, 267 (2014) 411-420.

[57] A.J. Bard, L.R. Faulkner, J. Leddy, C.G. Zoski, Electrochemical methods: fundamentals and applications, wiley New York, 1980.

[58] S. Zhang, N. Pan, Adv. Energy Mater., 5 (2015).

[59] J.R. Miller, R. Outlaw, B. Holloway, Science, 329 (2010) 1637-1639.

[60] P.L. Taberna, P. Simon, J.F. Fauvarque, J. Electrochem. Soc., 150 (2003) A292-A300.

[61] J. Yew, T. Saha, A. Thomas, in: Power Engineering Society General Meeting, 2006. IEEE, IEEE, 2006, pp. 7 pp.

[62] A. Lewandowski, A. Olejniczak, M. Galinski, I. Stepniak, J. Power Sources, 195 (2010) 5814-5819.

[63] P. Ratajczak, K. Jurewicz, P. Skowron, Q. Abbas, F. Béguin, Electrochim. Acta, 130 (2014) 344-350.

[64] M. Zhu, C.J. Weber, Y. Yang, M. Konuma, U. Starke, K. Kern, A.M. Bittner, Carbon, 46 (2008) 1829-1840.

[65] P. Azaïs, L. Duclaux, P. Florian, D. Massiot, M.-A. Lillo-Rodenas, A. Linares-Solano, J.-P. Peres, C. Jehoulet, F. Béguin, J. Power Sources, 171 (2007) 1046-1053.

[66] R. Kötz, P.W. Ruch, D. Cericola, J. Power Sources, 195 (2010) 923-928.

[67] D. Weingarth, A. Foelske-Schmitz, R. Kötz, J. Power Sources, 225 (2013) 84-88.

[68] R. Kotz, M. Carlen, Electrochim. Acta, 45 (2000) 2483-2498.

[69] E. Talaie, P. Bonnick, X. Sun, Q. Pang, X. Liang, L.F. Nazar, Chem. Mater., 29 (2017) 90-105.

[70] G.Y. Gor, M. Thommes, K.A. Cychosz, A.V. Neimark, Carbon, 50 (2012) 1583-1590.

[71] P. Ruch, D. Cericola, A. Foelske-Schmitz, R. Kötz, A. Wokaun, Electrochim. Acta, 55 (2010) 4412-4420.

[72] D. Cericola, P.W. Ruch, A. Foelske-Schmitz, D. Weingarth, R. Kötz, Int. J. Electrochem. Sci, 6 (2011) 988-996.

[73] V.C. Gungor, G.P. Hancke, IEEE Transactions on industrial electronics, 56 (2009) 4258-4265.

[74] J. Niu, B.E. Conway, W.G. Pell, J. Power Sources, 135 (2004) 332-343.

[75] S. Ban, J. Zhang, L. Zhang, K. Tsay, D. Song, X. Zou, Electrochim. Acta, 90 (2013) 542-549.

[76] M. Yu, Y. Lu, H. Zheng, X. Lu, Chem. Eur. J., 24 (2018) 3639-3649.

[77] P. Kurzweil, M. Chwistek, J. Power Sources, 176 (2008) 555-567.

[78] P. Kurzweil, M. Chwistek, R. Gallay, Proc. 16th Int. Semin. Double Layer Capacitors, (2006) 1-15.

[79] M. Zhang, Y. Li, Z. Shen, J. Power Sources, 414 (2019) 479-485.

[80] V. Khomenko, E. Raymundo-Piñero, F. Béguin, J. Power Sources, 195 (2010) 4234-4241.

[81] Q. Gao, L. Demarconnay, E. Raymundo-Piñero, F. Béguin, Energy Environ. Sci., 5 (2012) 9611-9617.

[82] X. Zang, C. Shen, M. Sanghadasa, L. Lin, ChemElectroChem, 6 (2019) 976-988.

[83] K. Fic, G. Lota, M. Meller, E. Frackowiak, Energy Environ. Sci., 5 (2012) 5842-5850.

[84] K. Jurewicz, E. Frackowiak, F. Béguin, Appl. Phys. A, 78 (2004) 981-987.

[85] K. Fic, M. Meller, E. Frackowiak, J. Electrochem. Soc., 162 (2015) A5140-A5147.

[86] L. Demarconnay, E. Raymundo-Pinero, F. Béguin, Electrochem. Commun., 12 (2010) 1275-1278.

[87] B. Evanko, S.W. Boettcher, S.J. Yoo, G.D. Stucky, ACS Energy Lett., 2 (2017) 2581-2590.

[88] M. De Castro, B. Wilde, Corros. Sci., 19 (1979) 923-936.

[89] A. Shukla, S. Sampath, K. Vijayamohanan, Curr. Sci., 79 (2000) 1656-1661.

[90] G. Xiong, A. Kundu, T.S. Fisher, in: Springer Briefs in Applied Sciences and Technology 2015.

[91] H. Gualous, H. Louahlia, R. Gallay, IEEE Transactions on power electronics, 26 (2011) 3402-3409.

[92] N. Sato, J. Power Sources, 99 (2001) 70-77.

[93] R. Kötz, M. Hahn, R. Gallay, J. Power Sources, 154 (2006) 550-555.

[94] E. Perricone, M. Chamas, J.-C. Leprêtre, P. Judeinstein, P. Azais, E. Raymundo-Pinero, F. Béguin, F. Alloin, J. Power Sources, 239 (2013) 217-224.

[95] M. Armand, F. Endres, D.R. MacFarlane, H. Ohno, B. Scrosati, Nat. Mater., 8 (2009) 621-629.

[96] A. Brandt, S. Pohlmann, A. Varzi, A. Balducci, S. Passerini, MRS bulletin, 38 (2013) 554-559.

[97] S. Fendt, S. Padmanabhan, H.W. Blanch, J.M. Prausnitz, J. Chem. Eng. Data, 56 (2010) 31-34.

[98] T. Liebert, T. Heinze, BioResources, 3 (2008) 576-601.

[99] M. Zavrel, D. Bross, M. Funke, J. Büchs, A.C. Spiess, Bioresour. Technol., 100 (2009) 2580-2587.

[100] K. Kierzek, E. Frackowiak, G. Lota, G. Gryglewicz, J. Machnikowski, Electrochim Acta, 49 (2004) 515-523.

[101] B. Pillay, J. Newman, J. Electrochem. Soc., 143 (1996) 1806-1814.

[102] B.W. Ricketts, C. Ton-That, J. Power Sources, 89 (2000) 64-69.

[103] H. Yang, Y. Zhang, J. Power Sources, 273 (2015) 223-236.

[104] J. Black, H.A. Andreas, Electrochim. Acta, 54 (2009) 3568-3574.

[105] T. Tevi, H. Yaghoubi, J. Wang, A. Takshi, J. Power Sources, 241 (2013) 589-596.

[106] H. Wang, Q. Zhou, B. Yao, H. Ma, M. Zhang, C. Li, G. Shi, Adv. Mater. Interfaces, (2018) 1701547.

[107] Y. Wang, X. Qiao, C. Zhang, X. Zhou, Energy, 159 (2018) 1035-1045.

[108] K. Fic, G. Lota, E. Frackowiak, Electrochim. Acta, 55 (2010) 7484-7488.

[109] M. Xia, J. Nie, Z. Zhang, X. Lu, Z.L. Wang, Nano Energy, 47 (2018) 43-50.

[110] S.-S. Sun, L.R. Dalton, Introduction to organic electronic and optoelectronic materials and devices, CRC Press, 2016.

[111] J. Ananthaiah, R. Sahoo, M. Rasna, S. Dhara, Phys. Rev. E, 89 (2014) 022510.

[112] K. Negita, J. Chem. Phys., 105 (1996) 7837-7841.

[113] J.-Y. Song, L. Zhang, J.-Y. Zou, in: 2008 14th Symposium on Electromagnetic Launch Technology, IEEE, 2008, pp. 1-5.

[114] K. Negita, Chem. Phys. Lett., 246 (1995) 353-357.

[115] C. Forman, I.K. Muritala, R. Pardemann, B. Meyer, Renew. Sust. Energ Rev., 57 (2016) 1568-1579.

[116] X. Zhang, M. He, Y. Zhang, Renew. Sust. Energ Rev., 16 (2012) 5309-5318.

[117] G.J. Snyder, E.S. Toberer, Materials for sustainable energy: a collection of peer-reviewed research and review articles from Nature Publishing Group, (2011) 101-110.

[118] A. Laiho, L. Herlogsson, R. Forchheimer, X. Crispin, M. Berggren, Proc. Natl. Acad. Sci., 108 (2011) 15069-15073.

[119] B. Poudel, Q. Hao, Y. Ma, Y. Lan, A. Minnich, B. Yu, X. Yan, D. Wang, A. Muto, D. Vashaee, Science, 320 (2008) 634-638.

[120] Y. Sun, P. Sheng, C. Di, F. Jiao, W. Xu, D. Qiu, D. Zhu, Adv. Mater., 24 (2012) 932-937.

[121] B. Xu, L. Liu, H. Lim, Y. Qiao, X. Chen, Nano Energy, 1 (2012) 805-811.

[122] W. Liu, X. Yan, G. Chen, Z. Ren, Nano Energy, 1 (2012) 42-56.

[123] H. Wang, D. Zhao, Z.U. Khan, S. Puzinas, M.P. Jonsson, M. Berggren, X. Crispin, Adv. Electron. Mater, 3 (2017) 1700013.

[124] W. Liu, X. Qian, C.-G. Han, Q. Li, G. Chen, Appl. Phy. Lett, 118 (2021) 020501.

[125] D. Zhao, A. Würger, X. Crispin, J. Energy Chem. 61 (2021) 88-103.

[126] A. Al-zubaidi, X. Ji, J. Yu, Sustain. Energ. Fuels, 1 (2017) 1457-1474.

[127] X. Shi, J. He, Science, 371 (2021) 343-344.

[128] A. Härtel, M. Janssen, D. Weingarth, V. Presser, R. van Roij, Energy Environ. Sci., 8 (2015) 2396-2401.

[129] H. Lim, Y. Shi, Y. Qiao, App. Phys. A, 122 (2016) 443.

[130] J.J. Wang, S.P. Feng, Y. Yang, N.Y. Hau, M. Munro, E. Ferreira-Yang, G. Chen, Nano Lett., 15 (2015) 5784-5790.

[131] D. Zhao, H. Wang, Z.U. Khan, J. Chen, R. Gabrielsson, M.P. Jonsson, M. Berggren, X. Crispin, Energy Environ. Sci., 9 (2016) 1450-1457.

[132] E. Frackowiak, Q. Abbas, F. Béguin, J. Energy Chem., 22 (2013) 226-240.

[133] Q. Li, V. Kuzmenko, M. Haque, M. Di, A.D. Smith, P. Lundgren, P. Enoksson, Electrochim. Acta, (2020) 135921.

[134] C. Subramaniam, T. Pradeep, J. Chakrabarti, J. Phys. Chem. C, 111 (2007) 19103-19110.

[135] B. Xu, Y. Qiao, T. Park, M. Tak, Q. Zhou, X. Chen, Energy Environ. Sci., 4 (2011) 3632-3639.

[136] B. Xu, B. Wang, T. Park, Y. Qiao, Q. Zhou, X. Chen, J. Chem. Phys., 136 (2012) 184701.

[137] D. Lee, Langmuir, 23 (2007) 6011-6018.

[138] J.W. Graydon, M. Panjehshahi, D.W. Kirk, J. of Power Sources, 245 (2014) 822-829.

[139] E. Laux, S. Uhl, T. Journot, J. Brossard, L. Jeandupeux, H. Keppner, J. Electron. Mater., 45 (2016) 3383-3389.

[140] A.W. King, A. Parviainen, P. Karhunen, J. Matikainen, L.K. Hauru, H. Sixta, I. Kilpeläinen, RSC adv., 2 (2012) 8020-8026.

[141] K. Hayamizu, Y. Aihara, H. Nakagawa, T. Nukuda, W.S. Price, J. Phys. Chem. B, 108 (2004) 19527-19532.

[142] R.C. Remsing, G. Hernandez, R.P. Swatloski, W.W. Massefski, R.D. Rogers, G. Moyna, J. Phys. Chem. B, 112 (2008) 11071-11078.